



1-1-2014

Intervertebral Disc Structure and Mechanical Function Under Physiological Loading Quantified Non-invasively Utilizing MRI and Image Registration

Jonathon H. Yoder

University of Pennsylvania, jonathon.yoder@gmail.com

Follow this and additional works at: <http://repository.upenn.edu/edissertations>

 Part of the [Biomechanics Commons](#), [Biomedical Commons](#), and the [Radiology Commons](#)

Recommended Citation

Yoder, Jonathon H., "Intervertebral Disc Structure and Mechanical Function Under Physiological Loading Quantified Non-invasively Utilizing MRI and Image Registration" (2014). *Publicly Accessible Penn Dissertations*. 1511.
<http://repository.upenn.edu/edissertations/1511>

This paper is posted at ScholarlyCommons. <http://repository.upenn.edu/edissertations/1511>
For more information, please contact libraryrepository@pobox.upenn.edu.

Intervertebral Disc Structure and Mechanical Function Under Physiological Loading Quantified Non-invasively Utilizing MRI and Image Registration

Abstract

The intervertebral discs (IVD) functions to permit motion, distribute load, and dissipate energy in the spine. It performs these functions through its heterogeneous structural organization and biochemical composition consisting of several tissue substructures: the central gelatinous nucleus pulposus (NP), the surrounding fiber reinforced layered annulus fibrosus (AF), and the cartilaginous endplates (CEP) that are positioned between the NP and vertebral endplates. Each tissue contributes individually to overall disc mechanics and by interacting with adjacent tissues. Disruption of the disc's tissues through aging, degeneration, or tear will not only alter the affected tissue mechanical properties, but also the mechanical behavior of adjacent tissues and, ultimately, overall disc segment function. Thus, there is a need to measure disc tissue and segment mechanics in the intact disc so that interactions between substructures are not disrupted. Such measurements would be valuable to study mechanisms of disc function and degeneration, and develop and evaluate surgical procedures and therapeutic implants. The objectives of this study were to develop, validate, and apply methods to visualize and quantify IVD substructure geometry and track internal deformations for intact human discs under axial compression. The CEP and AF were visualized through MRI parameter mapping and image sequence optimization for ideal contrast. High-resolution images enabled geometric measurements. Axial compression was performed using a custom-built loading device that permitted long relaxation times outside of the MRI, 300 μ m isotropic resolution images were acquired, and image registration methods applied to measure 3D internal strain. In conclusion, new methods to visualize and quantify CEP thickness, annular tear detection and geometric quantification, and non-invasively measure 3D internal disc strains were established. No correlation was found between CEP thickness and disc level; however the periphery was significantly thicker compared to central locations. Clear distinction of adjacent AF lamellae enabled annular tear detection and detailed geometric quantification. Annular tears demonstrated "non-classic" geometry through interconnecting radial, circumferential, and perinuclear formations. Regional strain inhomogeneity was observed qualitatively and quantitatively. Variation in strain magnitudes might be explained by geometry in axial and circumferential strain while peak radial strain in the posterior AF may have important implications for disc herniation.

Degree Type

Dissertation

Degree Name

Doctor of Philosophy (PhD)

Graduate Group

Mechanical Engineering & Applied Mechanics

First Advisor

Dawn M. Elliott

Keywords

annulus fibrosus, axial compression, image registration, internal strain, intervertebral disc, magnetic resonance imaging

Subject Categories

Biomechanics | Biomedical | Radiology

**INTERVERTEBRAL DISC STRUCTURE AND MECHANICAL
FUNCTION UNDER PHYSIOLOGICAL LOADING QUANTIFIED
NON-INVASIVELY UTILIZING MRI AND IMAGE
REGISTRATION**

Jonathon Henry Yoder

A DISSERTATION

in

Mechanical Engineering and Applied Mechanics

Presented to the Faculties of the University of Pennsylvania

in

Partial Fulfillment of the Requirements for the

Degree of Doctor of Philosophy

2014

Supervisor of Dissertation

Dawn M. Elliott, Professor – Director of Biomedical Engineering University of Delaware

Graduate Group Chairperson

Prashant Purohit, Chair and Associate Professor MEAM

Dissertation Committee:

Louis J Soslowsky, Fairhill Professor Orthopaedic Surgery and Professor Bioengineering

James C Gee, Associate Professor Radiologic Science in Radiology

Prashant Purohit, Chair and Associate Professor MEAM

Beth A Winkelstein, Professor Bioengineering

Edward J Vresilovic, Orthopaedic Surgery Penn State University

ABSTRACT

INTERVERTEBRAL DISC STRUCTURE AND MECHANICAL FUNCTION UNDER PHYSIOLOGICAL LOADING QUANTIFIED NON-INVASIVELY UTILIZING MRI AND IMAGE REGISTRATION

Jonathon H Yoder

Dawn M Elliott

The intervertebral discs (IVD) functions to permit motion, distribute load, and dissipate energy in the spine. It performs these functions through its heterogeneous structural organization and biochemical composition consisting of several tissue substructures: the central gelatinous nucleus pulposus (NP), the surrounding fiber reinforced layered annulus fibrosus (AF), and the cartilaginous endplates (CEP) that are positioned between the NP and vertebral endplates. Each tissue contributes individually to overall disc mechanics and by interacting with adjacent tissues. Disruption of the disc's tissues through aging, degeneration, or tear will not only alter the affected tissue mechanical properties, but also the mechanical behavior of adjacent tissues and, ultimately, overall disc segment function. Thus, there is a need to measure disc tissue and segment mechanics in the intact disc so that interactions between substructures are not disrupted. Such measurements would be valuable to study mechanisms of disc function and degeneration, and develop and evaluate surgical procedures and therapeutic implants. The objectives of this study were to develop, validate, and apply methods to visualize and

quantify IVD substructure geometry and track internal deformations for intact human discs under axial compression. The CEP and AF were visualized through MRI parameter mapping and image sequence optimization for ideal contrast. High-resolution images enabled geometric measurements. Axial compression was performed using a custom-built loading device that permitted long relaxation times outside of the MRI, 300 μm isotropic resolution images were acquired, and image registration methods applied to measure 3D internal strain. In conclusion, new methods to visualize and quantify CEP thickness, annular tear detection and geometric quantification, and non-invasively measure 3D internal disc strains were established. No correlation was found between CEP thickness and disc level; however the periphery was significantly thicker compared to central locations. Clear distinction of adjacent AF lamellae enabled annular tear detection and detailed geometric quantification. Annular tears demonstrated “non-classic” geometry through interconnecting radial, circumferential, and perinuclear formations. Regional strain inhomogeneity was observed qualitatively and quantitatively. Variation in strain magnitudes might be explained by geometry in axial and circumferential strain while peak radial strain in the posterior AF may have important implications for disc herniation.

Table of Contents

ABSTRACT	ii
Table of Contents.....	iv
List of Tables	vi
List of Illustrations	viii
CHAPTER 1 Introduction	1
CHAPTER 2 Background	5
2.1. Clinical Significance.....	5
2.2. Intervertebral Disc Structure	6
2.3. Disc Mechanical Function.....	7
2.4. Disc Degeneration	9
2.5. Internal Deformations.....	14
2.6. Medical Image Analysis and Registration Applications	16
2.7. Advanced Normalization Tools Image Registration Parameters	18
CHAPTER 3 Cartilaginous Endplate Geometry	20
3.1. Introduction	20
3.2. Materials and Methods.....	22
3.2.1. Intervertebral disc MRI parameter measurement.....	22
3.2.2. Optimization of CEP image contrast.....	23
3.2.3. Cartilaginous Endplate Imaging.....	24
3.2.4. CEP Histology and endplate thickness quantification	25
3.3. Results.....	27
3.4. Discussion	32
CHAPTER 4 Annulus Fibrosus Lamellar Structure and Defects.....	35
4.1. Introduction	35
4.2. Materials and Methods.....	38
4.2.1. Intervertebral disc MRI parameter measurement.....	38
4.2.2. Optimization of AF image contrast	39
4.2.3. Annulus Fibrosus Imaging.....	40
4.2.4. Annular tear detection	41
4.3. Results.....	43
4.3.1. Annulus Fibrosus Lamellar Visualization	43
4.3.2. Annulus Fibrosus Tear Detection	44
4.4. Discussion	48
CHAPTER 5 Design of a MRI Loading Device	50
5.1. Design Objectives	50
5.2. Design and Fabrication	51
5.2.1. Design Effectiveness	54
5.3. Results and Discussion.....	58
CHAPTER 6 Optimization of ANTs Image Registration Parameters – in 2D images and comparison to Vic2D	59
6.1. Introduction	59

6.2.	Materials and Methods	61
6.2.1.	Mechanical Testing and Image Acquisition.....	61
6.2.2.	Anatomic feature labeling	61
6.2.3.	Optimization of Image Registration Parameters	64
6.2.4.	Nucleotomy Strain Analysis and Validation.....	67
6.3.	Results	68
6.3.1.	Optimization of Image Registration Parameters	68
6.3.2.	Nucleotomy Strain Analysis and Validation.....	69
6.4.	Discussion	71
CHAPTER 7	Verification of Image Registration	73
7.1.	Introduction	73
7.2.	Materials and Methods	76
7.2.1.	Specimen Preparation.....	76
7.2.2.	Mechanical Loading and Image Acquisition.....	76
7.2.3.	Image Processing and Registration	79
7.2.4.	Registration Verification.....	82
7.2.5.	Strain Analysis.....	84
7.3.	Results	87
7.3.1.	Registration Verification.....	87
7.3.2.	Strain Analysis.....	89
7.4.	Discussion	93
CHAPTER 8	Regional Strain of the Annulus Fibrosus under Axial Compression 100	
8.1.	Introduction	100
8.2.	Materials and Methods	104
8.2.1.	Specimen Preparation.....	104
8.2.2.	Mechanical Testing and Image Acquisition.....	104
8.2.3.	Image Registration	105
8.2.4.	Strain Analysis.....	105
8.3.	Results	110
8.3.1.	Axial Disc Height Variance	112
8.3.2.	Circumferential Regional Variance.....	114
8.3.3.	Inner vs. Outer Annulus.....	117
	Discussion	120
CHAPTER 9	Conclusion and Future Directions	129
	Bibliography	137

List of Tables

Table 1: Average (\pm standard deviation) T1 values for a healthy and degenerate disc substructures.	27
Table 2: Average T1 and T2 values for a healthy and degenerate disc substructures.	43
Table 3: Tear severity measurements. Type: R = radial, C = circumferential, PN = perinuclear. Location: L = lateral, TL = trans-lateral, A = anterior, AL = antero-lateral, PL = postero-lateral.....	45
Table 4: Matrix of ANTs registration parameters (transformation models, similarity metrics, regularization techniques). MI = mutual information, MSQ = mean squared difference, CC = fast cross correlation, PR = cross correlation, PSE = point set expectation, DMFFD = directly manipulated free form deformation. Adapted from Avants <i>et al.</i> 2011	64
Table 5: Parametric analysis variable matrix used for registrations	65
Table 1: Mean \pm standard deviation of stress and strain for each applied loading condition. Note that Applied Compression represents grip-to-grip applied strains that are compressive and that these compressive boundary conditions induce negative axial strain. AF = annulus fibrosus, E_{zz} = axial strain, $E_{\theta\theta}$ = circumferential strain, E_{rr} = radial strain. Stress calculated as load divided by area from axial reference MR image. Strains averaged over entire AF volume for each disc. N= 9. 91	
Table 7: Global annulus fibrosus strain values (average \pm standard deviation).	111
Table 8: Results for regional axial (E_{zz}) strain values (mean \pm standard deviation) under 5%, 10%, and 15% axial compression. Region definitions: axial disc height (M = middle region, S/I = attachment region), radial position (O = outer annulus, I = inner annulus), and circumferential position (A = anterior, A-L = anterior-lateral, L = lateral, P-L = posterior-lateral, P = posterior). Three comparisons were made along each axis to assess regional variance: 1. Axial column analyzed superior/posterior vs. middle region disc height within the outer and inner annulus for each circumferential position (A, A-L, L, P-L, P). Circumferential column analyzed the differences between (A, A-L, L, P-L, P) within the outer and inner annulus for each axial disc-height position, and 3. Radial column analyzed inner vs. outer annulus within (A, A-L, L, P-L, P) for each axial disc-height position. Significance ($*$ = $p < 0.05$) and trend (\dagger = $0.05 < p < 0.10$).....	125
Table 9: Results for regional circumferential ($E_{\phi\phi}$) strain values (mean \pm standard deviation) under 5%, 10%, and 15% axial compression. Region definitions: axial disc height (M = middle region, S/I = attachment region), radial position (O = outer annulus, I = inner annulus), and circumferential position (A = anterior, A-L = anterior-lateral, L = lateral, P-L = posterior-lateral, P = posterior). Three comparisons were made along each axis to assess regional variance: 1. Axial column analyzed superior/posterior vs. middle region disc height within the outer and inner annulus for each circumferential position (A, A-L, L, P-L, P). Circumferential column analyzed the differences between (A, A-L, L, P-L, P) within the outer and inner annulus for each axial disc-height position, and 3. Radial column analyzed inner vs. outer annulus within (A, A-L, L, P-L, P) for each axial disc-height position. Significance ($*$ = $p < 0.05$) and trend (\dagger = $0.05 < p < 0.10$).....	126
Table 10: Results for regional radial (E_{rr}) strain values (mean \pm standard deviation) under 5%, 10%, and 15% axial compression. Region definitions: axial disc height (M =	

middle region, S/I = attachment region), radial position (O = outer annulus, I = inner annulus), and circumferential position (A = anterior, A-L = anterior-lateral, L = lateral, P-L = posterior-lateral, P = posterior). Three comparisons were made along each axis to assess regional variance: 1. Axial column analyzed superior/interior vs. middle region disc height within the outer and inner annulus for each circumferential position (A, A-L, L, P-L, P). Circumferential column analyzed the differences between (A, A-L, L, P-L, P) within the outer and inner annulus for each axial disc-height position, and 3. Radial column analyzed inner vs. outer annulus within (A, A-L, L, P-L, P) for each axial disc-height position. Significance (* = $p < 0.05$) and trend ($\dagger = 0.05 < p < 0.10$)..... 127

Table 11: Results for regional radial ($E_{\phi r}$) strain values (mean \pm standard deviation) under 5%, 10%, and 15% axial compression. Region definitions: axial disc height (M = middle region, S/I = attachment region), radial position (O = outer annulus, I = inner annulus), and circumferential position (A = anterior, A-L = anterior-lateral, L = lateral, P-L = posterior-lateral, P = posterior). Three comparisons were made along each axis to assess regional variance: 1. Axial column analyzed superior/interior vs. middle region disc height within the outer and inner annulus for each circumferential position (A, A-L, L, P-L, P). Circumferential column analyzed the differences between (A, A-L, L, P-L, P) within the outer and inner annulus for each axial disc-height position, and 3. Radial column analyzed inner vs. outer annulus within (A, A-L, L, P-L, P) for each axial disc-height position. Significance (* = $p < 0.05$) and trend ($\dagger = 0.05 < p < 0.10$)..... 128

List of Illustrations

Figure 1: Representative lumbar spine image and the intervertebral disc sub-structures...	6
Figure 2: Magnetic resonance images illustrating different stages of human lumbar degeneration. (A) A healthy disc exhibiting distinct AF lamellae and central NP region. (B) A disc exhibiting early stages of degeneration, including moderate height reduction, decreased NP signal intensity and inward bulging of AF lamellae (*). (C) A disc exhibiting advanced stages of degeneration, including severely reduced height, large fissures (*) and generalized structural deterioration.(Smith, Nerurkar et al. 2011)	10
Figure 3: Representative annular and intervertebral disc defects. (Vernon-Roberts, Moore et al. 2007)	11
Figure 4: Pfirrmann grading scale displaying degenerative changes visualized in MR (Pfirrmann, Metzdorf et al. 2001).	13
Figure 5: T2 correlations to T1p and Pfirrmann from Elliot Lab lumbar spine database collected over several years for a multitude of studies	13
Figure 6: Graphical overview of image registration	19
Figure 7: Representative T1 parameter maps at 7T: (A) T1 healthy, (B) T1 degenerate. 23	
Figure 8: Computed MRI signals and image contrast at 7T: (a) NP-CEP image contrast (Δ_{CEP}) according to Equation 3, over the full range of the parameters flip angle and TR. (b) Close-up 3D view within the small dashed box in (a). Asterisk (*) indicates the point chosen as optimal. (c,d) Computed NP (dashed) and CEP (dotted) MRI signals, and image contrast (Δ_{CEP} , solid) versus flip angle at optimal TR (9 ms) (c) and versus TR at optimal flip angle (20°) (d).	28
Figure 9: MRI images of four different specimens with 200 μm isotropic resolution acquired at 7T. Three-plane views reformatted from the same isotropic dataset of each specimen clearly demonstrate the CEP's (arrows) clearly, which are located between the vertebral body and the NP. Axial views show that the shape and size of the CEP can vary considerably for different subjects and levels: (a) 47 years, female, L1L2; (b) 63 years, male, L2L3; (c) 53 years, female, L3L4; (d) 53 years, female, L4L5. Scale bar = 1 cm	29
Figure 10: MRI and histology images of the same specimen (63 years, male, L2L3, Grade 2.6). Axial (a) and coronal (b) FLASH MRI of the whole disc, showing approximate locations of biopsy punches used for histological analysis. (c) Representative histology section of the CEP stained with Alcian blue (glycosaminoglycans) and picrosirius red (collagen) showing adjacent NP and vertebral bone. (d) Von Kossa staining of an undecalcified section, showing regions of bone distinct from CEP and minimal CEP calcification. (Scale bars in (a) and (b) = 1 cm and in (c) and (d) = 0.5 mm)	30
Figure 11: CEP thickness in specimens, as measured on mid-sagittal MRI slices: (a) at different disc levels (b) at different anterior-posterior locations (C-center, A5, A10 = 5 and 10mm off the center towards anterior, P5, P10 = 5 and 10 mm off the center towards posterior). Letters on top of error bars indicate significance ($p < 0.005$) between measured locations.	31
Figure 12: Representative parameter maps at 7T: (A) T1 healthy, (B) T1 degenerate, (C) T2 healthy, and (D) T2 degenerate	39

Figure 13: Computed AF MRI signals and image contrast at 7T. (a) Normalized AF signal intensity according to Equation 6 over the full range of parameters TR and TE. (b) AF image contrast based on Equation 7 utilizing the maximum and minimum AF signal intensities. (c,d) Computed AF max (dashed), AF min (dotted) MRI signals, and image contrast (solid) at optimal TE (34 ms) (c) and versus TE at optimal TR (3000 ms) (d).	44
Figure 14: Representative images for (A) Radial, (B) Perinuclear, and (C) Circumferential tears. Left column shows raw TSE images and right shows 3D fusion volume rendering for each tear, respectively	46
Figure 15: Volume renderings of tears: (A-B) Radial and (C) Perinuclear/Radial – coronal views; (D-E) Circumferential – axial and coronal views of the same specimen.	47
Figure 16: Three matched images of a radial tear with different imaging: (a) fluoroscopic coronal view with radiographic dye, (b) T2 weighted TSE, and (c) T1 weighted FLASH.	47
Figure 17: MRI loading frame integration with Instron 8874	51
Figure 18: Effect of signal to noise ratio (SNR) on disc positioning within the MRI. Red arrow indicates the direction of lost signal within the RF coil. Clinically relevant anatomic orientation (Left Side) results in decreased posterior AF lamellar distinction (Orange Arrow). Lateral positioning of the disc (Right Side) enables the spine axis and B_0 (Blue Circle: dot indicates spine axis and B_0 direction) to be parallel, decreasing banding artifacts within the disc during image acquisition.	53
Figure 19: Integration of loading device with MRI and RF coil: (1) Placement of the transmit piece of the coil in the direction of B_0 on the MRI patient table, (2) loading frame slides over the transmit piece, and the (3) receive array slides directly over the disc's location.	54
Figure 20: Representative mid-axial MR images with (A) and without (B) loading frame. Signal to noise ratio (SNR) was measured using a region selected within the agarose (Green) to represent signal, as these samples come from different lumbar levels (Noise – White).	55
Figure 21: Representative image depicting area and length measurements in the Coronal and Sagittal plane to determine an average disc-height across the entire disc volume.	57
Figure 22: Representative (A) reference and (B) deformed labeled images. Labels cover the SVB, IVB, AF lamellae, and defects. Arrows indicate differences between reference and deformed images.	62
Figure 23: Overlay of reference and reconstructed labels. Arrows indicate regions where individual pixels are not aligned.	62
Figure 24: Reconstructed image displaying the effect of Gaussian (A) vs. B-spline (B) regularization technique. Note the unnatural swirling pattern within the NP and vertebrae in the Gaussian regularization.	65
Figure 25: Segmentation of AAF (red) and PAF (blue) using ITK-SNAP. Each region was defined based on visible lamellae within each IVD.	67
Figure 26: Representative plot on the effect of B-splines on AAF and PAF (A) Avg (B) St. dev. for axial and radial strain	69

Figure 27: Representative (A) radial and (B) axial strain maps generated in ANTs. (C) Radial strains and (D) Axial strains measured in the AAF, PAF, and IVD in ANTs (intact white, nucleotomy checkered) and Vic2D (intact black, nucleotomy striped), $\equiv p \leq 0.05$ & $\text{---} p \leq 0.10$	70
Figure 1: (A) Loading frame interfaced with Instron (red arrow), showing locking mechanism, segment grips, disc, and sliding tank (white arrows). (B) Loading frame integrated with RF coil (green arrows) in MRI. B0 = direction of magnetic field. ..	77
Figure 2: Images (A – C) are oriented to show coronal (left), axial (top-right), and sagittal (bottom) planes. (A) Representative MRI data set. (B) The volume used for strain analysis (pink). (C) Annulus fibrosus regions of interest defined in the mid-axial plane: A=anterior (red), A-L=anterior-lateral (green), L=lateral (purple), P-L=posterior-lateral (yellow), P=posterior (aqua).....	79
Figure 3: Pictorial representation of the image registration process, resultant warp field, and displacement map. The reference image is registered to the deformed image defining a warp field that prescribes how structures within the reference image are mapped to the deformed image. The deformation gradient tensor is applied to calculate the Lagrangian strain tensor.....	80
Figure 4: (A) Generation of lamellar structure labels using Sobel edge detection (red), shown in three planes. A representative label is shown in green. (B-C) Five identified lamellar labels, shown in mid-axial view and as 3D projections, respectively. Labels identified by white arrow.	82
Figure 5: Transformation of Cartesian coordinates to local disc coordinates using the disc's outer contour, scaled to intersect each voxel: (A) circumferential basis vectors defined by the contour's tangent; (B) radial basis vectors defined by the contour's normal. Note the complex vector directions imposed by the lamellar curvature.	85
Figure 6: Registration of a representative lamellar label (green), shown in coronal (left), axial (top-right), and sagittal (bottom) views. Difference between original and registered label is small (red), demonstrating good registration. Scale bar = 1cm ...	88
Figure 7: Axial strains for all discs obtained by manual measurement and by image registration, showing good agreement ($r^2=0.79$, $p<0.05$).....	89
Figure 8: Strain maps for 10% axial compression in a representative disc: (A) axial strain in coronal and sagittal views (left and right, respectively); (B) circumferential strain in axial view; (C) radial strain in axial view. Scale bar = 5 cm.	90
Figure 9: Mean (standard deviation) of AF regional strain at mid-disc height when loaded to 15% compression for (A) axial, (B) circumferential, and (C) radial strain. A=Anterior, A-L=Anterior-Lateral, L=Lateral, P=L=Posterior-Lateral, P=Posterior. Region locations are shown in Figure 2C. A solid line represents significance $p<0.05$ and dashed line a trend $0.05<p<0.10$	91
Figure 35: Representative segmentation process for defining disc regions: (A) Automatic NP (blue), inner AF (green), and outer AF (red), (B) Axial height division into superior, middle, and inferior disc regions, and (C) Subdivision into anterior: A, anterior-lateral: A-L, lateral: L, posterior-lateral: P-L, and posteriorL: P annulus within each axial height division. White scale bar = 1 cm.	107
Figure 36: Representative middle third disc height anterior outer annulus axial strain histogram (left) and strain color map (right). Each region exhibited a normal strain	

distribution. Mean strain values (solid black line) were reported for each region. One standard deviation (dashed black line) is shown for reference.	107
Figure 37: Reported regional (average \pm standard deviation) mean strain values for inferior (red) and superior (green) annulus fibrosus at 5%, 10%, and 15% axial compression for [A] – axial (E_{zz}), [B] – circumferential ($E_{\theta\theta}$), [C] – radial (E_{rr}), and [D] – in-plane shear ($E_{\theta r}$).	110
Figure 38: Regional strain bar charts (mean \pm standard deviation) comparing the inner (left-hand side) and outer (right-hand side) attachment region (solid) vs. middle (dotted) AF regions under 15% axial compression for axial [A / B], circumferential [C / D], radial [E / F], and in-plane shear [G / H] at 15% axial compression. Regions: anterior (A – red), anterior-lateral (A-L – green), lateral (L – blue), posterior-lateral (P-L – orange), and posterior (P – turquoise) annulus. Significance: solid line $p \leq 0.05$. Trend: dashed line $0.05 \leq p \leq 0.10$	113
Figure 39: Regional strain bar charts (mean \pm standard deviation) comparing the circumferential positions (A, A-L, L, P-L, and P) along the middle [left-hand side] and attachment region [right-hand side] disc height within the outer (solid) and inner (dashed) AF regions under 15% axial compression for axial [A / B], circumferential [C / D], radial [E / F], and in-plane shear [G / H] at 15% axial compression. Regions: anterior (A – red), anterior-lateral (A-L – green), lateral (L – blue), posterior-lateral (P-L – orange), and posterior (P – turquoise) annulus. Significance: solid line $p \leq 0.05$. Trend: dashed line $0.05 \leq p \leq 0.10$	116
Figure 40: Regional strain bar charts (mean \pm standard deviation) comparing the middle [left-hand side] and attachment region [right-hand side] disc height outer (solid) and inner (dashed) AF regions under 15% axial compression for axial [A / B], circumferential [C / D], radial [E / F], and in-plane shear [G / H] at 15% axial compression. Regions: anterior (A – red), anterior-lateral (A-L – green), lateral (L – blue), posterior-lateral (P-L – orange), and posterior (P – turquoise) annulus. Significance: solid line $p \leq 0.05$. Trend: dashed line $0.05 \leq p \leq 0.10$	118
Figure 41: Proof of concept balloon loading placement: (A) Unpressurized placement in center of NP under fluoroscopic guidance, (B) Pressurized balloon, and (C) Securing of balloon.	135
Figure 42: Proof of concept balloon visualization comparing an intact bovine motion segment to balloon pressurization: (A – B) Intact sagittal and coronal view and (C – D) Pressurized sagittal and coronal view.	136

CHAPTER 1 **Introduction**

The intervertebral disc (IVD) functions to permit motion of the spine while distributing the multidirectional loads experienced during daily activities, including tension, compression, torsion, and bending. Intervertebral disc degeneration widely afflicts the aging population, often manifesting itself in low back pain. This progressive and irreversible process causes deleterious changes to the disc's structural integrity, mechanical function, and nutritional pathways. The current surgical standard of care for painful disc degeneration is limited to disc removal, followed by superior and inferior vertebral body fusion or total disc replacement. Fusion results in a loss of motion and the ability to distribute load. Total disc replacement attempts to preserve mobility, but does not replicate the native disc load distribution characteristics. Quantification of internal IVD mechanics can improve knowledge of the effect of degeneration on disc mechanical function. This knowledge will provide crucial design criteria to better recapitulate healthy disc structure and function, and thus improve treatment options.

Measuring disc internal mechanics is a complicated challenge; in situ boundary condition replication is difficult with excised tissue testing samples. Motion segment testing permits the study of overall disc stress and strain behavior, but it does not present detail of the discs internal mechanics and interactions between its constituents. Prior experimental studies have attempted to study the IVD internal deformations; however they are limited to physical marker insertion or entire disc bisection, disrupting the discs structural integrity. Physical markers may move separately from the surrounding tissue and bisection depressurizes the NP, altering the AF mechanics. Magnetic resonance imaging (MRI) has recently been utilized to study IVD internal deformations, providing a

non-invasive technique to visualize the disc's substructures in two-dimensions (2D). This technique has only been applied to measure 2D strain under single loads. However, the IVD deforms in three-dimensions (3D). Single 2D images are not able to capture out-of-plane deformations, which are typical of a loaded disc. Work within this dissertation will develop techniques utilizing 3D MRI and image registration to allow intervertebral disc structural visualization and the quantification of its deformations under load. The overall objective of this dissertation is to measure the disc's 3D internal deformations when subjected to physiological loading, and more specifically, the effect of incremental axial deformations on the regional annulus fibrosus (AF) mechanics.

Chapter 2 will provide background on the IVD and explain the structure, composition, and mechanical function of healthy discs as well as the effects of degeneration. Additionally, a thorough review of internal deformations within the IVD, medical image analysis, and an introduction to Advanced Normalization Tools for image registration will be presented.

Current MRI techniques for visualizing the detailed IVD structure have been limited to single 2D images in one of the primary orthogonal planes: sagittal, coronal, or transverse. Chapter 3 will develop a 3D MRI sequence to visualize and distinguish the cartilaginous endplate (CEP). As the IVD degenerates, there is a loss of structural integrity causing the CEP to become sclerotic. The imaging techniques developed in Chapter 3 will then be applied to detecting and quantifying CEP thickness.

Chapter 4 will further visualize and distinguish the annulus fibrosus lamellae within the IVD. A 3D MRI sequence will enable the ability to differentiate between adjacent AF lamella facilitating the detection of deformities such as tears (radial,

circumferential, perinuclear), rim lesions, and Schmorl's nodes. The high-resolution 3D images will then be applied to the clinically relevant problem to non-invasively characterize and quantify annular deformities which are linked to low back pain and alter disc mechanics. The ability to visualize AF lamellae in 3D will be applied to track internal deformations within the disc under physiological loading in Chapters 7-8.

Chapter 5 describes an MRI compatible loading device designed to apply incremental amounts of axial compression, maintain disc hydration, and integrate with a curved RF coil. The developed loading frame will enable disc image acquisition in both a reference and deformed state with the optimized sequence from Chapter 4.

Image registration is considered a promising soft tissue (e.g., pulmonary and cardiovascular tissues, and ligament) strain analysis technique utilizing medical images. Chapter 6 will establish the use of Advanced Normalization Tools (ANTs), an image registration software for disc registration and optimize its parameters for 2D strain analysis. The use of manual segmentation tools will enable registration accuracy verification and strain measurements across user-defined regions. Registration strain measurements before and after nucleotomy will be compared with previously published texture correlation methods. Image registration optimization in 2D will be translated to 3D in chapters 7-8.

In Chapter 7, the high-resolution isotropic MR imaging sequence (Chapter 4), MRI safe loading frame (Chapter 5), and optimized image registration parameters (Chapter 6) will enable 3D internal deformation measurements in intact human discs. Intervertebral disc substructures work together and distribute multi-directional loading in compression, torsion, and bending. Data within the literature quantifying 3D internal

strain distributions under physiological loading is limited. Experimental whole-disc testing is limited to providing global disc load and deformation details, not yielding internal mechanics information. The effect of incremental amounts of axial compression on the regional strain variance will be reported along the mid-axial disc height.

Chapter 8 will expand upon the techniques developed in Chapters 3 – 6 to assess the internal regional strain properties of the IVD. Regional strain analysis has been limited to mid-axial, ex-vivo tissue testing, surface strain measurements, and two-dimensional internal analysis. A complete 3D internal strain analysis will be performed segmenting the disc into radial (i.e., inner and outer), circumferential (i.e., anterior, lateral, and posterior) and axial (i.e., inferior, medial, and superior) components.

The developed capabilities to measure 3D internal strain within the disc, the results from this dissertation, and proposed future studies involving the assessment of degeneration, different loading schemes, and clinical treatments will be discussed in Chapter 9.

CHAPTER 2 Background

2.1. Clinical Significance

Intervertebral disc (IVD) degeneration is a progressive disease strongly linked to low back pain (Frymoyer 1988, Andersson 1999, Adams 2004, Adams and Dolan 2005). This ailment debilitates more than 5 million Americans and is the second most frequent reason for physician visits (Deyo and Tsui-Wu 1987, Luo, Pietrobon et al. 2004). Its estimated \$100 billion societal cost in the United States (Katz 2006) mandates increased knowledge of the effects of this disease. Current surgical treatment options for painful disc degeneration is limited to disc removal, followed by either superior and inferior vertebral body fusion or total disc replacement (Schizas, Kulik et al.). Fusion results in a loss of motion and load distribution. Total disc replacement attempts to preserve mobility but does not replicate the native disc load distribution characteristics (Costi, Freeman et al.). Degeneration greatly affects the IVD and its constituents; it is associated with mechanical damage, biological degradation, and a loss of nutritional pathways (Martin, Boxell et al. 2002). Studies have shown that individuals, who undergo recurring compressive and torsional motion, have a higher incidence of disc degeneration compared to the general population (Kumar 2004, Hangai, Kaneoka et al. 2009). The factors that cause disease progression, including interactions of mechanical, compositional, structural, and cellular changes, are not well understood (Buckwalter and Mow 2000). The primary function of the disc is mechanical; however the understanding of disc internal deformations is limited to 2D work (O'Connell, Malhotra et al. , O'Connell, Vresilovic et al. , O'Connell, Johannessen et al. 2007) for a 3D structure. This

motivates the current study to examine the disc's 3D internal mechanics, quantify the effects of degeneration, and explore potential restorative techniques for AF mechanics.

2.2. Intervertebral Disc Structure

The spine is a column-like structure that is made up of alternating vertebral bodies (VB) that encapsulate the intervertebral discs (IVD) acellular soft-tissues. The IVD sub-structures (Figure 1) comprise of the nucleus pulposus (NP), annulus fibrosus (AF), and the cartilaginous endplates (CEP).

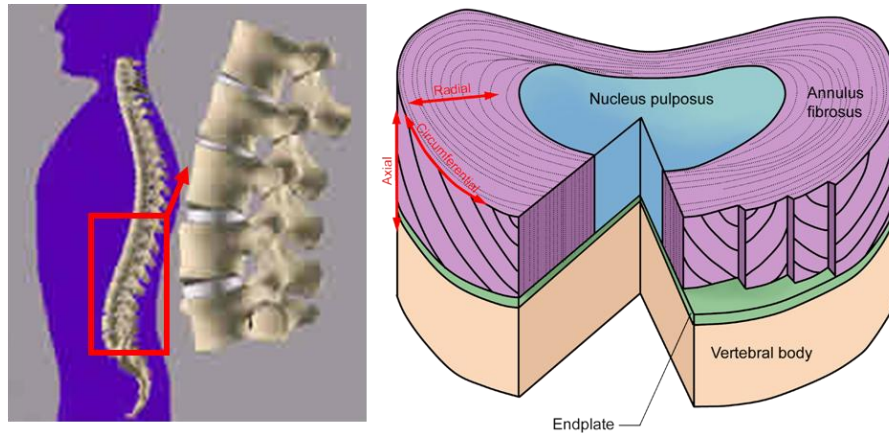


Figure 1: Representative lumbar spine image and the intervertebral disc sub-structures.

The NP is a hydrated, gel-like structure made up of water, proteoglycan, and type II-collagen that primarily aids the IVD during compression (Pearce, Grimmer et al. 1987). The NP is circumferentially encapsulated by the AF, which is made up of highly organized concentric lamellae. Each layer of lamellae has alternating fiber orientations 28° - 43° above and below the transverse plane (Marchand and Ahmed 1990); with the angle increasing from outer to inner AF. These fibers are made up of collagen bundles that are embedded in a matrix of proteoglycans and non-fibrillar collagens. Along the transition from the outer to inner AF, there is an increase in type II collagen and decrease

in type I collagen (Buckwalter 1995); resulting in less distinctive lamellae. Lamellae thickness varies by location (anterior/posterior/lateral) within the disc and becomes thicker towards the NP ranging from 140 – 520 μm (Marchand and Ahmed 1990). The AF outer lamella fibers are attached to the vertebra, while the inner lamellas merge with the CEP. The CEP is a very thin layer of hyaline-like cartilage, ranging from 450 – 800 μm positioned between the vertebral endplates and the NP (Roberts, Menage et al. 1989, Marchand and Ahmed 1990, Roberts, Menage et al. 1993, Moore 2000, Urban and Roberts 2003). It provides a mechanical barrier between the pressurized NP and the VB, acting as a gateway for nutrient transport from blood vessels into the disc (Roberts, Menage et al. 1993, Moore 2000, Urban and Roberts 2003). The structure and composition of the disc is strongly linked to its mechanical function (Buckwalter and Mow 2000).

2.3. Disc Mechanical Function

The intervertebral discs sub-structures (nucleus pulposus – NP, annulus fibrosus – AF, and cartilaginous endplate – CEP) function to distribute multi-directional loads, which are applied to the disc during daily activities that relate to tension, compression, torsion, and bending with stresses ranging from 0.1-2.3 MPa (Nachemson and Morris 1963, Wilke, Neef et al. 1999). The disc acts as a pressurized vessel, under load the NP exhibits viscoelastic properties (Iatridis, Weidenbaum et al. 1996, Iatridis, Setton et al. 1997), where the pressurization of the NP transfers hoop stresses radially to the anisotropic nonlinear AF. The alternating AF collagen fiber network permits resistance to bending and torsion while experiencing direct compression, plus radial and

circumferential stress from the NP bulging under physiological loading. The proposed work will focus on the internal strains seen during physiological compressive loads.

Motion-segment (bone-disc-bone) testing has been extensively performed in compression analyzing both the static (Stokes, Laible et al. , Koeller, Funke et al. 1984, Keller, Spengler et al. 1987, Cannella, Arthur et al. 2008) and dynamic (Adams and Hutton 1983, Liu, Njus et al. 1983, Hansson, Keller et al. 1987, Race, Broom et al. 2000, Riches, Dhillon et al. 2002, Johannessen, Vresilovic et al. 2004, van der Veen, van Dieen et al. 2007, Korecki, MacLean et al. 2008, Wang, Wu et al. 2008) responses of the disc. Disc height decreases under axial compression, resulting in an intradiscal pressure increase. The reported disc's compressive stiffness and modulus are 1.73 kN/mm and 3-10MPa (Nachemson, Schultz et al. 1979, Shea, Takeuchi et al. 1994, Beckstein, Sen et al. 2008) respectively. Under extended creep loading the NP transfers load to the annulus. The thin posterior annulus sustains high strains (Stokes 1987, Heuer, Schmidt et al. 2008) resulting in stress concentrations (Adams, McMillan et al. 1996, Edwards, Ordway et al. 2001). Radiographic measures have shown the endplate to bulge under increasing amounts of load (Holmes, Hukins et al. 1993).

Torsional shear modulus ranges between 2-9 MPa (Abumi, Panjabi et al. 1990, Elliott and Sarver 2004, Beckstein, Espinoza Orias et al. 2007) within the AF, where the disc experiences 1-2° of torsion in-vivo (Adams and Hutton 1981). Both the facet joints and annulus resist torsion (Shirazi-Adl 1994, Krismer, Haid et al. 1996) with the annulus bearing upwards of 77% (Yingling and McGill 1999). Surface strain measurements have shown the posterior lateral region to experience the greatest strain under torsion (Stokes 1987). The disc stiffens with age in torsion (Nachemson, Schultz et al. 1979) and is

linked to degeneration by the derangement of the AF lamellae at low magnitudes (Farfan 1969, Farfan, Cossette et al. 1970) and to increased risk of herniation under combined loading conditions (Drake, Aultman et al. 2005).

2.4. Disc Degeneration

Degeneration of the IVD causes progressive changes to the disc's structural integrity (Figure 2), mechanical function, and loss of nutritional pathways; the interactions of these changes are not well understood. During IVD degeneration the proteoglycans breakdown, resulting in a pressure loss and the ability to maintain hydration within the NP. This pressure and hydration loss subsequently causes a decrease in compressive stiffness (Buckwalter 1995, Nguyen, Johannessen et al. 2008). These changes in biochemical composition as a result of degeneration lead to a loss in fixed charge density (Urban and McMullin 1985, Urban and McMullin 1988). Consequently, the AF bears most of the loads within the IVD (Tsantrizos, Ito et al. 2005), leading to inward bulging of the AF (Brinckmann and Grootenboer 1991), disorganization, and thickening. Thickening increases collagen cross-linking (Pokharna and Phillips 1998), which can lead to annular tears (Thompson, Pearce et al. 1990, Adams 2004) and ultimately disc herniation. The inner AF undergoes an increase in collagen content with type II collagen fibrils becoming type I. (Weidenbaum and Iatridis 2006). This change in fibril type makes the distinction between NP and AF less apparent. Additionally, the CEP becomes sclerotic and loses vascular contact, which in turn causes decreased permeability, nutritional loss, and apoptosis of NP cells (Nachemson, Lewin et al. 1970, Bernick and Cailliet 1982,

Roberts, Urban et al. 1996, Grignon, Grignon et al. 2000, Bibby, Jones et al. 2001, Martin, Boxell et al. 2002, Adams and Roughley 2006, Accadbled, Laffosse et al. 2008, Raj 2008). These compositional changes of the IVD cause height loss, shifting the load towards the facets (Yang and King 1984) and placing high stresses on the AF leading to tears (Vernon-Roberts, Fazzalari et al. 1997, Lawrence, Greene et al. 2006).

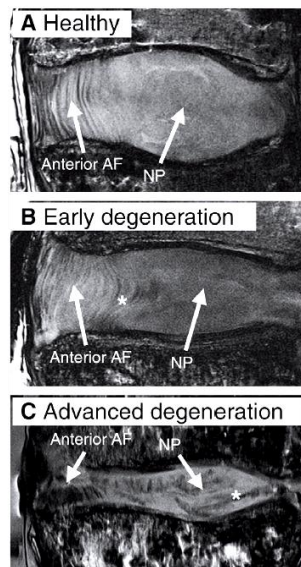


Figure 2: Magnetic resonance images illustrating different stages of human lumbar degeneration. (A) A healthy disc exhibiting distinct AF lamellae and central NP region. (B) A disc exhibiting early stages of degeneration, including moderate height reduction, decreased NP signal intensity and inward bulging of AF lamellae (*). (C) A disc exhibiting advanced stages of degeneration, including severely reduced height, large fissures (*) and generalized structural deterioration. (Smith, Nerurkar et al. 2011)

Annular defects have been categorized into classic tear categories: radial, circumferential, perinuclear (Osti, Vernon-Roberts et al. 1992, Vernon-Roberts, Moore et al. 2007) and other defects such as rim lesions and Schmorl's nodes (Figure 3). Radial tears typically initiate at the NP and radiate outward, occurring primarily in the posterior AF. Tears are closely associated with NP degeneration and

increased age (Osti, Vernon-Roberts et al. 1992, Vernon-Roberts, Fazzalari et al. 1997). Circumferential tears are the separation of lamellae and occur equally in the anterior and posterior AF, often concentrated in the outer regions (Osti, Vernon-Roberts et al. 1992, Vernon-Roberts, Fazzalari et al. 1997). Perinuclear tears are the separation of the NP from the AF and result in a cleft (Vernon-Roberts, Moore et al. 2007).

In cadaveric studies, morphological/histological sections and discograms (fluid contrast injected into the NP) have been used to quantify AF tears. Morphological sections are limited because they only view one disc slice, while tears occur in a complex 3D pattern (Vernon-Roberts, Fazzalari et al. 1997, Videman and Nurminen 2004).

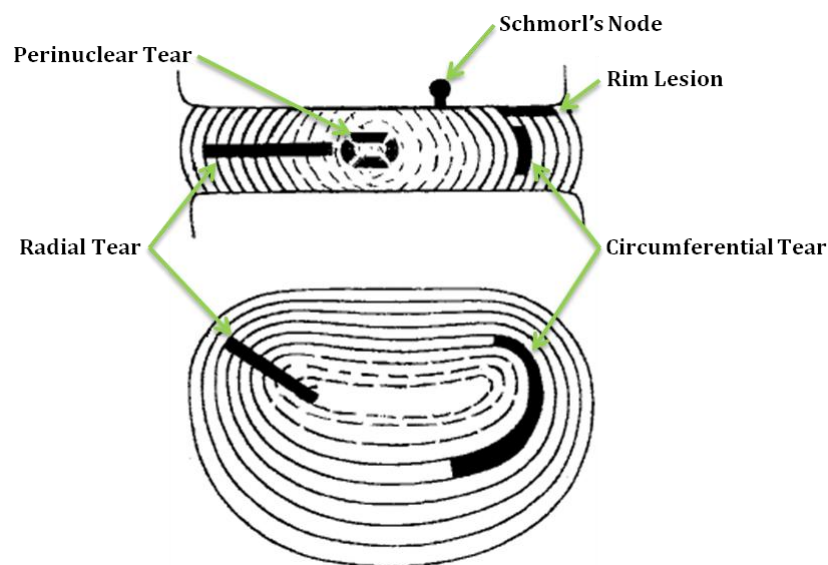


Figure 3: Representative annular and intervertebral disc defects. (Vernon-Roberts, Moore et al. 2007)

Discogram studies detect the presence of radial tears, but not their size or structure, and these studies do not detect circumferential tears (Adams, Dolan et al. 1986,

Kakitsubata, Theodorou et al. 2003, Videman and Nurminen 2004). The risk of a radial AF tears has been shown to be 60% in early adulthood and 100% by retirement age through an extensive discogram study of 157 cadaver spines. The risk of a full AF tear is 10% for 20 to 49 year olds and 35% for 50 to 59 year olds (Videman and Nurminen 2004). A comprehensive recent study using multiple histological sections of L4-L5 quantified the incidence concentric tears to be ~100% between ages 10 and 80 years (Vernon-Roberts, Moore et al. 2007). The incidence of perinuclear tears was also high at ~90% across all ages. Posterior radial tears increase from 70% incidence in those 10-30 years to 85% within the 51-89 year group (Vernon-Roberts, Moore et al. 2007). Rim lesions occur at the junction of the AF and vertebral endplate and are related to trauma, rather than degeneration. Rim lesion data shows 30% incidence at age 30 and 90% at age 80 (Vernon-Roberts, Moore et al. 2007). Schmorl's nodes are herniations of the disc into the VB (Resnick and Niwayama 1978). Reported frequency in the literature is varied (Hilton, Ball et al. 1976, Hansson and Roos 1983, Hamanishi, Kawabata et al. 1994, Stabler, Bellan et al. 1997).

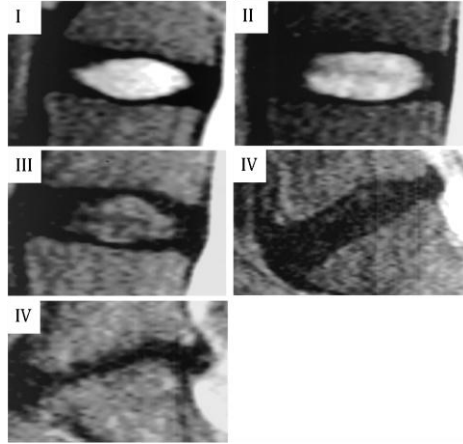


Figure 4: Pfirrmann grading scale displaying degenerative changes visualized in MR (Pfirrmann, Metzdorf et al. 2001).

The degenerative IVD structural and compositional changes can be visualized with MR imaging. Images illustrate a decrease in signal intensity, disc height narrowing, and osteophytes on the vertebral bodies (Pfirrmann, Metzdorf et al. 2001). Pfirrmann *et al.* established a qualitative graded scale (Figure 4) of increasing degeneration, where non-degenerate discs are grades I-II, moderately degenerate are grades III-IV, and severely degenerate grade V (Pfirrmann, Metzdorf et al. 2001).

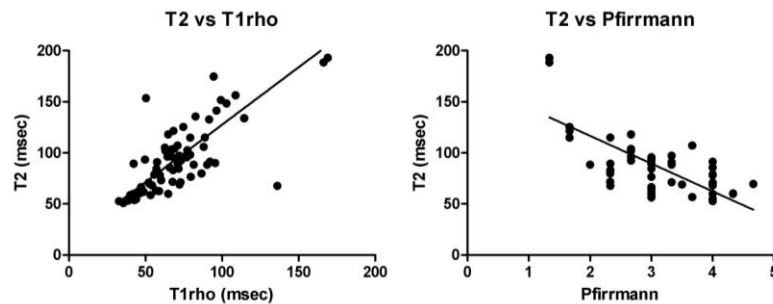


Figure 5: T2 correlations to T1p and Pfirrmann from Elliot Lab lumbar spine database collected over several years for a multitude of studies

Since degeneration is a continuous process, quantitative MR mapping techniques (T1p and T2) have been linked to degeneration through changes in water and

proteoglycan content (Blumenkrantz, Zuo et al. , Borthakur, Maurer et al. , Marinelli, Haughton et al. , Takashima, Takebayashi et al. , Welsch, Trattnig et al. , Zuo, Joseph et al. , Blumenkrantz, Li et al. 2006, Johannessen, Auerbach et al. 2006, Perry, Haughton et al. 2006, Watanabe, Benneker et al. 2007, Nguyen, Johannessen et al. 2008, Marinelli, Haughton et al. 2009). T2 mapping will be used within this study because it is more repeatable and is correlated to both Pfirrmann grade and T1 ρ score (Figure 5) (Blumenkrantz, Zuo et al.).

2.5. Internal Deformations

Internal deformations of IVD strains have been measured through various optical and radiographic techniques (Seroussi, Krag et al. 1989, Meakin and Hukins 2000, Kusaka, Nakajima et al. 2001, Meakin, Redpath et al. 2001, Tsantrizos, Ito et al. 2005, Ho, Kelly et al. 2006, Costi, Stokes et al. 2007). Physical markers were inserted to track displacements within the disc. Markers included metal beads (Seroussi, Krag et al. 1989), thin wires (Tsantrizos, Ito et al. 2005, Costi, Stokes et al. 2007), or nylon rods (Kusaka, Nakajima et al. 2001). These markers offered limited accuracy since they were able move separately from the structure of the disc. This limitation was improved by the use of Alcian blue stain dots to track the displacements of a sagittally bisected disc against transparent Plexiglas (Meakin and Hukins 2000, Meakin, Redpath et al. 2001, Ho, Kelly et al. 2006); however, bisection depressurizes the disc. The recent application of the commercial texture correlation software Vic2D (Correlated Solutions Inc: Columbia, SC) to MR images has permitted non-invasive internal deformation measurements to be made

in 2D within the sagittal and coronal plane of the disc (O'Connell, Malhotra et al. , O'Connell, Vresilovic et al. , O'Connell, Johannessen et al. 2007).

O'Connell *et al.* utilized a turbo spin echo (TSE) with TR/TE = 3000/113 ms respectively, producing T2-weighted 2D mid-sagittal/coronal MR images with in-plane resolution of 234 $\mu\text{m}/\text{pixel}$ and 3mm slice thickness on a 3T clinical MRI scanner (O'Connell, Johannessen et al. 2007). Spin-echo based sequences have been widely used for MR imaging of the intervertebral disc (Haughton 2004) because they are less susceptible to inhomogeneity's in the magnetic field. T2-weighting an image with a long echo time (TE) and long repetition time (TR) provides brighter signal for high water content soft tissues and darker for fat predominant tissues. Texture correlation strain measurements (resolution of $1/20^{\text{th}}$ pixel = 11.7 μm) were validated against displacement measurements across the entire disc and also against finite element studies (O'Connell, Johannessen et al. 2007). Under axial compression it was found that compressive and radially tensile strains increased with degeneration (O'Connell, Vresilovic et al.). The posterior AF experienced the highest regional strain and did not correlate with degeneration, indicating that the posterior region undergoes high loads throughout life (O'Connell, Vresilovic et al.). The use of MRI to measure internal deformations permits the study of clinical treatments such as nucleotomy, which increases compressive AF strains while decreasing radial strain (O'Connell, Malhotra et al.). Despite significant technical improvements, these studies are limited to 2D strain measurements for a 3D structure. It is difficult to limit out of plane motion; the 3D techniques developed in this thesis will mitigate these limitations. Texture correlation has been shown to produce strain inaccuracies due to the in-homogeneity of the IVDs native texture as visualized in

MR images (Gilchrist, Xia et al. 2004). Recognition of such limitations has directed the implementation of image registration to perform strain analysis on medical images (Phatak, Sun et al. 2007). This process produces comparable results to texture correlation (Hardisty, Akens et al. , Villemure, Cloutier et al. 2007). A non-rigid image registration method was employed by Reiter *et al.* to calculate mid-sagittal strain after creep loading (Reiter, Fathallah et al. 2012). Displacement encoded MRI, an image tagging method that enables direct displacement measurements from MR data, was used by Chan and Neu to calculate strain across the entire disc under cyclic loading (Chan and Neu 2013). These studies utilized MR phantoms (Chan and Neu 2013) or computer generated deformations (Reiter, Fathallah et al. 2012) to verify strain measurements. However, experimental specific verification can provide a better sense of what is actually occurring within the disc (ground truth). Image registration and the application of overlap statistics with segmentations will provide strain analysis of the entire disc and accurate disc-specific reportable strain resolution in Chapter 6-8.

2.6. Medical Image Analysis and Registration Applications

Quantitative image analysis including texture correlation, digital volume correlation and image registration (Liang, Zhu et al. , O'Connell, Malhotra et al. , O'Connell, Vresilovic et al. , Tustison, Cook et al. , Weiss, Rabbitt et al. 1998, Bay, Smith et al. 1999, Bay 2001, Veress, Weiss et al. 2002, Tustison, Davila-Roman et al. 2003, Veress, Gullberg et al. 2005, Tustison and Amini 2006, Chandrashekara, Mohiaddin et al. 2007, Liu and Morgan 2007, O'Connell, Johannessen et al. 2007, Phatak, Sun et al. 2007, Phatak, Maas et al. 2009, Tustison, Avants et al. 2009) has been

extensively used to measure strain from various biomedical imaging modalities. Texture correlation is a pattern-matching algorithm that compares random patterns of pixel intensities between two images, calculating displacements between individual pixels in corresponding images. Digital volume correlation is an adjunct to digital image correlation, a form of texture correlation utilizing 3D images to track microstructural feature movement within specimens (Bay, Smith et al. 1999, Bay 2001, Liu and Morgan 2007). Image registration is the process of finding a transformation (warp field) which can map points from a reference image (original) to a different image (deformed) (Ng and Ibanez 2004), this technique has been widely applied to medical images.

Image registration permits various imaging modalities, including X-Ray, CT, and MRI which can be spatially aligned to correlate data (Maintz and Viergever 1998). The wide applicability of image registration enables physicians to quantitatively detect subtle changes between images, facilitate identification and localization of brain lesions for surgical guidance (Ng and Ibanez 2004), assess treatment effectiveness pre- and post-intervention and tumor/disease development (Maintz and Viergever 1998, Ng and Ibanez 2004), hippocampus disease valuation via template building for population studies (Avants, Yushkevich et al.), and measuring ligament, pulmonary, and cardiovascular tissue mechanics (Liang, Zhu et al. , Tustison, Cook et al. , Weiss, Rabbitt et al. 1998, Veress, Weiss et al. 2002, Tustison, Davila-Roman et al. 2003, Veress, Gullberg et al. 2005, Tustison and Amini 2006, Chandrashekara, Mohiaddin et al. 2007, Phatak, Sun et al. 2007, Phatak, Maas et al. 2009, Tustison, Avants et al. 2009). Parameter selection is a critical process when performing image registration in a new tissue, in Chapter 6-7 these techniques will be applied to the intervertebral disc.

2.7. Advanced Normalization Tools Image Registration Parameters

Registrations are performed using either features or image intensity. Features include specific points and landmarks or binary structures within the native anatomy, which can be segmented as curves, surfaces, or volumes. Image intensity refers to the image grayscale patterns. Landmark- and segmentation- based registration methods align images, minimizing the distance between features. Intensity-based registrations minimize a cost function that measures the similarity of the intensity between corresponding images (Ng and Ibanez 2004). Advanced Normalization Tools (ANTs) is a multi-resolution approach encompassing landmark-, segmentation-, and intensity- based registration techniques.

The registration process is guided by 3 main parametric variables: transformation model, regularization technique, and the similarity metric to define the resultant warp field (Figure 6). The transformation model determines how one image is mapped into or aligned with another image. Multiple transformation models exist to account for varying degrees of differentiation between the images registered. During registration, ANTs has the ability to account for rigid translation and rotation to align one image with another. Deformable or non-rigid models (Diffeomorphic or Elastic) are more flexible, modeling and deforming the image as a continuum (e.g. elastic material, viscous fluid, etc.) (Avants and Gee 2004). During registration, the transformation model deforms the images on an overlaid grid or warp field. Generally, points that fall along gridlines are matched directly to points in the second image, and thus the grayscale intensity is known. The regularization technique interpolates the pixel intensity of points mapped between gridlines (Ng and Ibanez 2004). ANTs primarily uses Gaussian and B-spline (Lehmann,

Gonner et al. 1999, Tustison, Avants et al. 2009) interpolators, which use Gaussian distributions and basis functions respectively, to assign intensity values. The choice of regularization as well as its measures (e.g. size of variance and number of splines) affects the smoothness of the mapping. Similarity metrics are statistical measures used to quantify the resemblance between the pixel intensity patterns in both images. Different statistical measures should be used if pixel intensities and patterns are consistent or vary across images. The metric choice is thus dependent on whether one or multiple imaging modalities are used. ANTs offers several similarity metrics and is capable of both mono- and multi- modality registrations. Mean squared difference (MSQ) and fast cross correlation (CC) are ideal for mono-modality registrations, which are employed in this work.

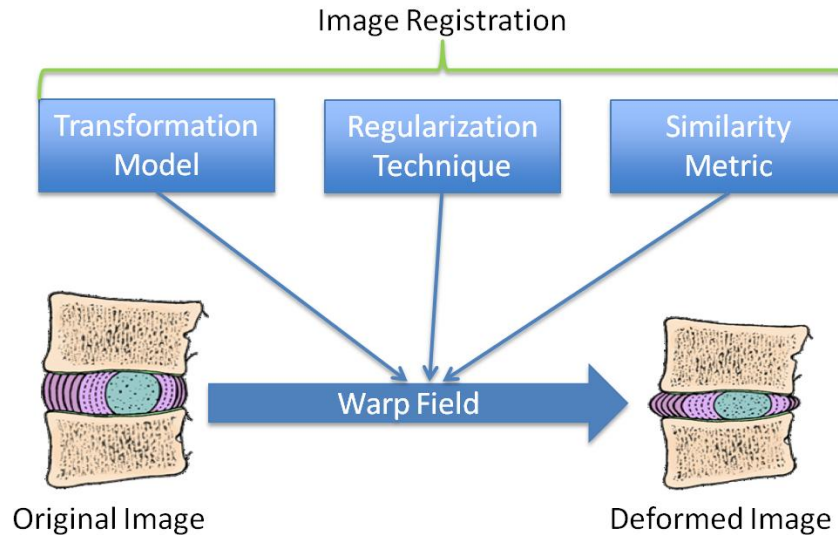


Figure 6: Graphical overview of image registration

CHAPTER 3 **Cartilaginous Endplate Geometry**

3.1. **Introduction**

The intervertebral disc has three distinct anatomical regions: the central nucleus pulposus (NP), the surrounding annulus fibrosus (AF), and centrally positioned cartilaginous endplates (CEP). These CEPs are distinct from the adjacent vertebral endplates, which are composed of cortical bone (Francois, Bywaters et al. 1985, Roberts, Menage et al. 1989, Raj 2008). The CEP is an approximately 600 μm thick layer of hyaline cartilage positioned between the vertebral endplate and NP (Roberts, Menage et al. 1989). It functions both as a mechanical barrier between the pressurized NP and the vertebral bone, as well as a gateway for nutrient transport into the disc from adjacent blood vessels (Crock and Goldwasser 1984, Roberts, Menage et al. 1993, Moore 2000, Urban and Roberts 2003).

Intervertebral disc degeneration causes the CEP to become sclerotic, lose vascular contact, and exhibit decreased permeability (Nachemson, Lewin et al. 1970, Bernick and Cailliet 1982, Roberts, Urban et al. 1996, Grignon, Grignon et al. 2000, Bibby, Jones et al. 2001, Benneker, Heini et al. 2005, Accadbled, Laffosse et al. 2008). This process is considered to contribute to degeneration by reducing diffusion of nutrients to cells of the NP (Ariga, Miyamoto et al. 2001, Martin, Boxell et al. 2002, Adams and Roughley 2006, Raj 2008).

The literature is replete with cadaveric studies using histology or gross sections depicting CEP thickness (Roberts, Menage et al. 1993, Vernon-Roberts, Fazzalari et al. 1997, Videman and Nurminen 2004, Bae, Statum et al. 2013). However, even multiple histological sections cannot reconstruct the complex 3D CEP geometry; as a result, no

accurate quantitative techniques for characterization of the 3D human CEP. Magnetic resonance imaging (MRI) is a non-invasive, non-ionizing imaging modality well known for its superior soft tissue contrast, making it ideal for disc applications including anatomy, composition, and stage of degeneration through a number techniques (e.g., T1 ρ - and T2-weighted images) (Lyons, Eisenstein et al. 1981, Pfirrmann, Metzdorf et al. 2001, Antoniou, Mwale et al. 2006, Johannessen, Auerbach et al. 2006). Application of MRI to the study of the intervertebral disc has to date focused predominantly on the composition of the NP and AF. Few studies have examined the CEP, therefore the objective of this chapter is to develop MRI techniques to visualize and quantify the CEPs geometric. In-order to visualize the thin CEP and accurately measure its thickness, a sufficiently high resolution (small voxels) and appropriately matched MRI parameters are required.

3.2. Materials and Methods

3.2.1. Intervertebral disc MRI parameter measurement

In this chapter, a T1weighted 3D FLASH (fast low-angle shot) sequence was chosen for CEP imaging. In the FLASH sequence, transverse magnetization is spoiled and the steady-state longitudinal magnetization depends on T1 and the flip angle. Flip angle is the angle at which the net magnetization is rotated relative to the primary magnetic field (B_0) by application of an excitation pulse. The sequences parameters repetition time (TR) and flip angle thus determine the T1 contrast in the FLASH sequence and were optimized in this study using an analytical model. Repetition time (TR) is the amount of time between successive pulses applied during image acquisition. Optimized sequence parameters TR and flip angle will yield sufficient image contrast to distinguish the CEP from its adjacent tissue.

The first step in MR image sequence optimization involves determining the MRI tissue specific properties. To achieve a T1 weighted image, the T1 relaxation time must be determined. T1 relaxation time (measured in milliseconds) known, as longitudinal relaxation time is a measure of the time required for a tissues protons to realign with B_0 . T1 values of NP, CEP, and AF lamellae were measured in a representative healthy and degenerate cadaveric lumbar disc (Grade = 2.3/5) (Pfirrmann, Metzdorf et al. 2001) at 7T magnetic field strength. T1 was measured using a fully relaxed (TR = 5100 ms) 2D spin echo inversion recovery pulse sequence with ten inversion times (TI = 33 – 5000 ms). T1 maps were generated (Figure 7) by fitting data on a pixel-by-pixel basis to its respective exponential decay function (Equation 1

Equation 1). Averaging 900 or more pixels within center of the NP, anterior and posterior AF, and CEP determined representative T1 values of each disc substructure.

$$\text{Equation 1: } I(TI) = I_0 \left(1 - 2e^{-TI/T1} \right)$$

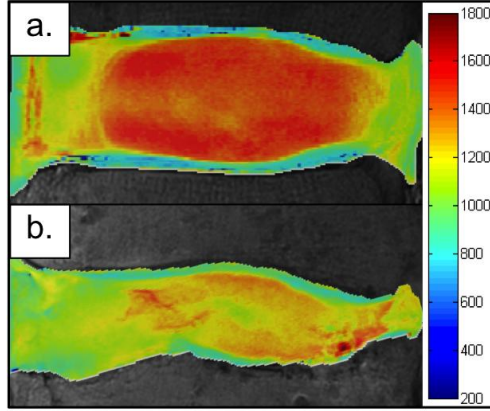


Figure 7: Representative T1 parameter maps at 7T: (A) T1 healthy, (B) T1 degenerate

3.2.2. Optimization of CEP image contrast

In order to attain pulse sequence parameters with optimized contrast in the CEP, MRI signal intensity and image contrast were simulated using an analytical MRI pulse sequence equation prior to imaging. The T1 contrast of the FLASH sequence is a function only of TR and flip angle in the limit of a short echo time (TE), and the dependence of MRI signal intensity upon flip angle, TR, and T1 is given by Equation 2 where A is the equilibrium magnetization reduced by T2 relaxation and α is the flip angle (Helms, Dathe et al. 2008, Dathe and Helms 2010). Echo time (TE) corresponds to the time between RF pulse and the peak in signal. T2 relaxation time known, as transverse relaxation is a measure of time required for a tissues protons to dissipate energy to their surrounding nuclei perpendicular to B_0 .

$$\text{Equation 2: } MRI\text{signal} = A \sin \alpha \frac{1 - \exp(-TR/T1)}{1 - \cos \alpha \exp(-TR/T1)}$$

This equation was used to analyze the signal dependence on flip angle and TR, the primary adjustable imaging parameters in this application. Using the experimentally determined mean T1 and I_0 values for NP and CEP, normalized MRI signals (Equation 2) for each substructure were plotted versus flip angle and TR. The image contrast (signal difference) between NP and CEP (Equation 3), normalized to maximize the signal intensity of CEP, was plotted versus flip angle and TR for the full range of possible parameter values according to ex vivo MR imaging

$$\text{Equation 3: } \Delta_{CEP} = \left| \frac{\text{Signal}_{NP} - \text{Signal}_{CEP}}{1 - \text{Signal}_{CEP}} \right|$$

3.2.3. Cartilaginous Endplate Imaging

Specimens for CEP imaging were prepared from 11 cadaveric human lumbar spines ($n = 17$ discs, age: 57.7 ± 13.3). While for some subjects 2–3 levels were used from a single spine, consistent with common practice in the literature (O'Connell, Vresilovic et al. , Iatridis, Setton et al. 1997, Rodriguez, Slichter et al. 2011), these discs were assumed to be independent samples and post hoc statistical analysis confirmed no subject dependence on CEP height. Each whole spine was first scanned with a mid-sagittal T2-weighted turbo spin echo imaging sequence for routine grading of degenerative state (Pfirrmann, Metzdorf et al. 2001, Johannessen, Auerbach et al. 2006). The integer grade from five individual examiners was averaged (Grade: 2.8 ± 0.7). Lumbar spines were then dissected into bone-disc-bone segments with posterior elements removed and sealed in airtight freezer bags to avoid dehydration during imaging. The sealed segments were then embedded in 2 % agarose gel for immobilization and to reduce image distortion at tissue edges due to the tissue/air mismatch in magnetic susceptibility (Schenck 1996).

For protocol optimization, the flip angle and TR that provided the best optimal NP-CEP contrast was selected using the analytical model simulation. All imaging was done in a Siemens Magnetom 7T scanner (Siemens Medical Solutions, Erlangen, Germany) using a 4-channel ankle coil (Insight MRI) (Wright, Lemdiasov et al. 2011). Due to the thinness of the endplate, a voxel size of $200\ \mu\text{m}^3$ was chosen. Imaging parameters were TR = 9 ms, TE=3.7ms, flip angle=20°, $(0.2\ \text{mm})^3$ isotropic resolution, matrix = 320 x 320, and fat suppression. Scan time was 3 min per disc.

3.2.4. CEP Histology and endplate thickness quantification

Histological analysis was performed to confirm that the structure visualized using MRI was indeed the CEP and to compare CEP thickness measurements with measurements from site-matched MR images. Two adjacent 8 mm biopsy punches, comprising vertebral bone, the CEP and the NP, were taken from a disc (63 years, male, L2L3, Grade: 2.6), which had previously been imaged as described above, and an optical image of the specimen was taken. These $200\ \mu\text{m}^3$ isotropic MRI data and photograph were later co-registered to confirm the location of the punches. Both punches were fixed in buffered 10% formalin overnight. One punch was then decalcified overnight in formic acid/EDTA. Twenty-micron sections were cut on a cryostat, and double stained with Alcian blue and picosirius red to demonstrate glycosaminoglycans and collagen, respectively, and imaged using bright field microscopy. The other punch was sectioned in a similar way, but without prior decalcification. These sections were then stained using the von Kossa method to demonstrate calcium deposits and imaged using differential interference contrast microscopy (Eclipse 90i; Nikon; Tokyo, Japan).

To compare MRI-based CEP measurements with a histological standard, three 4 mm diameter CEP samples were punched within the inferior endplate for a single disc (75 years, male, L2L3, Grade: 2.0), sectioned on a cryostat, and the CEP thickness measured at three evenly spaced intervals across the plug. Virtual plugs were generated from the MR data by co-registering with an optical image of the vertebral surface and site-matched CEP thickness measurements were made.

Images were imported into OsiriX software and evaluated for CEP contrast in comparison to the surrounding structures, for morphology three dimensions thickness. MRI data had isotropic resolution and, therefore, could be viewed in arbitrary image planes using multi-planar reformatting. The CEP thickness was measured for the superior and inferior CEP along the mid-sagittal plane at five locations (center, 5 and 10 mm off the center towards anterior and 5 and 10 mm off the center towards posterior). Average thicknesses across specimens were measured by hand within OsiriX for each location and each disc level.

The CEP thickness measurements were evaluated using a two-way ANOVA with repeated measures, where the factors were disc level (L1L2, L2L3, L3L4, L4L5, L5S1) and anterior-posterior disc location (center, 5 and 10 mm off the center towards anterior, and 5 and 10 mm off the center towards posterior). Significance was set at $p < 0.05$. A post hoc Bonferonni test was performed when significance was detected resulting in significance at $p < 0.005$.

3.3. Results

Average T1 values (\pm standard deviation) from the T1 parameter map (Figure 7) of each disc substructure obtained at 7T are presented for a representative healthy and degenerate disc substructures in Table 1. These T1 values were used in Equation 2 and Equation 3 to calculate signal intensity and determine optimal pulse sequence parameters for NP-CEP image contrast (D_{CEP}) (Figure 8). Figure 8a shows a contour plot of D_{CEP} covering the exhaustive range of flip angles ($0-180^\circ$) and TR values ($0-6,000$ ms). However, only a small region corresponding to short TR (dotted box in Figure 8a), where scan time is reasonable for future in vivo applications, was considered in selecting the optimal sequence parameters (Figure 8b), and the optimal flip angle and TR were identified (asterisk in Figure 8b).

Grade	Region	T1
Healthy	AF	1270 ± 80
	NP	1510 ± 50
	CEP	775 ± 75
Degenerate	AF	1100 ± 43
	NP	1300 ± 65
	CEP	840 ± 32

Table 1: Average (\pm standard deviation) T1 values for a healthy and degenerate disc substructures.

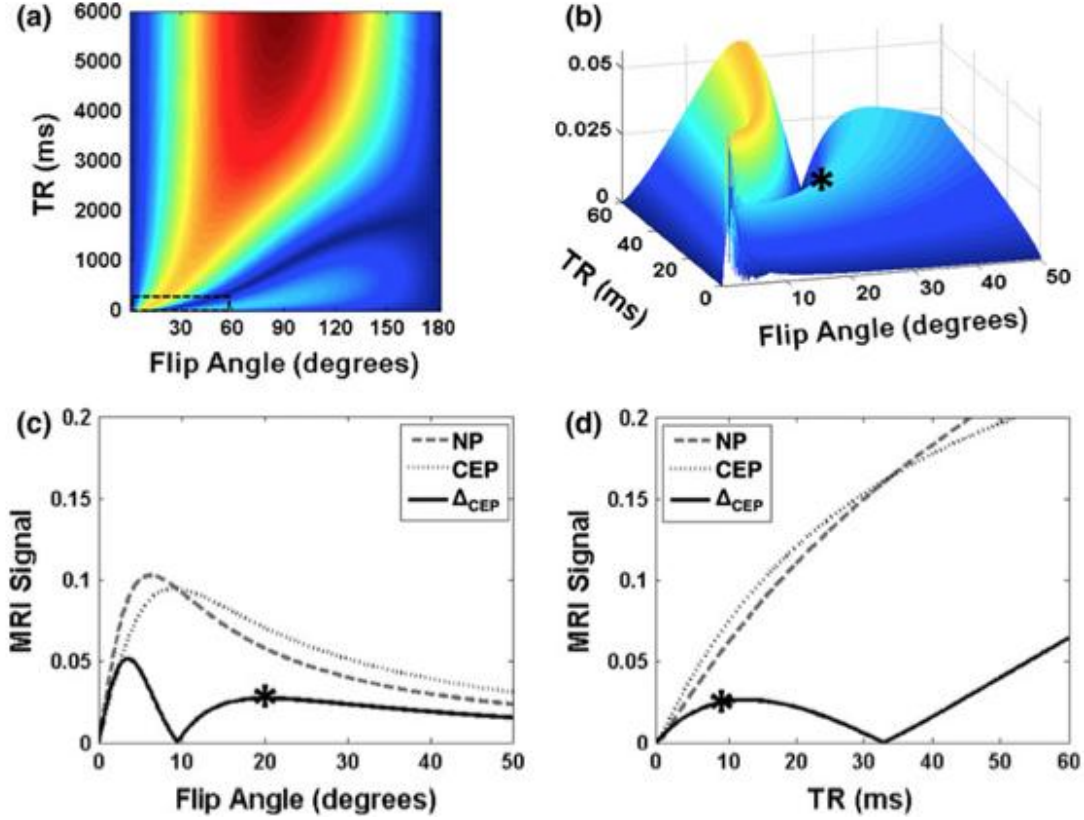


Figure 8: Computed MRI signals and image contrast at 7T: (a) NP-CEP image contrast (Δ_{CEP}) according to Equation 3, over the full range of the parameters flip angle and TR. (b) Close-up 3D view within the small dashed box in (a). Asterisk (*) indicates the point chosen as optimal. (c,d) Computed NP (dashed) and CEP (dotted) MRI signals, and image contrast (Δ_{CEP} , solid) versus flip angle at optimal TR (9 ms) (c) and versus TR at optimal flip angle (20°) (d).

A flip angle of 20° with a TR of 9 ms yielded the highest contrast between the CEP and NP (Figure 8c, d). Note that even though a flip angle of 3° yields higher signal difference between the NP and CEP; this was not chosen because for angles less than 5° the MR signal changes rapidly, resulting in a smaller range of optimal image contrast. Furthermore, at 5° or less the absolute signal intensity of the CEP is lower than it is at 20°.

The optimized T1-weighted 3D FLASH sequence yielded good contrast between the NP and CEP (Figure 9). The images showed clear distinction of the CEP (arrows). Multi-

planar reformatting was done to elucidate the three-dimensional extent and overall shape of the CEP. Mean projections of an axial slab (1.3 mm) of the CEP showed that the shape and size of the CEP can vary considerably between specimens (Figure 9).

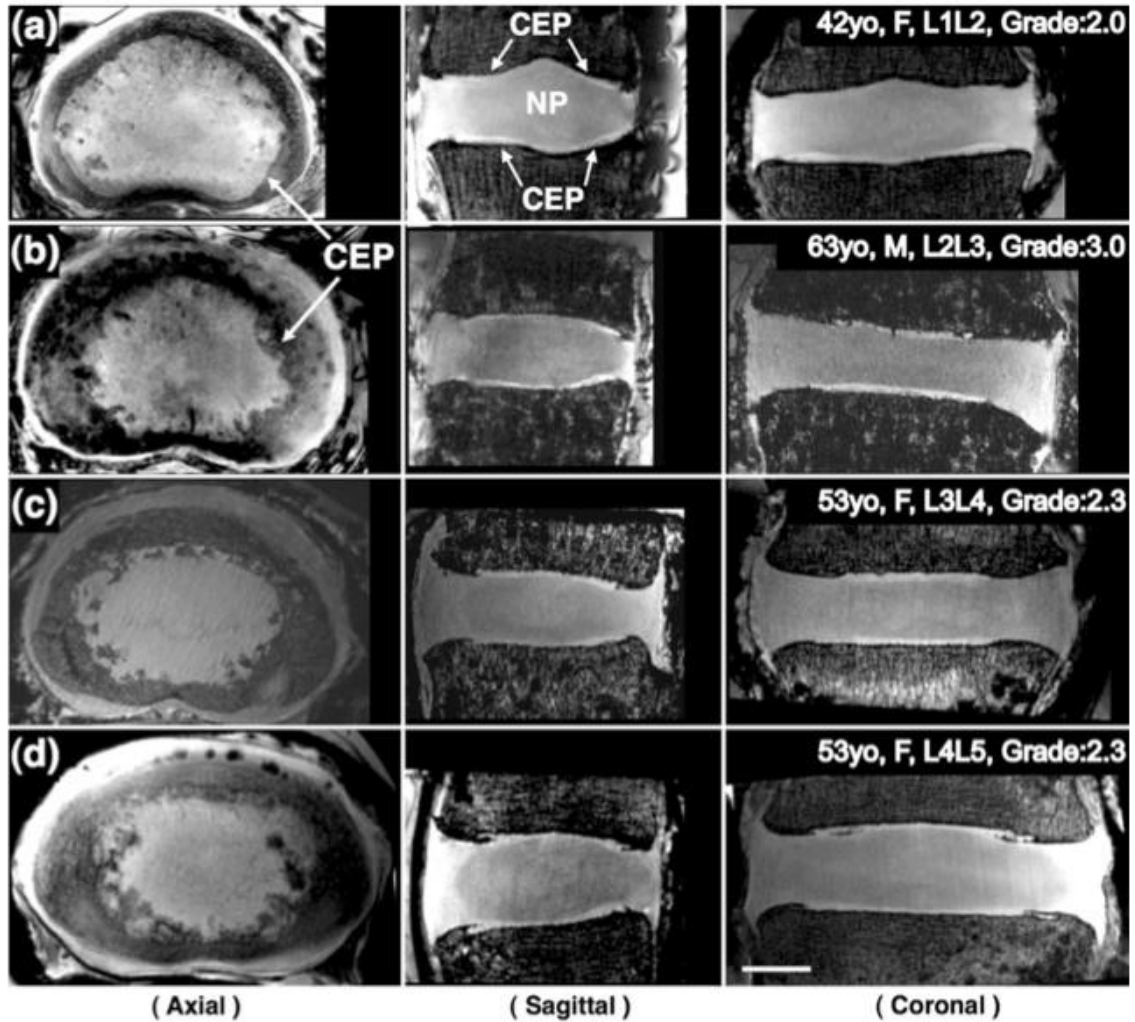


Figure 9: MRI images of four different specimens with 200 μm isotropic resolution acquired at 7T. Three-plane views reformatted from the same isotropic dataset of each specimen clearly demonstrate the CEP's (*arrows*) clearly, which are located between the vertebral body and the NP. Axial views show that the shape and size of the CEP can vary considerably for different subjects and levels: (a) 47 years, female, L1L2; (b) 63 years, male, L2L3; (c) 53 years, female, L3L4; (d) 53 years, female, L4L5. *Scale bar* = 1 cm

Histology confirmed that the structures observed in MR images were indeed CEP

(locations of histological samples are shown in Figure 10a, b). Alcian blue and picrosirius

red histology successfully illustrated different anatomic regions (i.e., trabecular bone, bony endplate, CEP, and NP) (Figure 10c). Von Kossa staining showed calcification of the adjacent vertebral trabecular bone and a very thin layer of cortical bone; however, with the exception of a very small number of cell lacunae at the bony interface, there was no calcification within the CEP itself (Figure 10d). To address accuracy of our MRI-based CEP thickness quantitative measurements of CEP thickness made from histological sections were 0.42 ± 0.69 mm. These CEP dimensions were of the same magnitude to those measured using MRI on site-matched virtual plugs, which were 0.45 ± 0.12 mm.

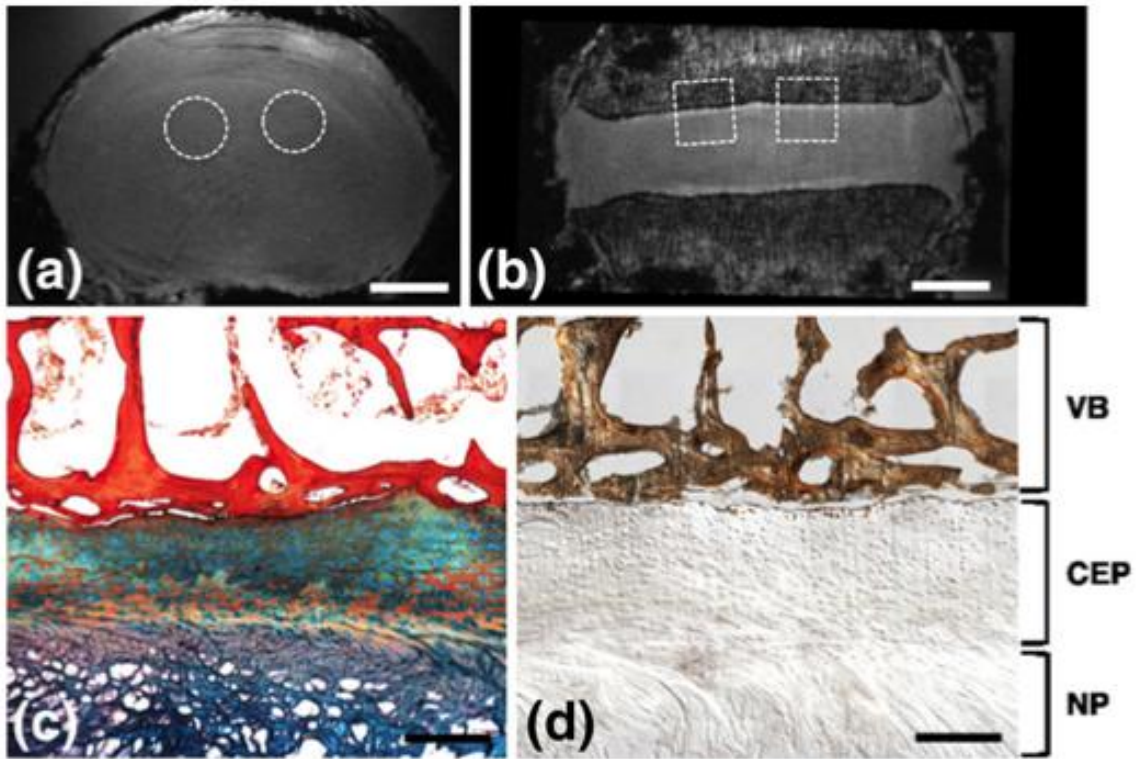


Figure 10: MRI and histology images of the same specimen (63 years, male, L2L3, Grade 2.6). Axial (a) and coronal (b) FLASH MRI of the whole disc, showing approximate locations of biopsy punches used for histological analysis. (c) Representative histology section of the CEP stained with Alcian blue (glycosaminoglycans) and picrosirius red (collagen) showing adjacent NP and vertebral bone. (d) Von Kossa staining of an undecalcified section, showing regions of bone distinct from CEP and minimal CEP calcification. (Scale bars in (a) and (b) = 1 cm and in (c) and (d) = 0.5 mm)

The thickness of the CEP at the mid-sagittal plane and its correlation with disc level and anterior-posterior location were evaluated in the specimen MRI data. Across all disc levels and locations, the mean CEP thickness was 0.77 ± 0.24 mm similar to that of (Roberts, Menage et al. 1989) 0.62 ± 0.29 mm.

No significant difference in CEP thickness was observed across disc levels (Figure 11a). There were significant effects of anterior–posterior location on CEP thickness (Figure 11b), where the minimum thickness was at the center of the disc (0.54 ± 0.12 mm, averaged across all lumbar levels). The thickness at the center was 23% less than the 0.5 cm anterior–posterior location and 44% less than the 1.0 cm anterior–posterior location ($p < 0.005$), resulting in a “V” shaped pattern across the disc (Figure 11b). There was no statistical interaction between level and anterior-posterior location for the CEP thickness measurements.

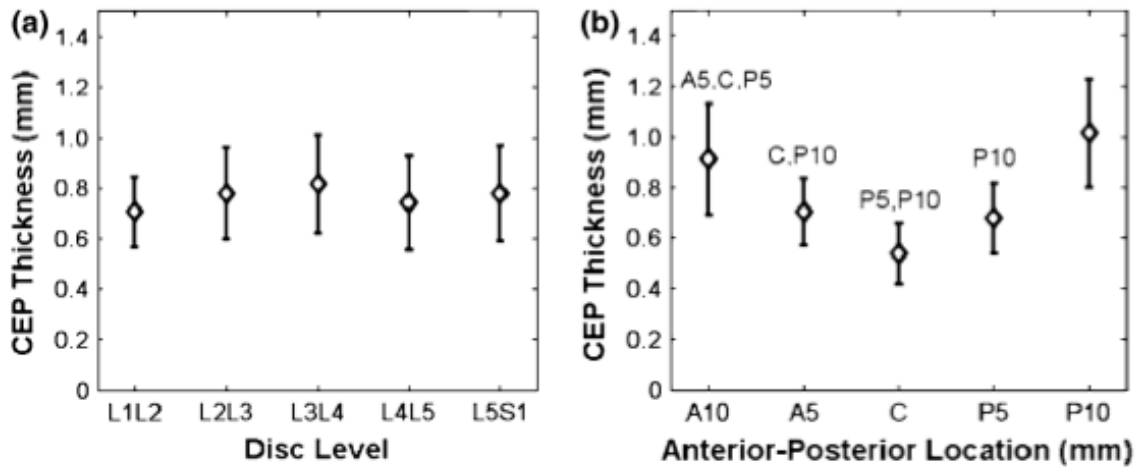


Figure 11: CEP thickness in specimens, as measured on mid-sagittal MRI slices: (a) at different disc levels (b) at different anterior-posterior locations (C-center, A5, and A10 = 5 and 10mm off the center towards anterior, P5, P10 = 5 and 10 mm off the center towards posterior). Letters on top of error bars indicate significance ($p < 0.005$) between measured locations.

3.4. Discussion

This study visualized the CEP morphology in three dimensions and quantified CEP thickness using an MRI 3D FLASH sequence. Optimal sequence parameters were selected by utilizing high-resolution T1 mapping along with an analytical MRI signal model to maximize the signal contrast between the CEP and NP. In addition, histology was performed which confirmed that the MRI FLASH sequence successfully detected the CEP and provided an accurate measurement of CEP thickness. Our MRI FLASH microstructural observations are consistent with recent ultrashort echo time MR imaging of uncalcified and calcified CEP (Bae, Statum et al. 2013), although that study did not measure CEP thickness. The CEP thickness measured in the mid-sagittal plane showed no effect of level, but the CEP becomes thinner toward the center of the disc. This study demonstrates the potential of MRI FLASH imaging for structural quantification of the CEP geometry, which may be developed as a technique to evaluate changes in CEP with disc degeneration in future applications.

T1 mapping and an analytical model of image contrast proved valuable in selecting parameters for FLASH imaging to emphasize the CEP. The high-resolution T1 map showed significant differences in T1 values between the NP and CEP, allowing these structures to be distinguished using appropriate sequence parameters. However, the T1 of the annulus fibrosus was closer to that of the CEP than to that of the NP; thus, careful choice of scan parameters would be needed to distinguish the CEP from the annulus fibrosus. Although only one representative disc was used to obtain the T1 map for the simulations to select the flip angle and TR, the selected optimal parameters resulted in excellent contrast for most of the specimens. The NP–CEP contrast using optimized

parameters from the analytical model would vary as T1 and T2 are expected to vary depending upon the subject's disc health.

The MRI FLASH images using optimized parameters yielded complete and detailed 3D morphology of the CEP, and its axial, sagittal, and coronal views were shown for the first time. The size and shape of the CEP varied considerably among subjects and disc levels. In particular, the circumference of the CEP as seen in the axial sections often had an irregular edge, and this may be an indication of CEP calcification associated with disc degeneration. Additional work is needed to evaluate this, as the histological samples prepared in this study did not contain calcification within the CEP. While preliminary, and of small sample size, the results suggest CEP morphology may be related to disc level and disc health. However, more samples across a large range of degeneration will be required before such correlations can be tested.

The measured CEP thicknesses agree well with previous literature, as does the V-shaped pattern along the anterior-posterior axis of the disc (Figure 11b) (Roberts, Menage et al. 1989). Furthermore, there was no effect of disc level on CEP thickness. Future studies will develop a semi-automated analysis programs that will give measurements with less user input. It is clear that due to both the thinness and curvature of the CEP voxel size should be minimized to avoid artifacts such as Gibbs ringing and partial volume averaging.

In conclusion, this study demonstrated CEP three-dimensional visualization using MRI, showing the three-dimensional CEP morphology and quantifying the CEP thickness in specimens. The CEP thickness was not related to disc level, but the CEP was significantly thicker in the periphery compared with the central location of the disc. This

work thus establishes a methodology for CEP MR imaging. With the relatively short scan time, the technique will provide a new tool for non-invasive assessment and quantification of disc health with potential in-vivo applications.

CHAPTER 4 Annulus Fibrosus Lamellar Structure and Defects

4.1. Introduction

The intervertebral disc substructures consist of a fiber-reinforced annulus fibrosus (AF) that surrounds a central gelatinous nucleus pulposus and cartilaginous endplates (CEP) positioned attachment regionally. The AF is made up of highly organized concentric lamellae that range in thickness from 140 – 520 μm (Marchand and Ahmed 1990) attaching to the vertebrae near the disc periphery while the inner AF merges with the CEP. Adjacent lamellae have alternating fiber orientations above and below the transverse plane (Marchand and Ahmed 1990) and are made up of collagen bundles that are embedded in a matrix of proteoglycans and non-fibrillar collagens.

Intervertebral disc degeneration leads to proteoglycans breakdown, resulting in a pressure loss and the ability to maintain hydration within the NP. The resultant loss of NP pressure causes the AF to bear increased load within the IVD (Tsantrizos, Ito et al. 2005) leading to inward bulging of the AF (Brinckmann and Grootenboer 1991), disorganization, and thickening which increases collagen cross-linking (Pokharna and Phillips 1998). The inner AF undergoes an increase in collagen content, with type II collagen fibrils becoming type I (Weidenbaum and Iatridis 2006) resulting in a less apparent distinction between the NP and AF. These structural changes to the AF can lead to annular tears (Thompson, Pearce et al. 1990, Adams 2004) and ultimately disc herniation linking this change to low back pain (Videman and Nurminen 2004, Peng, Hou et al. 2006).

Annular defects have been categorized into classic tear categories: radial, circumferential, perinuclear (Osti, Vernon-Roberts et al. 1992, Vernon-Roberts, Moore et al. 2007) and other defects: rim lesions and Schmorl's nodes. Radial tears typically initiate at the NP and radiate outward occurring primarily in the posterior AF and are closely associated with NP degeneration and increased age (Osti, Vernon-Roberts et al. 1992, Vernon-Roberts, Fazzalari et al. 1997). Circumferential tears are the separation of lamellae occurring equally in the anterior and posterior AF, often concentrated in the outer regions (Osti, Vernon-Roberts et al. 1992, Vernon-Roberts, Fazzalari et al. 1997). Perinuclear tears are the separation of the NP from the AF resulting in a cleft (Vernon-Roberts, Moore et al. 2007). The literature is replete with cadaveric studies using histology or gross sections depicting AF anatomy and high incidence of AF tears (Osti, Vernon-Roberts et al. 1992, Vernon-Roberts, Fazzalari et al. 1997, Videman and Nurminen 2004, Vernon-Roberts, Moore et al. 2007). However, even multiple histological sections cannot reconstruct these complex 3D geometries. As a result, no accurate quantitative techniques for characterization of the human AF anatomy and defects in 3D exist.

Magnetic resonance imaging (MRI) is a non-invasive, non-ionizing imaging modality well known for its superior soft tissue contrast, making it ideal for disc applications including anatomy, composition, and stage of degeneration through a number techniques (e.g., T1 ρ - and T2-weighted images) (Lyons, Eisenstein et al. 1981, Pfirrmann, Metzdorf et al. 2001, Antoniou, Mwale et al. 2006, Johannessen, Auerbach et al. 2006). Application of MRI to the study of the intervertebral disc has to date focused predominantly on the composition of the NP and AF, not anatomic structure. Few studies

have examined the structure of the AF, therefore the objective of this chapter is to develop MRI techniques to visualize the AF lamellae and quantify its structure defects. To accurately visualize the thin concentric rings of the AF lamellae and quantify the dimensions of defects within the disc a sufficiently high resolution (small voxels) and appropriately matched MRI parameters is required. The imaging techniques developed in this chapter will be applied throughout this thesis to track internal deformations of the intervertebral disc with image registration in-order to measure internal strain.

4.2. Materials and Methods

4.2.1. Intervertebral disc MRI parameter measurement

In this chapter, a T2 weighted 3D TSE (turbo spin-echo) sequence for AF lamellar visualization. Defect visualization with the 3D TSE sequence was verified with the optimized T1 weighted 3D FLASH (fast low-angle shot) MR sequence from Chapter 3 in conjunction with discography. The T2 weighted TSE sequence is characterized by the successive rapid application of 180 rephasing pulses and multiple echoes where repetition time (TR) is sufficiently greater than T1 and T2 less than that of the tissue of interest. Repetition time (TR) is the amount of time between successive pulses applied during image acquisition. T1 relaxation known, as longitudinal relaxation time is a measure of the time required for a tissues protons to realign with the primary magnetic field B_0 . T2 relaxation time known, as transverse relaxation is a measure of time required for a tissues protons to dissipate energy to their surrounding nuclei perpendicular to B_0 . Optimized sequence parameters will yield sufficient image contrast to distinguish each substructure from its adjacent tissue.

Similar to the steps outlined in Chapter 3, MR image sequence optimization involves determining the tissue specific parameters appropriate for the sequence of choice. T1 and T2 relaxation times are measured in milliseconds. T1 and T2 values of NP, CEP, and AF lamellae were measured from a representative (Chapter 3) healthy and degenerate cadaveric lumbar disc (Grade = 2.3/5) (Pfirrmann, Metzdorf et al. 2001) at 7T magnetic field strength. T1 was measured using a fully relaxed (TR = 5100 ms) 2D spin echo inversion recovery pulse sequence with ten inversion times (TI = 33 – 5000 ms). T2

was measured using a 2D spin echo pulse sequence with a TR = 4500 ms and ten echo times (TE = 12 – 60 ms). T1 and T2 maps were generated (Figure 7) by fitting data on a pixel-by-pixel basis to its respective exponential decay function (Equation 4 and Equation 5). Averaging 900 or more pixels within center of the NP, anterior and posterior AF, and CEP determined representative T1 and T2 values of each disc substructure.

$$\text{Equation 4: } I(TI) = I_0 \left(1 - 2e^{-TI/T_1} \right)$$

$$\text{Equation 5: } S(TE) = S_0 e^{-TE/T_2}$$

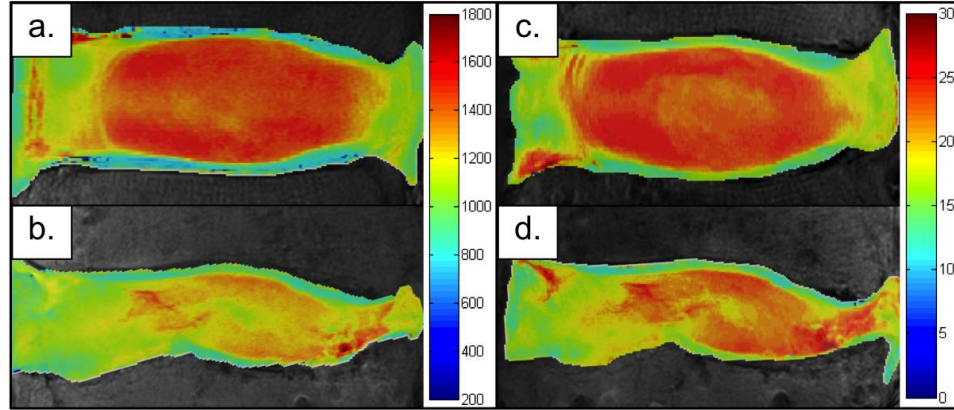


Figure 12: Representative parameter maps at 7T: (A) T1 healthy, (B) T1 degenerate, (C) T2 healthy, and (D) T2 degenerate

4.2.2. Optimization of AF image contrast

An optimized AF inter-lamellar contrast was obtained prior to imaging through utilization of an analytical MRI pulse sequence equation for MRI signal intensity and image contrast. The T2 contrast is dependent upon repetition time (TR) being around 3X that of the annulus's T1 value to reduce the tissues T1 affect and echo times (TE) between the tissues shortest and longest T2 value. Echo time (TE) corresponds to the time between RF pulse and the peak in signal. These parameters are implemented into

Equation 6, where A is the maximum signal amplitude at equilibrium magnetization, TR is the repetition time, TE is the echo time, and T1/T2 are the previously described MR parameters for the discs sub-structures.

$$\text{Equation 6: } MRI_{signal} = A \left(1 - e^{-TR/T1} \right) \left(e^{-TE/T2} \right)$$

Based on the T1 and T2 maps Figure 7, it is apparent that adjacent AF lamellae have different values. These values were measured within each lamella and correspond to approximately ± 2 standard deviations from the mean. To highlight these boundary distinctions the AF MR signal from Equation 6 was plotted vs. TR and TE. Adjacent lamellae were AF signal were defined as $Signal_{AF_max} = \text{mean AF signal} + 2 \text{ standard deviations}$ and $Signal_{AF_min} = \text{mean AF signal} - 2 \text{ standard deviations}$. Inter-lamellar contrast (Δ_{AF}) was defined by was normalization to maximize the signal intensity between alternating AF lamellae (Equation 7).

$$\text{Equation 7: } \Delta_{AF} = \frac{|Signal_{AF_max} - Signal_{AF_min}|}{|1 - Signal_{AF_max}|}$$

4.2.3. Annulus Fibrosus Imaging

Specimens for AF imaging were prepared from 8 cadaveric human lumbar spines (n=10 discs, age: 61.5 ± 11.1). While for some subjects 2–3 levels were used from a single spine, consistent with common practice in the literature (O'Connell, Vresilovic et al. , Iatridis, Setton et al. 1997, Rodriguez, Slichter et al. 2011), these discs were assumed to be independent samples. Each whole spine was first scanned with a mid-sagittal T2-weighted turbo spin echo imaging sequence for routine grading of degenerative state (Pfirrmann, Metzdorf et al. 2001, Johannessen, Auerbach et al. 2006). The integer grade from five individual examiners was averaged (Grade: 3.1 ± 0.7). Lumbar spines were

then dissected into bone-disc-bone segments with posterior elements removed and sealed in airtight freezer bags to avoid dehydration during imaging. The sealed segments were then embedded in 2 % agarose gel for immobilization and to reduce image distortion at tissue edges due to the tissue/air mismatch in magnetic susceptibility (Schenck 1996).

For protocol optimization, the TR and TE that yielded the best inter-lamellar contrast between adjacent annulus lamellae were selected using the analytical model simulation. All imaging was done in a Siemens Magnetom 7T scanner (Siemens Medical Solutions, Erlangen, Germany) using a 4-channel ankle coil (Insight MRI) (Wright, Lemdiasov et al. 2011). Due to scan time constraints, a voxel size of $300 \mu\text{m}^3$ was chosen. Imaging parameters were TR = 3000, TE = 34, $(0.3 \text{ mm})^3$ isotropic resolution, matrix = 256 x 256, fat suppression. Scan time was 2.75 hours per disc.

4.2.4. Annular tear detection

Defects within the annulus structure will be visualized from the optimized 3D TSE sequence. These AF lamellae disruptions will be co-registered with the optimized 3D FLASH sequence from Chapter 3 to verify they are not imaging artifacts. Through injection of radiographic dye into the nucleus pulposus under fluoroscopic guidance radial tears seen under MRI will be matched to fluoroscopic images. Tears will be categorized as radial, circumferential, perinuclear or a combination of these.

OsiriX image analysis software was used to measure total disc volume (cm^3), tear volume (mm^3), disc perimeter length (cm), and tear path length (mm). Measurements were made by segmenting regions of interest (ROI) for the entire disc and tear in each slice throughout the entire image set (Equation 8). Disc perimeter was measured along the mid-axial disc height by tracing its outer kidney bean shaped circumference (cm).

Tear path length (mm) was measured by tracking the propagated length of the tear throughout the disc.

$$\text{Equation 8: } \sum (ROI_{area}) \times (Thickness_{slice}) = ROI_{volume}$$

4.3. Results

4.3.1. Annulus Fibrosus Lamellar Visualization

A T1 and T2 map (Figure 7) and the average values (\pm standard deviation) of each disc substructure obtained at 7T are presented for a representative healthy and degenerate disc substructures in Table 1.

Grade	Region	T1	T2
Healthy	AF	1270 ± 80	21 ± 1.4
	NP	1510 ± 50	25 ± 1.1
	CEP	775 ± 75	14 ± 0.8
Degenerate	AF	1100 ± 43	19 ± 1.6
	NP	1300 ± 65	21 ± 1.4
	CEP	840 ± 32	13 ± 1.0

Table 2: Average T1 and T2 values for a healthy and degenerate disc substructures.

These T1 and T2 values were used in Equation 6 and Equation 7 to calculate signal intensity and determine optimal pulse sequence parameters for interlamellar annulus fibrosus image contrast (D_{AF}) (Figure 13). Figure 13a shows a contour plot of D_{AF} covering the exhaustive range of TE (0–120 MS) and TR values (0–6,000 ms). The average annulus fibrosus T2 value was $1,185 \pm 62$ ms, to ensure a T2 weighted image a TR value of $\geq 4,000$ ms would be ideal and achieve optimal image contrast (asterisk Figure 13). However, to maintain reasonable imaging times (< 3 hours) during acquisition of axial loaded discs 3,000 ms was selected and corresponding TE of 34 ms (dotted line, Figure 13b).

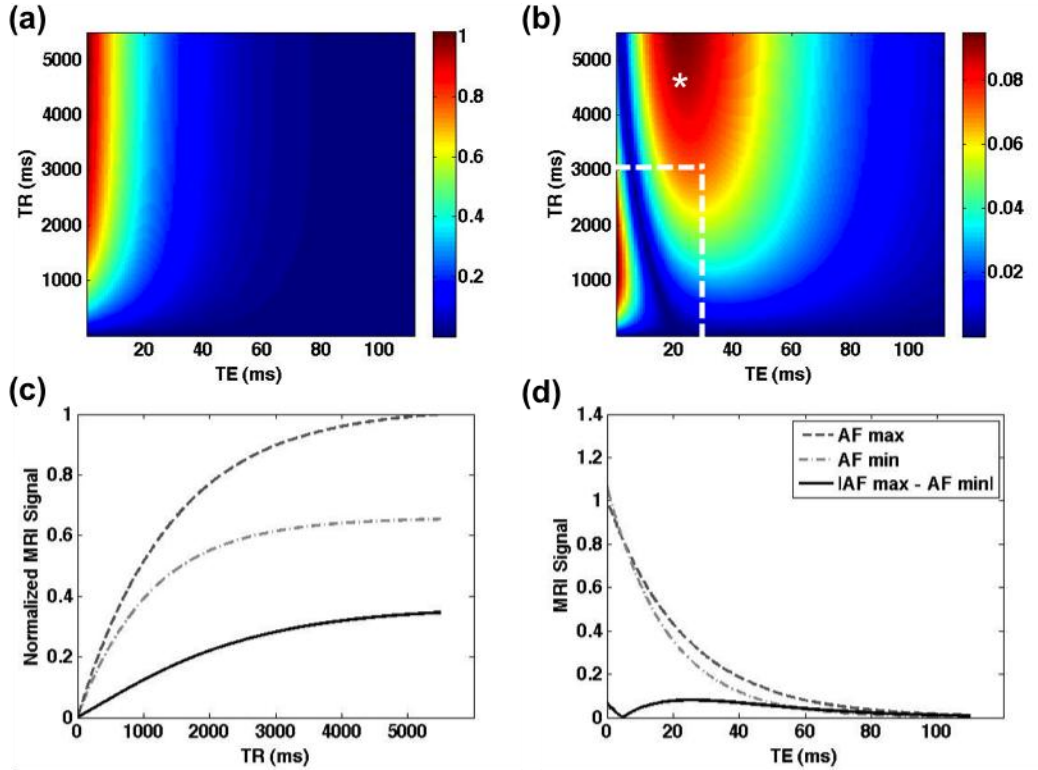


Figure 13: Computed AF MRI signals and image contrast at 7T. (a) Normalized AF signal intensity according to Equation 6 over the full range of parameters TR and TE. (b) AF image contrast based on Equation 7 utilizing the maximum and minimum AF signal intensities. (c,d) Computed AF max (dashed), AF min (dotted) MRI signals, and image contrast (solid) at optimal TE (34 ms) (c) and versus TE at optimal TR (3000 ms) (d).

The small 13% change in annulus fibrosus T2 relaxation time with degeneration did not alter the effective patterns seen in Figure 13. Increased degeneration resulted in lower overall signal intensity and achieved maximal contrast at TR values $\geq 3,500$ ms and an optimal TE range from 20 – 40 ms.

4.3.2. Annulus Fibrosus Tear Detection

Tears were present in all lumbar discs evaluated, however the sample size was small (n=10) and primarily comprised of degenerate discs (average grade = 3.1). A representative defect image for a radial, perinuclear, and circumferential tear are shown

in (Figure 14). Note, however, that even for these “classic” categories, the radial tear has additional tear offshoots in the perinuclear and circumferential orientations (Figure 14a) and perinuclear tear NP clefting extended outwards into radial tears (Figure 15c). A total of 4 radial, 4 circumferential and 2 perinuclear tears were visualized and quantified, geometry of these and other defects are provided in Table 3.

Specimen Data					Volume		Length (cm)		Location
Fig Ref	Type	Age/Gender	Level	Pfirr.	Disc (cm ³)	Tear (mm ³)	Disc Perimeter	Path Length	
2A	R, C	66/F	L1L2	4	10.82	15.00	13.63	1.62	L
1A	R	53/F	L2L3	3	16.22	18.90	13.85	5.65	L
NA	R	78/F	L4L5	4	18.47	0.33	15.15	0.41	AL
2D/E	C	63/M	L2L3	3	20.61	12.90	16.49	2.06	TL
NA	C	42/F	L1L2	2	11.48	0.92	12.54	0.28	A
1C	C, R	70/M	L4L5	3	25.30	14.10	16.57	0.79	PL
2C	PN, R	63/M	L3L4	3	14.96	193.50	16.48	8.25	TL
1B	PN, R	63/M	L4L5	4	13.90	58.90	16.48	5.84	TL
NA	C	47/F	L1L2	3	11.61	15.22	13.53	0.08	L
NA	R	63/M	L2L3	2	14.04	16.77	14.34	1.59	PL

Table 3: Tear severity measurements. Type: R = radial, C = circumferential, PN = perinuclear. Location: L = lateral, TL = trans-lateral, A = anterior, AL = antero-lateral, PL = postero-lateral.

The tears had varying ranges in volume and path length, respectively as: radial 0.33 – 16.77 cm³ and 0.41 – 1.62 cm, circumferential: 0.92 – 15.22 cm³ and 0.08 – 2.06 cm, perinuclear: 58.90 – 193.5 cm³ and 5.84 – 8.25 cm.

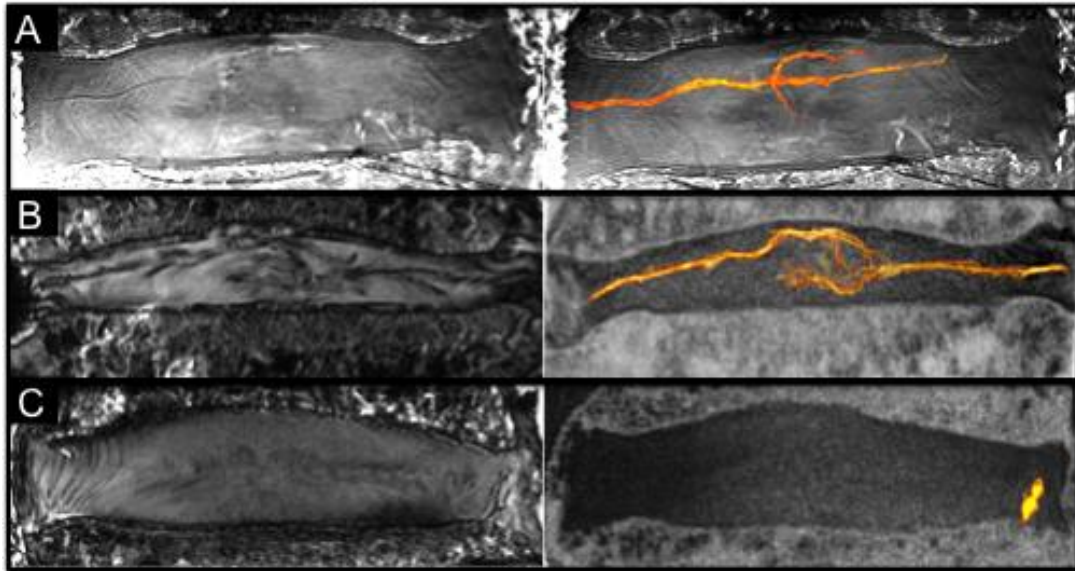


Figure 14: Representative images for (A) Radial, (B) Perinuclear, and (C) Circumferential tears. Left column shows raw TSE images and right shows 3D fusion volume rendering for each tear, respectively

The majority of tears present within this study were located in the lateral regions of the disc, with only 2 discs of 10 having a tear present in the postero-lateral region. The presence of Schmorl's nodes and rim lesions were observed in two specimens, however dimensions were not quantified here. Imaging the same disc with three techniques indicated tear presence; injection of radiographic dye under fluoroscopic guidance, T2 weighted MR image, and FLASH imaging (Figure 16) all depicted the same tear. Further histological and gross sectioning analysis is required to accurately validate the presence of tears within discs.

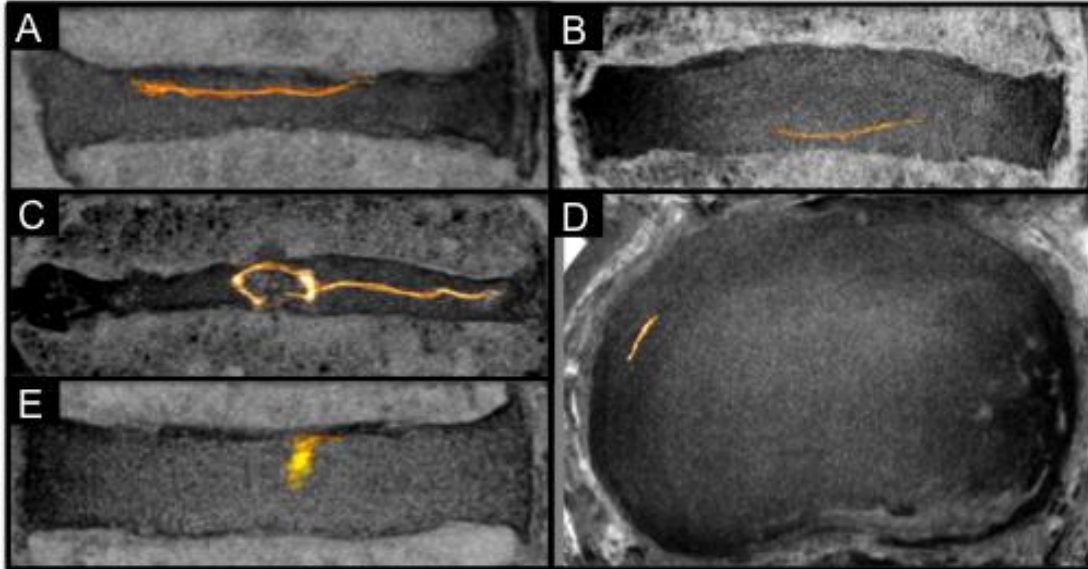


Figure 15: Volume renderings of tears: (A-B) Radial and (C) Perinuclear/Radial – coronal views; (D-E) Circumferential – axial and coronal views of the same specimen.

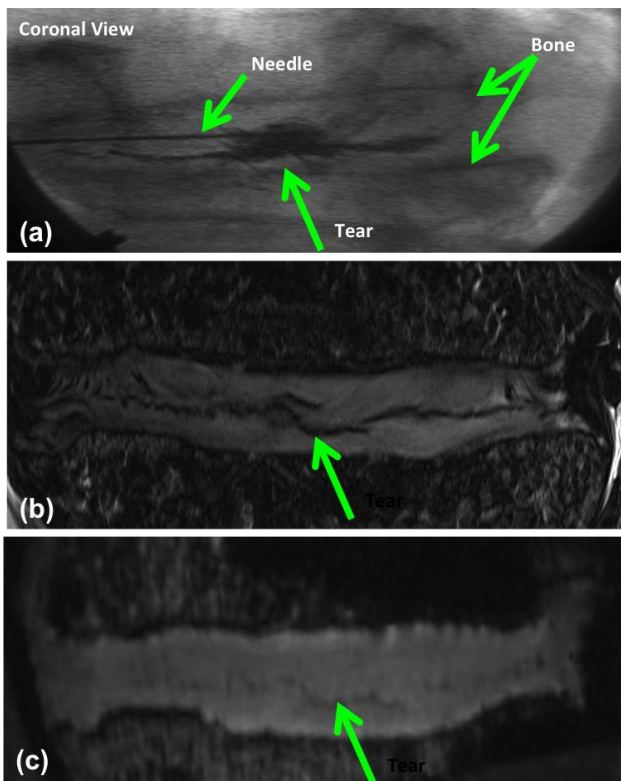


Figure 16: Three matched images of a radial tear with different imaging: (a) fluoroscopic coronal view with radiographic dye, (b) T2 weighted TSE, and (c) T1 weighted FLASH

4.4. Discussion

The annulus fibrosus morphology was visualized in three dimensions with a MRI 3D T2-weighted TSE sequence. High-resolution T1 and T2 mapping with an analytical MRI signal model enabled sequence parameter optimization to maximize signal contrast between adjacent AF lamellae. Clear AF lamellar distinction will enable the ability to internal displacements under axial compression with image registration in Chapter 6-8. This study will enable future studies to non-invasively assess the effects of degeneration AF lamellar structure, shape and orientation in three dimensions.

Quantitative mapping of the discs substructures provided valuable data in sequence selection and parameter optimization to visualize the structure of choice. Although only one representative disc was used to obtain T1 and T2 maps, the selected optimal parameters yielded excellent inter-lamellar contrast for all specimens. This strong contrast enabled the ability to visualize and quantify defects within the disc. Improved image resolution and scan time will permit future analysis of strain patterns around such defects.

Until now non-invasive detection of disc defects has been limited and detailed quantification of their characteristics was not possible without disturbing the native boundary conditions of the tissue. To date, tears have primarily been quantified by performing histological sections, which can lead to artifacts during sectioning and lack the ability to accurately portray and quantify tear complex and unique geometry. This method provides a non-invasive technique for 3D visualization, measurement, and the ability to precisely locate defect orientation within a disc.

The current clinical understanding of tears is that those radiating to the outer third of the AF may cause low back pain (Bogduk 1991). However, in-vivo detection of tears is difficult and quantification of their characteristics is not possible. High-intensity zones (HIZ) seen on clinical T2-weighted MRI are thought to be tears radiating outwards from the NP (Schizas, Kulik et al. , Peng, Hou et al. 2006, Gallucci, Anselmi et al. 2011, Wang and Hu 2012), however it is controversial whether these represent actual tears. Radial tears can be visualized under discography, however their location and orientation is difficult to determine (Bernard 1990). Additionally this is an invasive procedure and involves exposure to radiation. The MR imaging technique presented here suggests that MRI might provide an improvement from these procedures.

This method is currently far from in-vivo implementation due to the long imaging time. Future work will focus on further quantification and more samples that better represent the population. This will allow for implementation of accurate tear positioning and location placement into finite element models to determine the functional implications of AF tears. The ability to see structure without disrupting the native boundary conditions of the intervertebral disc will lead to better understanding of degenerative changes.

CHAPTER 5 **Design of a MRI Loading Device**

5.1. **Design Objectives**

The objectives of this chapter are to develop methods for applying axial compression and torsion to the intervertebral disc. The design objectives for this device are:

1. MRI safe, made up of non-magnetic materials, and not cause interference artifact with the chosen RF coil
2. Integrate with a curved 4-channel RF coil array and fit within the bore (60 cm) of a Siemens Magnetom 7T MRI
3. Not alter the optimized [Chapter 4] imaging parameters: turbo-spin echo sequence (TR/TE = 3000/34 ms, matrix = 256 x 256, 0.3 mm² resolution, fat suppression)
4. Interface with an Instron 8874 enabling free range of motion along the primary axis of the spine
5. Remove applied load from the Instron while maintaining fixed displacement during image acquisition
6. Maintain hydration during mechanical testing and image acquisition

5.2. Design and Fabrication

Material selection was based on minimizing magnetic susceptibility; the entire loading frame was made of either polyvinyl chloride plastic (PVC) or Delrin and secured with nylon screws. Similar nonmagnetic loading frames have been used in literature within a 3T MR (Chiu, Newitt et al. 2001, O'Connell, Johannessen et al. 2007, Reiter, Fathallah et al. 2012, Chan and Neu 2013) to perform in MRI loading, however only 2D strains were reported. A rectangular loading frame was designed to interface with an Instron 8874 (Figure 17) by bolts that attach to the Instron's base plate, which positions the motion segment to undergo axial compression.

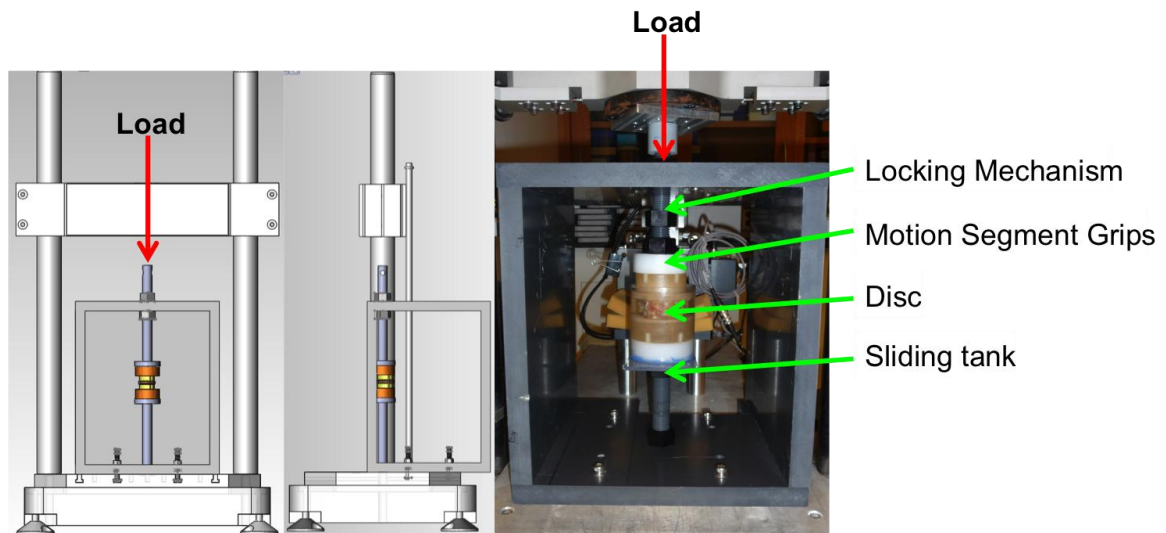


Figure 17: MRI loading frame integration with Instron 8874

Cylindrical PVC loading platens (Figure 17) and a custom mold for potting motion segments in polymethyl methacrylate (PMMA) were secured to the frame by threaded rods. These rods function to adjust motion segment position, aligning the disc's center with the RF coil's center to ensure maximum signal to noise ratio (SNR). One-rod screws

into the base, secured by a locking nut, while the opposing goes through the opposite frame wall, permitting axial compressive or torsional motion. Compression is secured by a series of locking bolts (Figure 17) placed on either side of the frame that, when tightened, remove load from the Instron and lock in the applied displacement. The application of torsion was designed but not fabricated for this thesis. A locking pin secures the driving rod to the Instron to enable torsional loading in a clock-wise direction, so as to not loosen any threaded connection. Torsion is secured through two steps; first tightening the locking bolts and then sliding a locking pin through aligned pre-drilled holes positioned between the locking bolts and loading frame. Once displacement is locked into place, all forces are transferred to the loading frame, which enables removal from the Instron. Hydration was maintained throughout experimentation by use of a sliding cylindrical tank (Figure 17). During mechanical testing, a lock nut keeps the tank flush to the motion segment grips to prevent phosphate buffered saline (PBS) leakage. Prior to image acquisition, the lock nut is loosened to drain PBS and then re-tightened to fill the tank with 2% agarose. The tank subsequently slides out of the way for image acquisition in order for the receive array of the RF coil to fit snugly over the disc + agarose.

The disc was positioned so that the lateral side faced the top surface of the MRI bore and the disc axis was parallel with the MRI bore (Figure 18). The lateral positioning enabled axis of symmetry to be applied for strain measurements, accounting for the horseshoe shaped receive array of the RF coil (Figure 18).

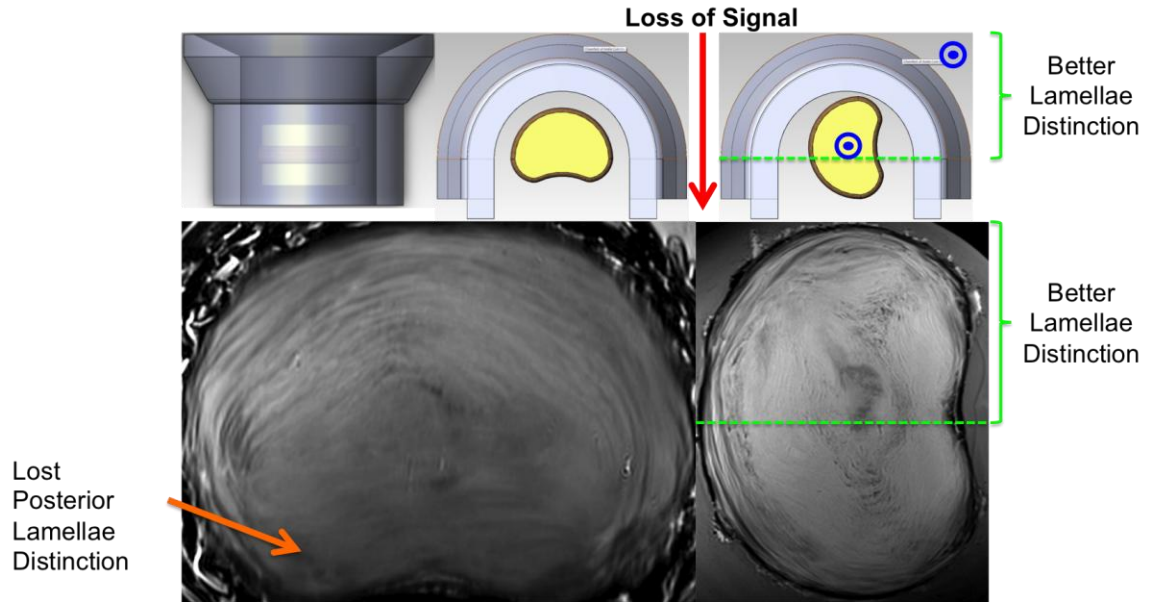


Figure 18: Effect of signal to noise ratio (SNR) on disc positioning within the MRI. Red arrow indicates the direction of lost signal within the RF coil. Clinically relevant anatomic orientation (Left Side) results in decreased posterior AF lamellar distinction (Orange Arrow). Lateral positioning of the disc (Right Side) enables the spine axis and B_0 (Blue Circle: dot indicates spine axis and B_0 direction) to be parallel, decreasing banding artifacts within the disc during image acquisition.

The spine axis was oriented parallel to the MRI bore (B_0 – direction of primary magnetic field), as done during clinical diagnostic MR imaging (Takashima, Takebayashi et al. , Pfirrmann, Metzdorf et al. 2001, Johannessen, Auerbach et al. 2006, Lotz, Haughton et al. 2012) and due to coil and mechanical loading constraints (Figure 19). Additionally, banding artifacts occur around the periphery of the disc when the spine axis is not parallel to B_0 (Saifuddin, Blease et al. 2003, Alyas, Connell et al. 2008). Once applied loading is removed from the Instron, PBS is replaced with agarose, and tank slides out of the way. The loading frame is positioned around of the transmit piece of the RF coil and the receive array is positioned directly over the disc (Figure 19). Slots were machined in the sides of the loading frame to permit RF coil cables to properly interface with the MRI (Figure 19).

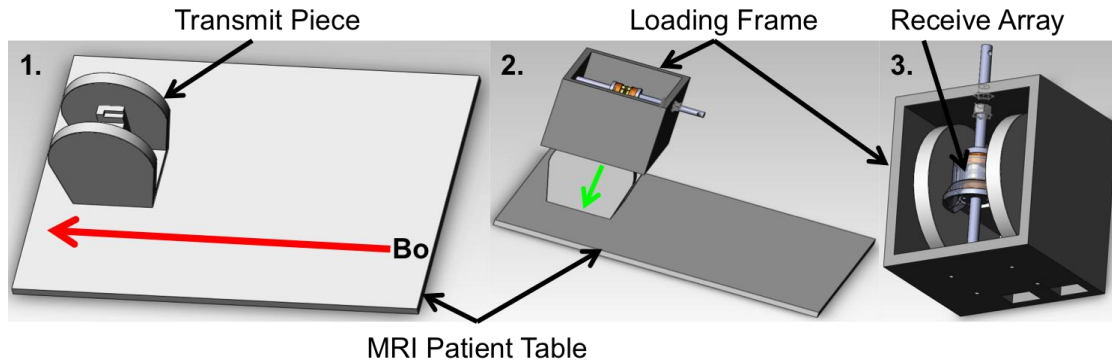


Figure 19: Integration of loading device with MRI and RF coil: (1) Placement of the transmit piece of the coil in the direction of B_0 on the MRI patient table, (2) loading frame slides over the transmit piece, and the (3) receive array slides directly over the disc's location.

The curved RF coil (Wright, Lemdiasov et al. 2011) was originally designed for study of trabecular bone within the distal tibia, and hence, required the transmit coil to be loaded with enough signal to fine tune shimming of the magnet. To supply enough signal for adequate loading of the transmit coil, bottles of 1X PBS were placed along the transmit coil base, positioned below the disc and receive array.

5.2.1. Design Effectiveness

Design effectiveness was tested with two main criteria: the effect of loading frame + RF coil integration on signal to noise ratio during image acquisition and repeatability of successful axial strain application. These two tests will confirm achievement of all design objectives and ensure functionality for planned experiments in [Chapter 7-8]. Two degenerative grade 3 (Pfirrmann, Metzdorf et al. 2001) lumbar L4L5 motion segments were selected to undergo image acquisition with [Figure 20A] and without [Figure 20B] the loading frame.

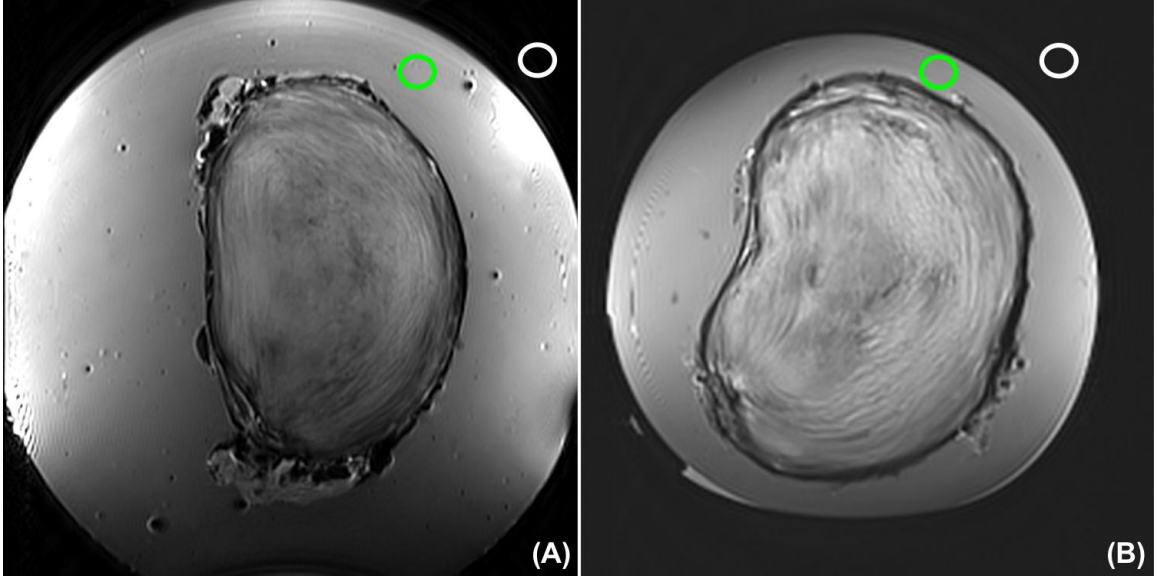


Figure 20: Representative mid-axial MR images with (A) and without (B) loading frame. Signal to noise ratio (SNR) was measured using a region selected within the agarose (Green) to represent signal, as these samples come from different lumbar levels (Noise – White).

The sample with frame and sample without frame (embedded in 2% agarose within a plastic specimen cup) were scanned separately within the 7T MR scanner and integrated with a 4-channel RF coil. Utilizing optimum imaging parameters developed in [Chapter 4], high-resolution 3D 300 μm isotropic MR images were acquired with a T2-weighted turbo-spin echo sequence (TR/TE = 3000/34 ms, matrix = 256 x 256, fat suppression).

$$\text{Equation 9: } SNR = \frac{P_{\text{signal}}}{P_{\text{noise}}}$$

Signal to noise ratio (SNR) was measured [Equation 9] in each image along the mid-axial disc height. The signal to noise ratio is a measure of the signal intensity within the region of interest divided by the signal intensity of the image background. Average signal (P_{signal}) pixel intensity corresponds to the green circular region and average noise (P_{noise}) pixel intensity corresponds to the white circular region [Figure 20]. The change SNR for

each image set and AF lamellar visibility were assessed to determine any interaction effects of the loading frame with RF coil.

A small sample size ($n=3$) of L4L5 lumbar motion segments underwent axial compression to test the loading frames ability to consistently apply and maintain axial compression. Thawed and hydrated bone-disc-bone segments with posterior elements removed were potted in polymethyl methacrylate bone cement. Mechanical loading followed by image acquisition was performed under two conditions: reference (50N preload) and 5% applied grip-grip compressive strain. The sample was placed in a PBS bath within the loading frame and installed in the Instron, which was used for load application. For the reference condition, a 50N pre-load was applied to ensure contact of the loading fixtures and held for 20 min. Locking bolts were then tightened to secure the position. The sample + frame was removed from the Instron. PBS was removed and replaced with agarose and then placed within in the 7T MR scanner and a 4-channel RF coil [Figure 19] for high-resolution MR images using the optimized image parameters.

After image acquisition the agarose was replaced with PBS and the sample + frame was returned to the Instron. The Instron crosshead was returned to the pre-load position and the locking bolts were then loosened. The average disc height was calculated by dividing the mid-sagittal/coronal disc space area by the anterior-posterior/lateral width from the pre-loaded reference image [Figure 21]. A 5% grip-grip compressive strain, based on mid-sagittal/coronal disc height, was applied at a slow rate of 0.1 mm/s (Holmes, Hukins et al. 1993) and held for 2.5 hours of relaxation within the Instron. The position was again locked, PBS replaced with agarose, and the sample + frame returned

to the MR scanner for imaging at the loaded condition using the same imaging parameters.

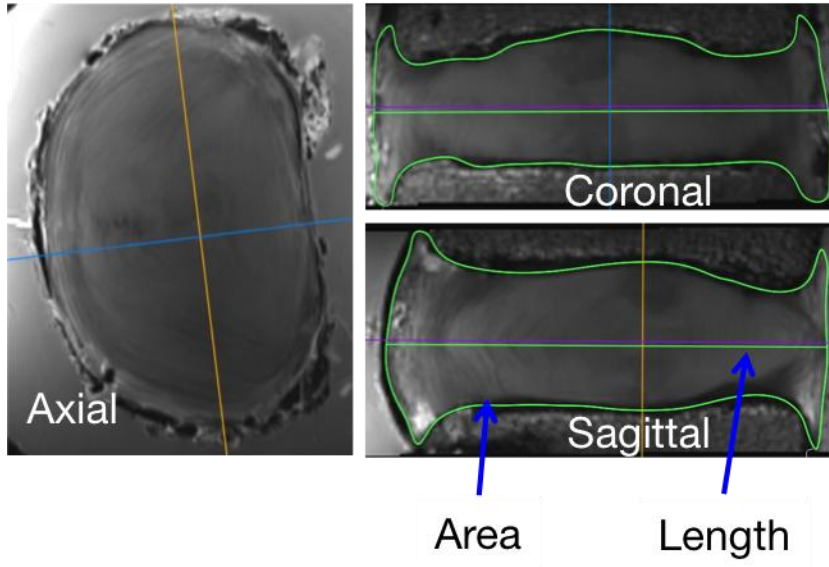


Figure 21: Representative image depicting area and length measurements in the Coronal and Sagittal plane to determine an average disc-height across the entire disc volume.

Achieved axial compression was determined by measuring disc-height from the loading image set and calculating global disc strain [

Equation 10]. Average achieved axial compression was reported.

$$\text{Equation 10: } E_{zz} = \left(\frac{(PreLoad_{DiscHeight} - Loaded_{DiscHeight})}{PreLoad_{DiscHeight}} \right) * 100$$

5.3. Results and Discussion

The loading frame successfully achieved all design objectives by integrating with an Instron, MRI, and curved RF coil. Loading frame incorporation resulted in a 50% SNR decrease when compared to imaging without the loading frame (

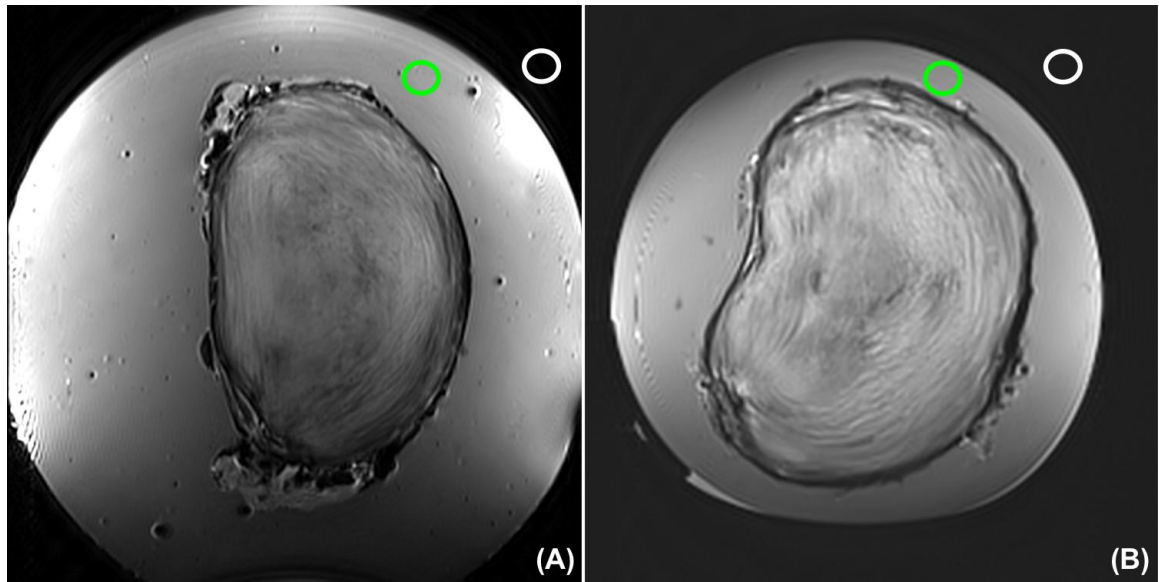


Figure 20). However, this apparent decrease in SNR still left a 20:1 ratio and strong lamellar contrast. Additionally, the loading frame was able to maintain disc hydration and hold an applied displacement throughout experimentation. The applied 5% axial strain, which was calculated from initial MRI mid-sagittal/coronal disc height measurements, achieved a successful average E_{zz} of $-4.88 \pm 0.33\%$. The tight integration of the loading frame with MRI and RF coil enabled reliable positioning of the disc between scans, minimizing rigid body motion between image sets. The developed loading frame will be utilized in [Chapter 7-8] to apply incremental amounts of axial compression.

CHAPTER 6 **Optimization of ANTs Image Registration Parameters – in 2D images and comparison to Vic2D**

6.1. **Introduction**

Various non-invasive techniques have recently utilized magnetic resonance imaging (MRI) to enable 2D internal deformation measurements of the intervertebral disc (IVD) (O'Connell, Malhotra et al. , O'Connell, Vresilovic et al. , O'Connell, Johannessen et al. 2007, Reiter, Fathallah et al. 2012, Chan and Neu 2013). Chan and Neu applied displacement encoded MRI, an image tagging method that enables direct displacement measurements from MR data reporting strain across the entire IVD. This technique validated strain measurements through applied deformations to a non-biological phantom. O'Connell *et al.* utilized texture correlation to measure regional AF strain under axial compression. Thus, our laboratory was able to report the effect of loading position, degeneration, and nucleotomy. Strain could only be calculated in small rectangular areas of interest with Vic2D, missing regions at the bone–disc interface. Reiter *et al.* employed image registration, enabling a continuous map of the transformation between images. However, registration quality was verified with an artificial image that was not representative of the disc. In order to accurately assess an internal deformation measurement technique, it is important to verify deformations with the specific tissue of interest, ensuring boundary condition replication and native tissue movement.

This chapter will establish Advanced Normalization Tools (ANTs), an image registration software that creates a continuous map of the transformation between images

as a non-invasive technique to measure internal IVD strain. The implementation of manual segmentation tools will enable registration accuracy verification and strain measurements across any user-defined regions. This approach will be applied to data from O'Connell *et al.*, where the effect of nucleotomy was assessed on internal IVD strains. Nucleotomy is the removal of NP material through an AF incision to mimic the clinical procedure of discectomy. Discectomies are performed on a herniated (expulsion of nucleus pulposus through a tear in the annulus fibrosus) IVD to remove NP fragments. The removal of NP material and AF incision has been shown to accelerate disc degeneration (Hanley and Shapiro 1989, Brinckmann and Grootenboer 1991, Kambin, Cohen et al. 1995, Yorimitsu, Chiba et al. 2001, Weinstein, Lurie et al. 2006, McGirt, Eustacchio et al. 2009, Mariconda, Galasso et al. 2010) and alter native mechanics (Seroussi, Krag et al. 1989, Broc, Crawford et al. 1997, Frei, Oxland et al. 2001, Meakin, Redpath et al. 2001, Kuroki, Goel et al. 2004, Johannessen, Cloyd et al. 2006, Vresilovic, Johannessen et al. 2006, Cannella, Arthur et al. 2008, Heuer, Schmidt et al. 2008). Therefore, the objectives of this chapter were to optimize ANTs parameters for disc image registration, verify registration accuracy, and compare registration strain measurements before and after nucleotomy with Vic2D method of analysis (O'Connell, Vresilovic et al.).

6.2. Materials and Methods

6.2.1. Mechanical Testing and Image Acquisition

A sample set of $n=5$ (grade 1-3) from the work of O'Connell *et al.* (2007) was selected at random for 2D strain validation. Sample preparation and MR image acquisition is previously described in detail (O'Connell, Malhotra *et al.* , O'Connell, Vresilovic *et al.* , O'Connell, Johannessen *et al.* 2007). Intact fresh-frozen human lumbar motion segments were embedded in fixtures with polymethyl methacrylate (PMMA) bone cement. Each sample was placed in a custom-built, non-magnetic loading device and underwent axial compression inside a 3T MR scanner. Two mid-sagittal images were acquired using a high-resolution T_2 -weighted TSE sequence and a custom-built coil (resolution = $0.234 \times 0.234 \times 3\text{mm}$). The IVD reference image was captured under a 20N pre-load. The deformed image was taken after 1000N was applied and 20 minutes of creep deformation was completed.

6.2.2. Anatomic feature labeling

Key anatomic features (AF lamellae, IVD defects, EP-NP border, and EP-VB border) that could be discerned in both images were manually labeled using segmentation software ITK-SNAP (Figure 22) (Yushkevich, Piven *et al.* 2006).

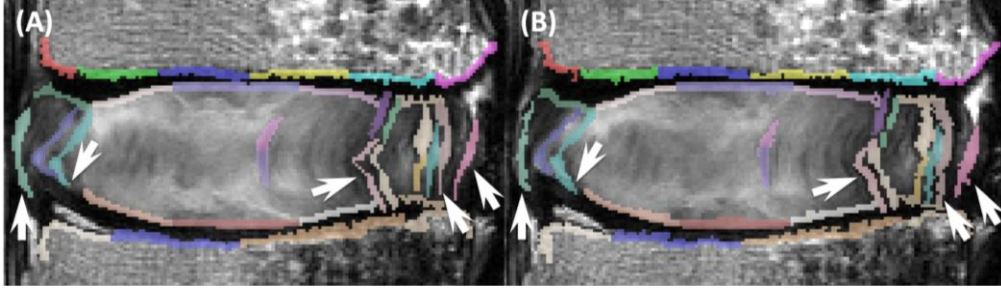


Figure 22: Representative (A) reference and (B) deformed labeled images. Labels cover the SVB, IVB, AF lamellae, and defects. Arrows indicate differences between reference and deformed images.

Each set of labels was utilized throughout parameter optimization to assess registration quality. Applying the inverse warp field found in registration to the deformed image labels generates a reconstruction of the original reference labels. Overlaying the reconstructed labels on the reference (Figure 23) determined segmentation accuracy and registration quality with overlap statistics.

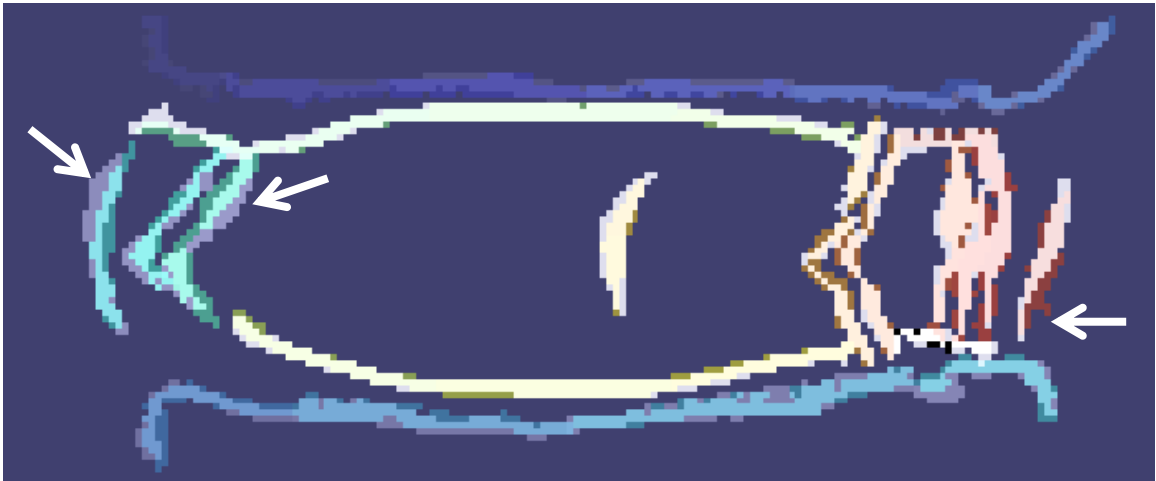


Figure 23: Overlay of reference and reconstructed labels. Arrows indicate regions where individual pixels are not aligned.

Labels were iteratively checked both visually and with an overlap statistic. Visual inspection compared reconstructed with reference label features by overlying labels on their respective image. The overlap statistic used, Hausdorff, (Equation 11) is an

indication of the maximal degree of mismatch between two labels. It is calculated as the maximal distance in all pixels of the reference label to the nearest point in the warped image.

$$\text{Equation 11: } h(A, B) = \max_{a \in A} \min_{b \in B} \|a - b\|$$

Lower case ‘a’ and ‘b’ are individual points within images ‘A’ and ‘B’ respectively.

Hausdorff was evaluated after registrations to confirm correct labeling; labels with a Hausdorff greater than 4 pixels were reviewed and updated. Image quality dictated the number of paired labels for each image set (26 to 37 label pairs); only features that can be clearly seen in both images were labeled.

An ideal registration would produce Hausdorff and Average Housdorff equal to zero and a target overlap of 100%. Average Hausdorff (Equation 12) is the average of all pixel distances between both labels representing the mean degree of mismatch between two labels.

$$\text{Equation 12: } h_{avg}(A, B) = \frac{1}{|A|} \sum_{a \in A} \min_{b \in B} \|a - b\|$$

Target overlap (Equation 13) is the ratio of the area contained in both the reference and warped image labels over the area of the reference image label.

$$\text{Equation 13: } TO = \left(\frac{|Reference \cap Reconstructed|}{|Reference|} \right) 100$$

6.2.3. Optimization of Image Registration Parameters

Advanced Normalization Tools (ANTs) provides numerous parameter options that guide the resultant warp field from two (reference \rightarrow deformed) registered images (Table 4).

Category	Transformation Model	Similarity Metric	Regularization Technique
Linear	Rigid	MI, MSQ	
	Affine		
Elastic	Deformable	CC, PR, MI, MSQ, PSE	Gaussian, DMFFD
	DMFFD		
Diffeomorphic	Exponential	CC, PR, MI, MSQ, PSE	Gaussian, DMFFD
	Greedy SyN		
	Geodesic SyN		

Table 4: Matrix of ANTs registration parameters (transformation models, similarity metrics, and regularization techniques). MI = mutual information, MSQ = mean squared difference, CC = fast cross correlation, PR = cross correlation, PSE = point set expectation, DMFFD = directly manipulated free form deformation. Adapted from Avants *et al.* 2011

Rigid body motion was accounted for with an initial affine registration. A mean-squared difference (MSQ) similarity metric was employed, which is ideal for mono-modality (MRI only) registrations (Equation 14).

$$\text{Equation 14: } MSQ = \sum_{i=1}^N (I_i - J_i)^2$$

Quantifying the degree of mismatch for image intensities can be problematic during registration for outlier intensity values due to the squared term in Equation 14. This is accounted for by defining an outlier term (X) when an intensity value in the reference image (I) and the intensity value of corresponding pixel in the deformed image (J) is greater than X. In this scenario, the MSQ equation is treated linearly. A directly manipulated free-form deformation (B-spline) regularization technique was chosen over Gaussian to control the amount of data smoothing within the registration processes. This technique has been widely used in medical imaging to measure soft-tissue deformations

with MR images (Tustison, Cook et al. , Tustison, Davila-Roman et al. 2003, Tustison, Avants et al. 2009) utilizing cubic B-splines. Preliminary work showed that a Gaussian regularization technique creates swirling artifacts within the registration (Figure 24).



Figure 24: Reconstructed image displaying the effect of Gaussian (A) vs. B-spline (B) regularization technique. Note the unnatural swirling pattern within the NP and vertebrae in the Gaussian regularization.

Parameter optimization was executed by varying transformation model (Elastic vs. Diffeomorphic), adjusting outlier value (X) within a MSQ similarity metric form 0.001 or 0.1, and numbering the splines used (7 even increments from: 2x2 – 14x14) with a DMFFD regularization technique (Parameter Overview: Table 5). The value range for outliers was based on preliminary experiments that indicated strain values remained constant when less than 0.01 and decreased when greater than 0.1. Additionally, the spline range was limited to values up to 14x14 since larger ranges resulted in a decreased label Target Overlap and an increased Hausdorff and Average Hausdorff.

Variable	Parameters					Comments
Transformation Model	Elastic vs. Diffeomorphic					Small vs. Large deformation freedom
Similarity Metric	MSQ	Radius	2			Defines pixel search radius
		Outlier	0.001	0.01	0.1	Accounts for large pixel intensity variation
Regularization Technique	DMFFD	2x2 → 30x30				Controls data smoothing

Table 5: Parametric analysis variable matrix used for registrations

Labels were grouped into anatomic regions: vertebral body (VB), annulus fibrosus (AF) and nucleus pulposus (NP). A global overlap statistic was reported for each region by taking the mean across all registered images. The overlap statistics were pooled for all number of splines because values remained constant for greater than 6x6.

Transformation model versus outlier value was assessed by a series of nine two-way ANOVAs with replication for each region (VB, AF, and NP) and overlap statistic (Target Overlap, Hausdorff, and Average Hausdorff). Four post-hoc paired, two-tail t-tests ($p \leq 0.05$) determined significance between outlier values within and between a transformation model (i.e., Diffeomorphic/Elastic 0.001/0.01 vs. Diffeomorphic/Elastic 0.001/0.01 and Diffeomorphic 0.001/0.01 vs. Elastic 0.001/0.01).

Based on preliminary analysis, there was no significant difference between strain values using a Diffeomorphic or Elastic transformation models. Elastic was selected because it is ideal for small deformations. The optimal outlier value was set to 0.01 based on the best overlap statistics; target overlap (68.48%) was maximized while minimizing Hausdorff (2.25 pixels) and Average Hausdorff (0.39 pixels). The number of splines used in regularization was determined by measuring the effect of spline number on the mean and the standard deviation of strain within the superior (SVB – top of image) and inferior (IVB – bottom of image) vertebral bodies and the entire annulus fibrosus (AF).

Anticipated results include nearly zero strain within the vertebral bodies, approximately 7% axial strain (O'Connell, Malhotra et al.), maximal target overlap, and minimal Hausdorff and Average Hausdorff. Radial and axial annulus strains from the anterior and posterior (avg. \pm st.dev.) were plotted against the number of splines.

6.2.4. Nucleotomy Strain Analysis and Validation

Each disc (n=5) underwent mechanical loading in the MR after nucleotomy, which was a previously published study using Vic2D texture correlation (O'Connell, Malhotra et al.). Reference and deformed images of intact discs and discs after nucleotomy were segmented into regions: AAF and PAF in ITK-SNAP (Figure 25).

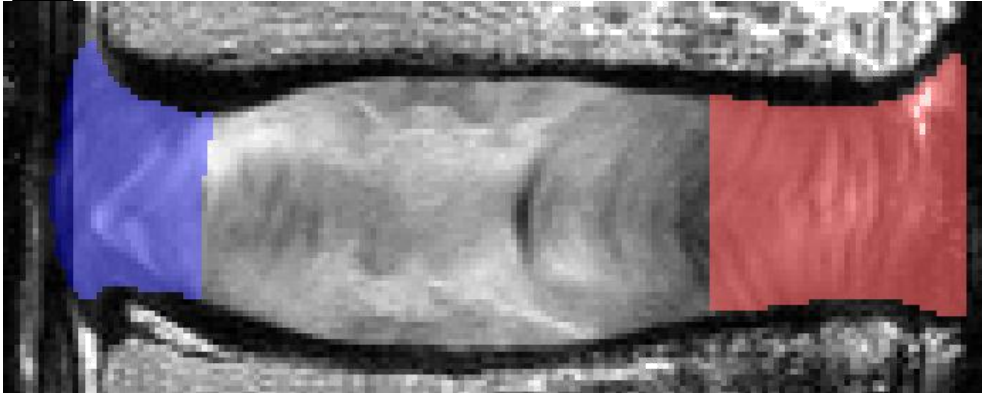


Figure 25: Segmentation of AAF (red) and PAF (blue) using ITK-SNAP. Each region was defined based on visible lamellae within each IVD.

The optimal registration (Section 6.2.3) was performed with ANTs. Axial and radial strains (avg. \pm st. dev.) were calculated in each region and strain maps were generated using the ANTs. Paired two-tail t-tests were performed comparing strains in the AAF and PAF between intact vs. nucleotomy data and ANTs vs. Vic2D (O'Connell, Malhotra et al.) ($p < 0.05$).

6.3. Results

6.3.1. Optimization of Image Registration Parameters

The optimal registration was determined to be an elastic transformation model, a directly manipulated free-form deformation (DMFFD: B-spline) regularization technique with 6x6 splines, and a mean squared similarity metric using a search radius of 2 and an outlier of 0.01. The effect of outlier value within a transformation model was only significant with regards to the vertebral body overlap statistics; target overlap ($p=0.016$), Hausdorff ($p=0.009$), and Average Hausdorff ($p \leq 0.001$). Post-hoc analysis showed an outlier value of 0.01 yielded significantly lower Hausdorff ($p=0.005$) and Average Hausdorff ($p=0.013$). Hausdorff values within the AF were significantly different ($p=0.012$), however post-hoc analysis showed no differences ($p=0.294$). All analysis testing the correlation between transformation models and outlier value showed significance. Post-hoc testing resulted in the elastic mapping being optimal in four of the five image pairs and an outlier of 0.01 was optimal for all cases. This registration had 68.90% target overlap, Hausdorff of 2.19 pixels, and Average Hausdorff of 0.36 pixels.

Strain standard deviation increased with the number of splines, while the average strain remained relatively constant between registrations (Figure 26). The 6x6 splines were selected since the average was stable with a lower standard deviation. Additionally, from 6x6 onwards, the qualitative strain patterns remained consistent.

6.3.2. Nucleotomy Strain Analysis and Validation

The effect on increased number of b-splines was found to be independent from nucleotomy (Figure 26).

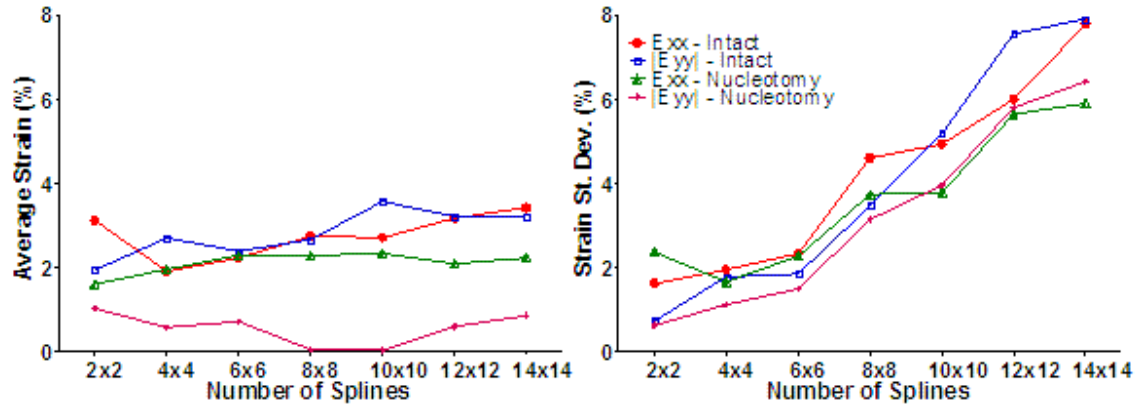


Figure 26: Representative plot on the effect of B-splines on AAF and PAF (A) Avg (B) St. dev. for axial and radial strain

The axial compressive strain increased in the PAF ($p=0.04$) and radial strain tended to decrease ($p=0.07$) for intact compared to after nucleotomy (Figure 27). No significant difference in strain was observed for registrations using ANTs and Vic2D for any groups or regions (Figure 27, $p=0.35$).

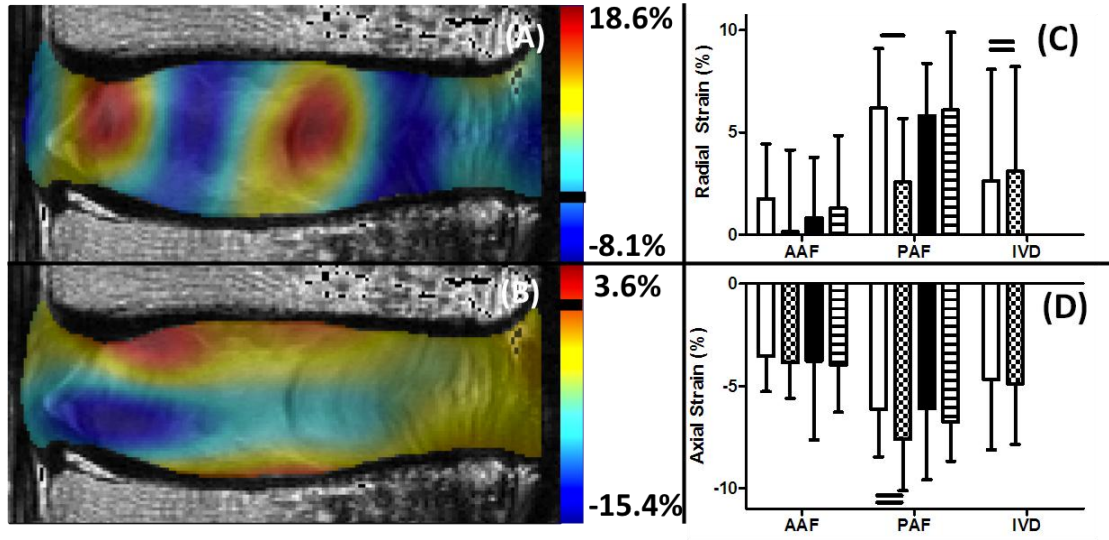


Figure 27: Representative (A) radial and (B) axial strain maps generated in ANTs. (C) Radial strains and (D) Axial strains measured in the AAF, PAF, and IVD in ANTs (intact white, nucleotomy checkered) and Vic2D (intact black, nucleotomy striped), == $p \leq 0.05$ & — $p \leq 0.10$.

6.4. Discussion

This study optimized parameters in Advanced Normalization Tools (ANTs) image registration as a method to measure intervertebral disc mechanics. Manual segmentation tools enabled registration accuracy verification assessing overlap statistics and comparing strain measurements before and after nucleotomy with Vic2d method of analysis (O'Connell, Vresilovic et al.). A B-spline regularization model has been implemented in this work and previously used to quantify myocardial strain in the heart (Tustison, Davila-Roman et al. 2003). In the B-spline model, a higher number of splines resulted in less smoothing within the strain map. Increasing the number of splines caused the strain standard deviation to rise, while the strain averages remained relatively constant. When the optimal mapping and outlier was used, increasing numbers of splines caused the target overlap to vary by less than 2% and the Hausdorff by less than 0.1 pixels. This result confirms that choosing 6x6 splines did not compromise feature detection.

At a 234 $\mu\text{m}/\text{pixel}$ image resolution, Hausdorff indicates a maximum shift of 500 μm between reference and deformed labels (approximately the width of one lamella), while the Average Hausdorff reports an average shift of 80 μm . The reference and warped labels overlapped by approximately 70%; slight variances can be seen from reference to warped (arrows Figure 22). Ideally overlap would be 100%, but this was not achieved due to human error in visualizing and marking anatomic features. The MR images had poor contrast between certain structures and image artifacts. Key anatomic features became more or less prominent in deformed images as individual substructures

such as AF lamellae moved in and out of plane. Since these issues compromised the ability to create accurate labels, we conclude that ANTs accuracy is greater than indicated in the overlap statistics.

Strain measurements with ANTs image registration for the disc were verified by comparing results with those from Vic2D texture correlation (O'Connell, Malhotra et al.) before and after nucleotomy. Nucleotomy causes an increase in axial PAF strain when quantified with both Vic2D (O'Connell, Malhotra et al.) and ANTs ($p=0.06$). Strain values were comparable between both techniques. Vic2D yielded a 30% increase and ANTs a 24% increase in axial strain as a result of nucleotomy in the PAF. The effect of radial strain in the PAF post-nucleotomy was also similar to Vic2D, which found a decrease of 50% ($p=0.01$) while ANTS showed a decrease of 58%. There were no significant difference between ANTs and Vic2D. However, the observed slight variance between them is likely due to ANTs ability to measure strain across the entire region of interest, potentially including areas that underwent greater deformation.

The verification and image registration techniques established here will act as the foundation for 3D image registration and strain analysis. The ability to track out-of-plane motion will greatly enhance the validity and accuracy for non-invasive strain measurements within the intervertebral disc.

CHAPTER 7 **Verification of Image Registration**

7.1. **Introduction**

The intervertebral disc functions to permit motion, distribute load, and dissipate energy in the spine. It performs these functions through its highly heterogeneous structural organization and biochemical composition consisting of several tissue sub-structures: the central gelatinous nucleus pulposus (NP), the surrounding fiber-reinforced layered annulus fibrosus (AF), and the cartilaginous endplates (CEP) that are positioned between the NP and vertebral endplates (Buckwalter and Mow 2000).. Disruption of any of the disc's tissues through aging, degeneration, or injury will not only alter the affected tissue mechanical properties, but also the mechanical behavior of adjacent tissues and, ultimately, the overall disc segment function. Thus there is a need to measure disc tissue and segment mechanics in the intact disc segment so that interactions between tissue structures are not disrupted. Such measurements would be valuable to study mechanisms of disc function and of disc degeneration, to design functional tissue engineered discs, and to develop and evaluate surgical procedures and therapeutic implants.

Disc mechanical behavior has been quantified through a number of measures including external displacements (Shah, Hampson et al. 1978, Reuber, Schultz et al. 1982, Stokes 1987, Holmes, Hukins et al. 1993) and internal pressure (Brinckmann and Grootenboer 1991, McNally and Adams 1992, Adams, McNally et al. 1996, Edwards, Ordway et al. 2001), however these do not fully establish internal tissue mechanics. Internal disc mechanics have also been measured through marker insertion or disc bisection (Seroussi, Krag et al. 1989, Kusaka, Nakajima et al. 2001, Meakin, Redpath et

al. 2001, Tsantrizos, Ito et al. 2005, Costi, Stokes et al. 2007). These studies have provided important data about disc mechanical function and how it changes with degeneration. Yet the disc is composed of soft hydrated, pressurized, and fibrous tissues that may deform separately from the inserted markers and may depressurize when bisected. Thus it has remained a challenge to quantify internal disc mechanics.

Magnetic resonance imaging (MRI) before and after an applied load, combined with image registration, is a promising method to quantify internal disc mechanics. Important advances have been made using MRI to measure internal disc deformation in a 2D plane (O'Connell, Malhotra et al. , O'Connell, Vresilovic et al. , O'Connell, Johannessen et al. 2007, Reiter, Fathallah et al. 2012, Chan and Neu 2013). Strains within several AF regions (e.g., anterior, posterior, lateral) were measured under applied axial compression and the effect of loading position, degeneration, and nucleotomy were determined (O'Connell, Malhotra et al. , O'Connell, Vresilovic et al. , O'Connell, Johannessen et al. 2007), demonstrating inhomogeneous strains across AF regions and differential effects of nucleotomy that depend on the initial state of degeneration (O'Connell, Malhotra et al. , O'Connell, Vresilovic et al. , O'Connell, Johannessen et al. 2007). A non-rigid image registration method was employed by (Reiter, Fathallah et al. 2012) to calculate mid-sagittal strain after creep loading. Displacement encoded MRI, an image tagging method that enables direct displacement measurements from MRI data, was used in (Chan and Neu 2013) to calculate strain across the entire disc under cyclic loading. While these are important advances, the 2D nature of recent MRI-based studies do not account for out-of-plane deformation nor provide the 3D strain components that are key to evaluating disc mechanical function.

The objectives of this study were to develop, validate, and apply a method to measure 3D internal deformations in intact human discs subjected to axial compression. This was achieved by using a custom-built loading device that permitted long relaxation times outside of the MRI scanner and maintained compression and hydration during imaging, by acquiring MR images at a high resolution (300 μm isotropic), and by applying state-of-the-art image registration methods.

7.2. Materials and Methods

7.2.1. Specimen Preparation

Human lumbar spines were procured, thawed, and scanned intact in a 3T whole-body MRI scanner (Trio, Siemens Medical Solutions) using the spine array RF coil. To assess degenerative grade, a T₂-weighted mid-sagittal image was acquired (Pfirrmann, Metzdorf et al. 2001), and to determine the nucleus pulposus T₂ relaxation time a T₂-mapping sequence was used (Marinelli, Haughton et al. , Welsch, Trattnig et al. , Watanabe, Benneker et al. 2007). To minimize anatomical and degenerative variability, grade 3 (Pfirrmann, Metzdorf et al. 2001) L4-L5 discs were selected (n=9), resulting in an average age of 57±12 years, an average NP T₂ relaxation time of 88.1 ± 16.6 ms, and an even gender distribution (5 female and 4 male). The L4-L5 lumbar spine was then dissected into a bone-disc-bone segment, the posterior elements removed, and the vertebral bodies potted in polymethyl methacrylate bone cement. Each sample was hydrated in a refrigerated phosphate-buffered saline (PBS) bath overnight and equilibrated to room temperature prior to testing.

7.2.2. Mechanical Loading and Image Acquisition

A custom-built non-magnetic loading frame (Figure 28A) was constructed to interface with an Instron 8874 for load application. The loading frame incorporated locking bolts to maintain axial compression applied using the Instron, a sliding tank to maintain hydration, and was designed to integrate with a two-piece RF coil (Helmholtz transmit, curved 4-channel receive array) (Wright, Lemdiasov et al. 2011) in a 7T whole-

body MRI scanner (Magnetom, Siemens Medical Solutions) (Figure 28B). The loading frame was fabricated using polyvinyl chloride (PVC) and Delrin plastics.

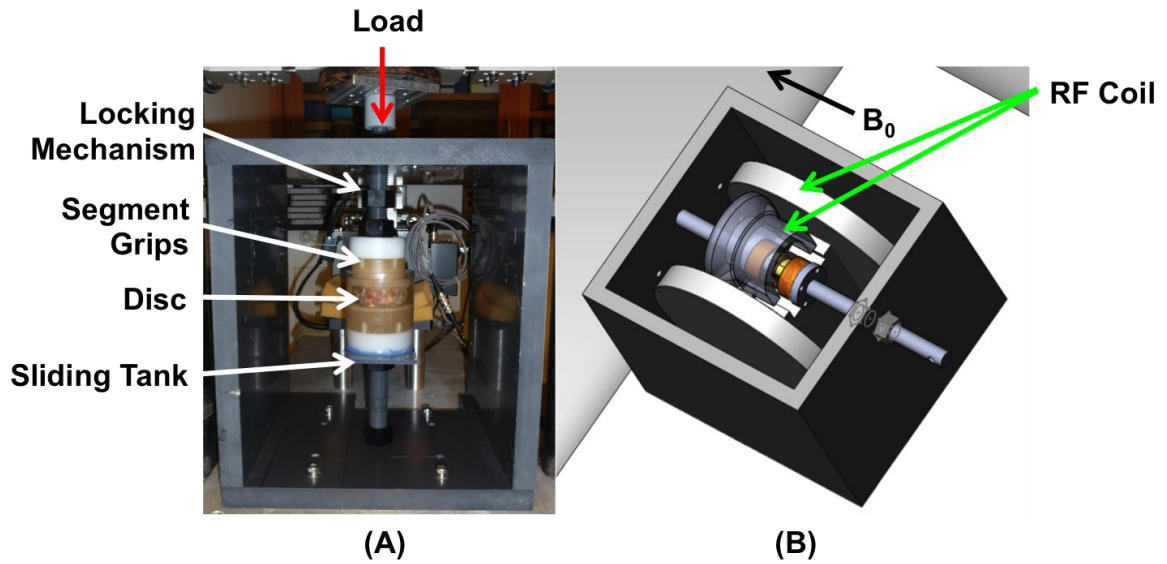


Figure 28: (A) Loading frame interfaced with Instron (red arrow), showing locking mechanism, segment grips, disc, and sliding tank (white arrows). (B) Loading frame integrated with RF coil (green arrows) in MRI. B_0 = direction of magnetic field.

A cylindrical sliding tank (diameter = 7.87 cm) made of acrylic held the disc and grips and allowed easy replacement of the PBS fluid (used while in the Instron) with 2% agarose gel (used while in the MRI scanner). The agarose gel maintained hydration during imaging and prevented image distortion at tissue edges due to the tissue-air mismatch in magnetic susceptibility (Schenck 1996). The disc-agarose unit was covered in plastic wrap throughout imaging to prevent dehydration. Sufficient space was maintained between the sliding tank and the outer walls of the frame in order for the coil array to be placed between them in the scanner and ports for wires were made within the outer frame walls (Figure 28B).

Mechanical loading followed by MR image acquisition was performed under four conditions: reference (50 N pre-load), 5%, 10%, and 15% applied grip-grip compressive

strain, as follows. The sample was placed in a PBS bath within the loading frame and installed in the Instron, which was used for load application. For the reference condition, a 50N pre-load was applied to ensure contact of the loading fixtures and held for 20 min., after which locking bolts were tightened to secure the position. The sample + frame then was removed from the Instron, and the PBS was removed and replaced with agarose.

The sample + frame was then placed within in the 7T MRI scanner and the 4-channel RF coil array placed to wrap around the sample (Figure 28B). High-resolution (300 μ m isotropic) MR images were acquired with a T2-weighted 3D turbo-spin echo sequence (TR/TE = 3000/34 ms, matrix = 256 x 256 x 32, turbo factor = 7, fat suppression). Scan time was 2.8 hours per disc per load.

After acquisition of the pre-load images, the agarose was replaced with PBS and the sample + frame was returned to the Instron. The Instron crosshead was returned to the pre-load position and the locking bolts were then loosened. A 5% grip-grip compressive strain, based on mid-sagittal disc height, was applied at a slow rate of 0.1 mm/s (Holmes, Hukins et al. 1993) and held for 2.5 hours of load-relaxation within the Instron. Average disc height was calculated by dividing the mid-sagittal disc space area by the anterior-posterior width from the pre-loaded reference image as previously described (O'Connell, Vresilovic et al. 2007). The position was again locked, PBS replaced with agarose, and the sample + frame returned to the MRI scanner for imaging under the loaded condition using the same imaging parameters as for the pre-load condition. These steps were repeated for 10% and 15% applied strain, always returning the Instron to the final displacement position of the previously applied load.

7.2.3. Image Processing and Registration

Image processing was performed prior to image registration. First, bone-disc-bone segmentations were generated for all images by masking out non-essential regions in the images, including agarose, and surrounding musculature, and most of the vertebral body. Because the imaging sequence was not optimized for bone contrast, deformation and strain analysis was not performed within the bone regions. This segmentation for each image set was performed using the 3D image edge-based snake tool in ITK-SNAP (Yushkevich, Piven et al. 2006), followed by manual correction of missed regions and sections that bled into the disc space. Second, to aid the alignment of similar features during registration, each image set was normalized to its maximum intensity value and the image sets were then histogram-matched. A representative resultant image set for a disc in the axial, coronal, and sagittal planes is shown in Figure 29A.

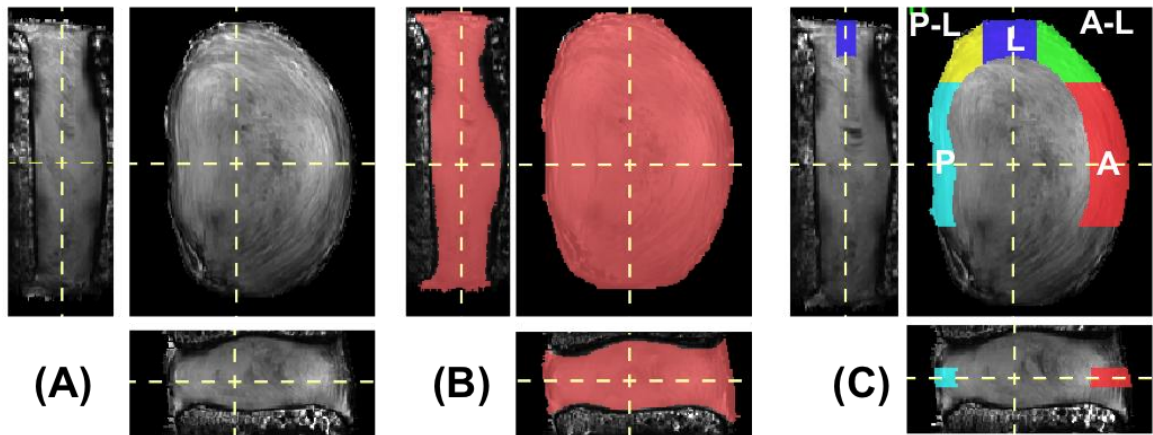


Figure 29: Images (A – C) are oriented to show coronal (left), axial (top-right), and sagittal (bottom) planes. (A) Representative MRI data set. (B) The volume used for strain analysis (pink). (C) Annulus fibrosus regions of interest defined in the mid-axial plane: A=anterior (red), A-L=anterior-lateral (green), L=lateral (purple), P-L= posterior-lateral (yellow), P=posterior (aqua).

Registration between reference (pre-load) and deformed (5%, 10%, and 15% compression) disc image sets was performed with Advanced Normalization Tools (ANTs) (Avants, Epstein et al. 2008, Tustison, Avants et al. 2009, Avants, Tustison et al. 2011, Tustison and Avants 2013). The resultant registration defines a warp field (Figure 30), which prescribes how the reference image transforms into the deformed image, and consequently, the inverse warp field prescribes how the deformed image transforms into the reference image.

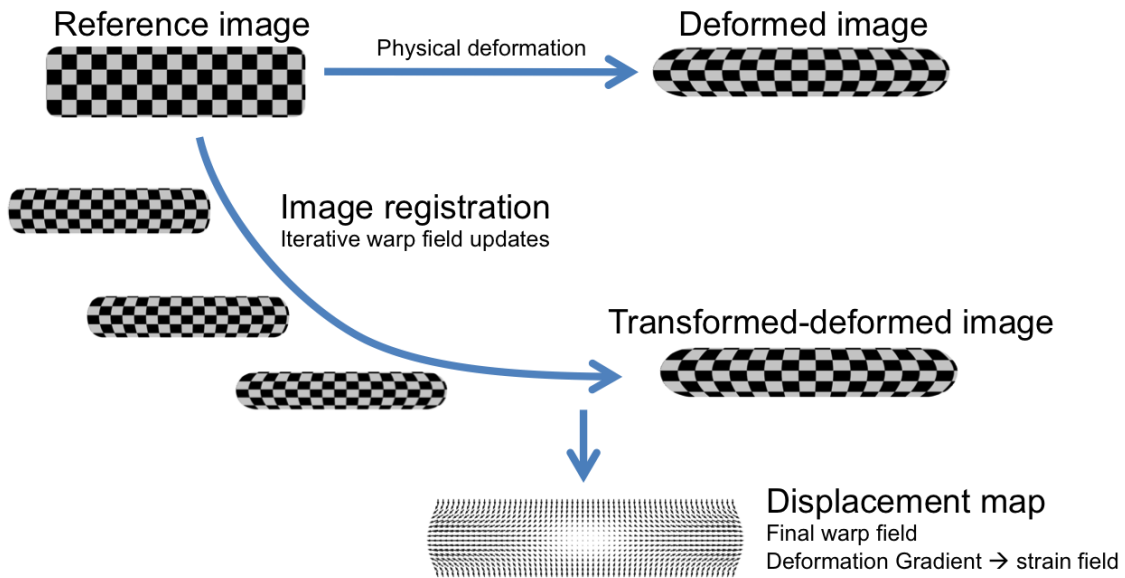


Figure 30: Pictorial representation of the image registration process, resultant warp field, and displacement map. The reference image is registered to the deformed image defining a warp field that prescribes how structures within the reference image are mapped to the deformed image. The deformation gradient tensor is applied to calculate the Lagrangian strain tensor.

Applying the warp field to the reference image creates a transformed-deformed image that appears identical to the deformed image; this approach can be applied in reverse using the inverse warp field. Lagrangian strain components were derived directly from the computed transformations (Tustison, Awate et al. , Tustison, Davila-Roman et al. 2003, Tustison and Amini 2006). ANTs performance has been validated in human brain

MRI registration (Klein, Andersson et al. 2009) and lung mapping (Murphy, van Ginneken et al. 2011), achieving top ranking in open competitions.

The procedure for using ANTs was as follows. An initial affine registration was applied which accounts for rigid body motion. A non-rigid registration was then performed using a symmetric diffeomorphic transformation model (Avants, Epstein et al. 2008). This transformation model was selected because it is invertible and is able to preserve topology and local neighborhood relations. Mean squared difference (MSQ) was employed as the similarity metric in the registration because of mono-modality and strong pixel intensity resemblance between the reference and deformed images. This metric performs the sum of the squared differences between corresponding intensity values between the reference (I_1) and deformed (I_2) image (Equation 15) such that ϕ is the iteratively updated warp field. To account for outliers, the MSQ equation was clipped by treating the equation linearly for intensity differences between the reference and deformed image that were greater than 0.01.

$$\text{Equation 15: MSQ} = 1/(n - 1) \sum (I_1(X) - I_2(\phi(X)))^2$$

A directly manipulated free-form deformation (DMFFD) regularization technique was utilized based on prior successful experience with its use in MR images (Tustison, Avants et al. 2009, Avants, Tustison et al. 2011, Tustison and Avants 2013). Preliminary experiments yielded 6x6x6 as the ideal number of splines for DMFFD regularization based on overlap statistics.

7.2.4. Registration Verification

Registration was validated with three different assessments: disc volume, lamellar structure, and axial strain. Disc volume and lamellar structure were evaluated using standard statistical assessment methods (Klein, Andersson et al. 2009). Disc volume validation was performed to assess gross morphology, ensuring registrations captured volumetric changes between the reference and deformed images. Lamellar structure validation was performed to verify registrations tracked internal AF displacements. Finally axial strain validation was performed to verify the strains calculated from the registration were as expected.

Disc volume and lamellar structure registration validation was performed by first identifying and “labeling” the matched features that are present in both the reference and deformed images – these labels are assumed to be the gold standard against which the registration is compared. Labeling these features entails manual segmentation using ITK-SNAP (Yushkevich, Piven et al. 2006). Labeling is highly labor intensive, therefore for these assessments a subset of samples was used for registration validation (n=3).

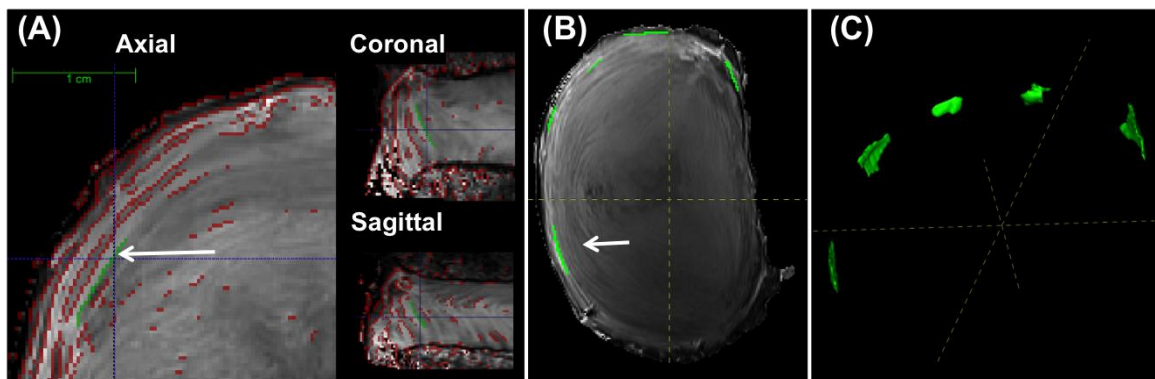


Figure 31: (A) Generation of lamellar structure labels using Sobel edge detection (red), shown in three planes. A representative label is shown in green. (B-C) Five identified lamellar labels, shown in mid-axial view and as 3D projections, respectively. Labels identified by white arrow.

For disc volume, a label image representing the entire disc was created by manually removing all pixels containing bone from each image set. For lamellar structure, labels representing the boundaries between adjacent AF lamellae were identified in three dimensions. Sobel edge detection was performed in 3D with a custom Matlab script to first identify AF boundaries (Figure 31A). These boundaries were then used to guide the identification of matched labels in the reference and deformed image sets (Figure 31B and Figure 31C). Five lamellar labels were identified around the circumference of each disc.

Once the five lamellar labels were identified in the reference and deformed images (5%, 10%, and 15% compression), the inverse warp field was applied to the deformed image labels to reconstruct the labels in the reference image. The reconstructed reference labels were then overlaid on the original reference labels to assess overlap statistics. Disc volume and lamellar structure were statistically evaluated for Target Overlap and Average Hausdorff (Klein, Andersson et al. 2009). Target overlap is the amount of overlap between the two images, where 100% represents a perfect registration. Average Hausdorff is the average pixel distance between matching label pixel boundaries, converted to length using 1 pixel = 300 μm image resolution, where 0 μm Average Hausdorff represents a perfect registration. For disc volume, 9 comparisons were made, 3 compression levels (5%, 10%, and 15%) across 3 samples. For lamellar structure, 45 comparisons made 5 labels per disc at 3 compression levels across 3 samples.

Finally, the axial strain was validated using all samples ($n=9$). Axial strain within the entire AF was averaged from the registration at each applied compression level. Manual segmentation of change in disc height was used to determine the axial strain for

comparison to the axial strain from registration. The disc height was manually segmented in the mid-sagittal and mid-coronal planes in the reference and deformed images. Axial strain was calculated as the change disc height between the reference and deformed image divided by the reference image disc height. For each sample, the axial strain was the average of the mid-sagittal and mid-coronal strain. Comparison between the axial strain from the registration and manual segmentation was made using a Pearson's correlation. Significance set at $p \leq 0.05$ and a trend defined by $0.05 < p \leq 0.10$.

The resultant applied strain measured from mid-axial disc was compared between groups, pre-load to 5%, 5% to 10%, and 10% to 15% compression. Difference between incremental strain groups was assessed by a one-way ANOVA with repeated measures and post-hoc comparisons with Tukey's test. Significance set at $p \leq 0.05$ and a trend defined by $0.05 < p \leq 0.10$.

7.2.5. Strain Analysis

Strain was calculated on a voxel-by-voxel basis from the warp field, ϕ , as follows. The warp field prescribes how features are mapped from the reference (X) to deformed (x) configuration (Tustison, Davila-Roman et al. 2003, Tustison and Amini 2006) in Equation 16, where V is the displacement field.

$$\text{Equation 16: } x = \phi(X) = V(X) + X$$

Next, the deformation gradient tensor (F) was calculated from the warp field $\phi(X)$ as,

$$\text{Equation 17: } F = \nabla \phi(X) = \nabla V(X) + \nabla X$$

Finally, the Lagrangian strain tensor (E) was calculated from the deformation gradient tensor. All of these analyses are performed within the ANTs software package (Tustison,

Davila-Roman et al. 2003, Tustison and Amini 2006). The Lagrangian strain tensor is initially calculated in the Cartesian coordinate system. These Cartesian strain components were then transformed into a local disc coordinate system and regional segmentation of the disc was performed, as described below.

To transform the Cartesian coordinate system, a local disc coordinate system was established based on the disc's outer contour (Figure 32).

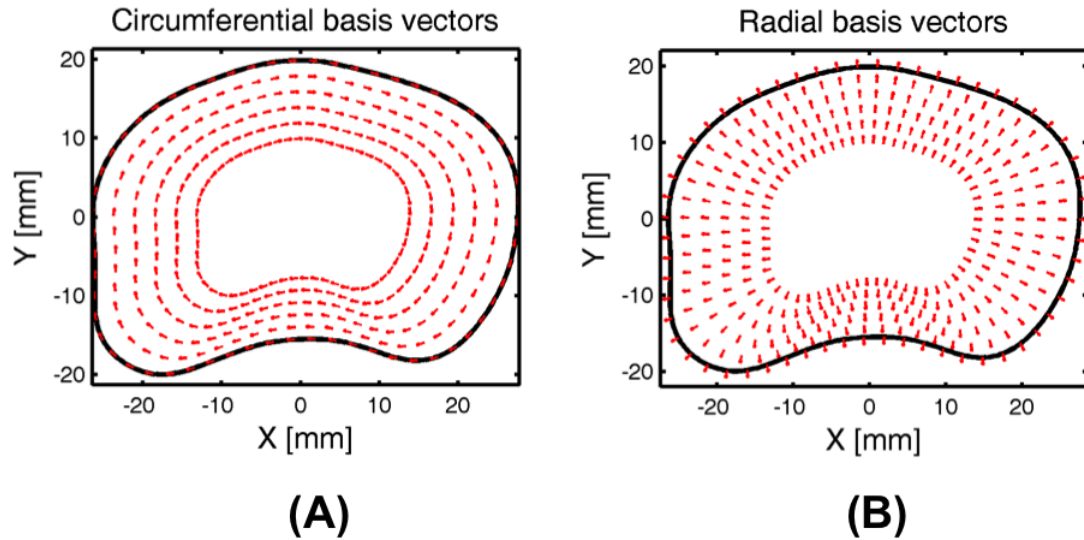


Figure 32: Transformation of Cartesian coordinates to local disc coordinates using the disc's outer contour, scaled to intersect each voxel: (A) circumferential basis vectors defined by the contour's tangent; (B) radial basis vectors defined by the contour's normal. Note the complex vector directions imposed by the lamellar curvature.

The outer contour was defined by tracing the projection of the disc into the x-y plane and its origin defined as the disc's centroid. For each voxel, the contour was scaled to find a similar contour that intersected the voxel's (x, y) position. The local coordinate system (B) is defined by the circumferential basis vector ($e_{\theta\theta}$) was defined by the contour's tangent, the local radial basis vector (e_{rr}) was defined by the contour's normal, and the local axial basis vector (e_{zz}) remained unchanged from the primary spine axis. The

Cartesian strain tensor (E) at each voxel in the x-y plane was then transformed into disc specific strain tensor (E') having components of circumferential strain ($E_{\theta\theta}$), radial strain (E_{rr}), and axial strain (E_{zz}) using the transformation (Equation 18),

$$\text{Equation 18: } E' = B^{-1}EB$$

The disc was next segmented to establish volumes of interest for averaging local strains. First, to eliminate artifacts that occur in the registration at the bone-disc boundary (Pech and Haughton 1985), the disc area was removed by two pixels depth (0.6 mm) at the superior and inferior boundaries using the image erosion function in Matlab maintaining the bone-disc boundary contour. Next, to remove any remaining strain outliers, the intersection of axial, circumferential, and radial strain values that were ± 2 standard deviations from the mean were eliminated, providing the final segmented disc for strain analysis (Figure 29B). Finally, the AF was defined by excluding regions where Sobel 3D edge detection did not locate lamellar edge boundaries. The AF segmentation outer boundary followed the outer disc contour and the AF inner boundary was defined by the inner most medially detected AF lamellar edge. To ensure no NP material fell within this segmentation, the NP region was defined to occupy 28% of the disc cross-section, positioned at the discs centroid with a 3% posterior translation, and mirrored the outer contour (O'Connell, Vresilovic et al. 2007). To achieve relatively homogenous strain regions, the mid-axial height, defined as the middle third of the disc height after segmentation, represented the AF region of interest. The AF was then divided into Anterior, Anterior-Lateral, Lateral, Posterior-Lateral, and Posterior (Costi, Stokes et al. 2007) regions (Figure 29C). The lateral region furthest from the RF coil was excluded because of reduced image contrast. Mean axial, circumferential, and radial disc strain

values were calculated for each region at the mid-axial disc height. Variance between regions as assessed by a one-way ANOVA and post-hoc comparisons with Tukey's test for 5%, 10%, and 15% compression. Significance set at $p \leq 0.05$ and a trend defined by $0.05 < p \leq 0.10$.

7.3. Results

In this study three dimensional image registration of the human intervertebral disc in axial compression loading was performed, the registration was validated, and then strain analysis in compression was performed. The high-resolution isotropic MR images provided excellent visualization of the AF lamellar architecture (Figure 29 and Figure 30), features essential for successful registration.

7.3.1. Registration Verification

Registration was validated with three different assessments: disc volume, lamellar structure, and axial strain. Disc volume and lamellar structure were statistically evaluated for Target Overlap and Average Hausdorff. These are standard assessment methods and were compared against the previous successful registration of human brain (Avants, Tustison et al. 2011). The disc volume was registered with a Target Overlap of $94.4 \pm 0.92\%$. This target overlap is similar to the best registration achieved in human whole brain of 95.8% (Avants, Tustison et al. 2011). The disc volume was registered with an Average Hausdorff of 0.030 ± 0.006 mm. Excellent overlap was achieved internally between the original and reconstructed AF labels (Figure 33).

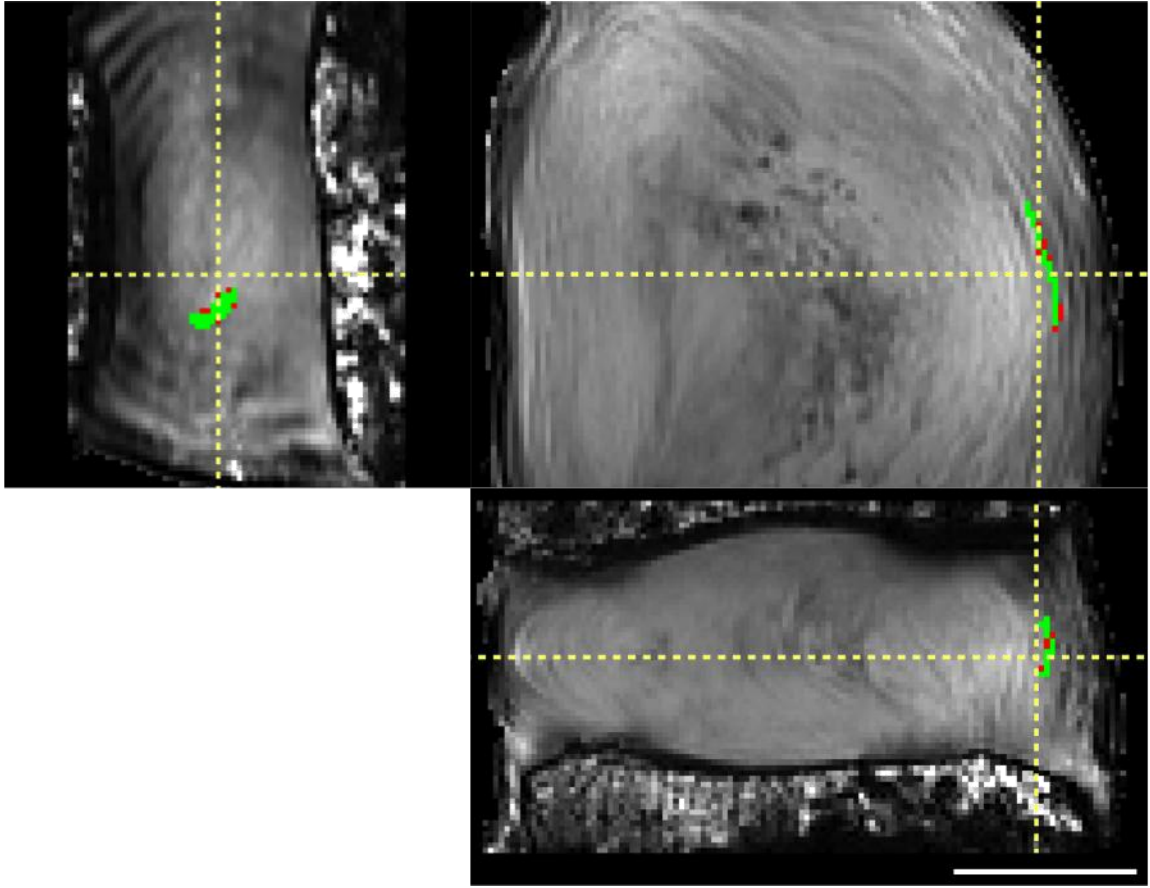


Figure 33: Registration of a representative lamellar label (green), shown in coronal (left), axial (top-right), and sagittal (bottom) views. Difference between original and registered label is small (red), demonstrating good registration. Scale bar = 1cm

The lamellar structure was registered with a Target Overlap of $65.2 \pm 12.4\%$. This Target Overlap is similar to the registration achieved in human brain subcortical structures of 66.9% (Avants, Tustison et al. 2011). The lamellar structure was registered with an Average Hausdorff of 0.12 ± 0.06 mm.

The axial strain was validated by comparing the axial strain calculated by ANTs, averaged across the entire AF, to axial strain measured directly from the change in disc height on the MR images. This validated not only the registration methods but also the strain analysis calculations. There was a linear correlation between the axial strain from the registration and the manually measured strain ($R^2=0.79$, $p<0.001$, Figure 34). No

statistical difference was found between the each of the achieved applied strain increments between pre-load to 5%, 5% to 10%, and 10% to 15% compression ($p = 0.34$).

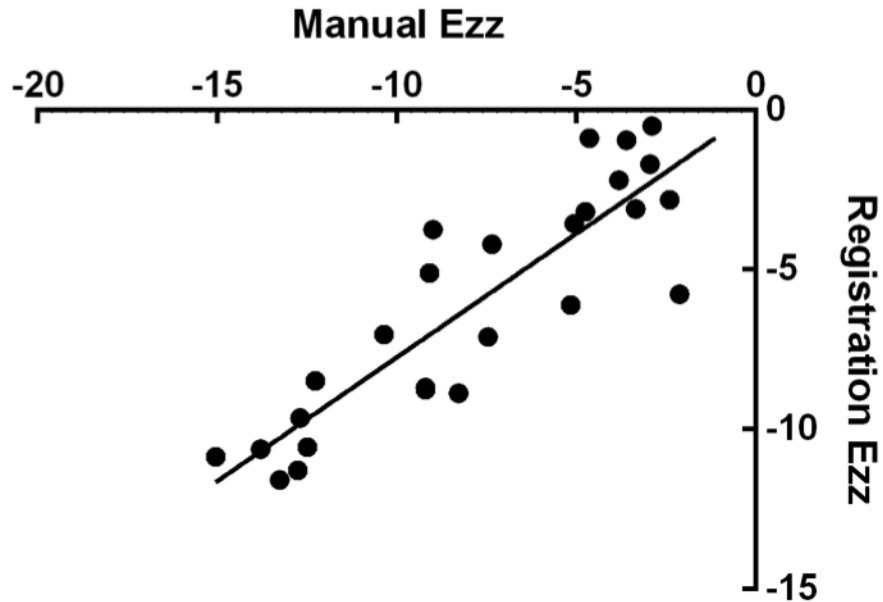


Figure 34: Axial strains for all discs obtained by manual measurement and by image registration, showing good agreement ($r^2=0.79$, $p<0.05$).

7.3.2. Strain Analysis

The three strain components under all applied axial compressions were qualitatively evaluated; a representative disc at 10% axial strain is shown in Figure 35.

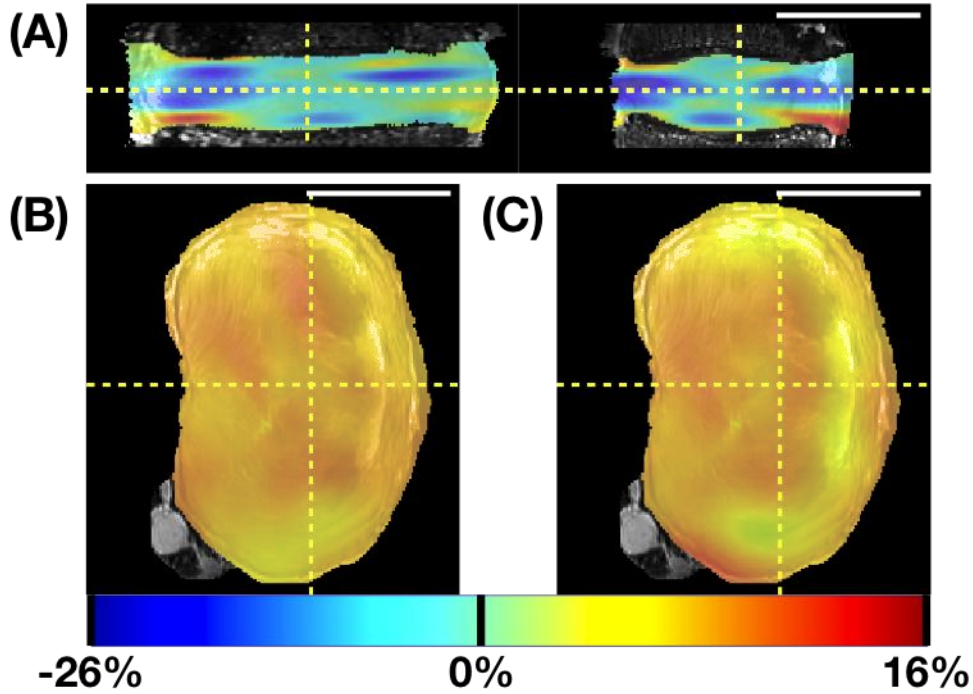


Figure 35: Strain maps for 10% axial compression in a representative disc: (A) axial strain in coronal and sagittal views (left and right, respectively); (B) circumferential strain in axial view; (C) radial strain in axial view. Scale bar = 5 cm.

Qualitative strain patterns described below were generally similar for all levels of applied strain across all discs. Axial strain (E_{zz}) had horizontal banding throughout the disc, as shown in the coronal and sagittal views (Figure 35A). Negative E_{zz} strains predominated, although bands of tensile E_{zz} strains occurred near the disc–endplate boundaries (Figure 35A). Circumferential strain ($E_{\theta\theta}$) was near zero at the endplates (not shown) and had high positive strain values occurring in the posterior and lateral regions, as shown in the axial view (Figure 35B). Radial strain (E_{rr}) decreased from the inner AF toward the periphery of the AF. The E_{rr} strains were positive in the inner AF regions and near zero at the AF outer boundary, as shown in the axial view (Figure 35C).

The peak and equilibrium stress increased with each applied strain increment (Table 6). The magnitude of the strain components, averaged across the entire AF, also

increased with each applied increment (Table 6). The AF E_{zz} did not match the applied grip-grip strain (Table 6), however it did increase linearly with each strain increment (Figure 34).

	Applied Compression		
	5%	10%	15%
Peak compression stress (kPa)	192 \pm 29.1	307 \pm 141	352 \pm 222
Equilibrium compression stress (kPa)	40.0 \pm 18.3	110 \pm 15.0	174 \pm 27.1
AF E_{zz}	-3.30 \pm 5.58%	-7.59 \pm 6.31%	-13.17 \pm 6.32%
AF $E_{\theta\theta}$	0.70 \pm 1.02%	1.23 \pm 1.29%	2.75 \pm 2.07%
AF E_{rr}	0.11 \pm 1.86%	0.96 \pm 2.44%	1.63 \pm 2.93%

Table 6: Mean \pm standard deviation of stress and strain for each applied loading condition. Note that Applied Compression represents grip-to-grip applied strains that are compressive and that these compressive boundary conditions induce negative axial strain. AF = annulus fibrosus, E_{zz} = axial strain, $E_{\theta\theta}$ = circumferential strain, E_{rr} = radial strain. Stress calculated as load divided by area from axial reference MR image. Strains averaged over entire AF volume for each disc. N= 9.

Because the strains were expected to be inhomogeneous across the AF, separate AF regions were defined and strains averaged within these regions. To avoid boundary effects at the bone attachment, the middle third (Figure 29C) of the disc was considered as “mid-axial” with five AF regions delineated as: anterior (A), anterior-lateral (A-L), lateral (L), posterior-lateral (P-L), and posterior (P). Differences in strain across AF regions were evaluated for 15% applied axial compression (Figure 36).

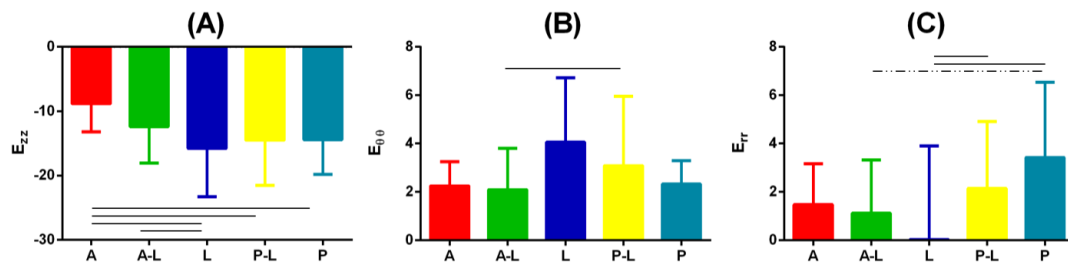


Figure 36: Mean (standard deviation) of AF regional strain at mid-disc height when loaded to 15% compression for (A) axial, (B) circumferential, and (C) radial strain. A=Anterior, A-L=Anterior-Lateral, L=Lateral, P=L=Posterior-Lateral, P=Posterior. Region locations are shown in Figure 2C. A solid line represents significance $p < 0.05$ and dashed line a trend $0.05 < p < 0.10$.

Axial strain (E_{zz}) was smallest in the anterior AF, significantly smaller compared to the lateral, posterior-lateral, and posterior AF ($p < 0.03$, Figure 36A). Circumferential strain ($E_{\theta\theta}$) in the anterior-lateral AF was smaller than the posterior-lateral AF ($p = 0.02$, respectively, Figure 36B). Radial strain (E_{rr}) was lowest in the lateral AF, significantly lower than the posterior-lateral and posterior AF ($p < 0.04$, Figure 36C). In addition, the radial strain was highest in the posterior AF, higher than the anterior-lateral ($p < 0.07$) and lateral AF ($p < 0.003$, Figure 36C).

7.4. Discussion

In this study a method to measure 3D internal deformations within intact human discs under axial compression was developed, validated, and applied. Important technical advances included a custom-built loading device that permitted long relaxation times outside of the MR scanner and maintained compression and hydration throughout imaging, a high-resolution 300 μm isotropic MR imaging sequence, and state-of-the-art image registration methods. There is a need to measure disc tissue and segment mechanics in the intact disc segment so that interactions between tissue structures are not disrupted. Such measurements established in this study are valuable to study mechanisms of disc function and of disc degeneration, to design functional tissue engineered discs, and to develop and evaluate surgical procedures and therapeutic interventions. In addition, finite element models used to study disc mechanics (Shirazi-Adl, Shrivastava et al. 1984, Goel, Monroe et al. 1995, Argoubi and Shirazi-Adl 1996, Fagan, Julian et al. 2002), have to date only performed model validation with respect to overall deformation at outer boundaries. The experimental internal strain data achieved in this study will be valuable to validate the internal strains predicted by finite element models.

The image registration was validated using both the disc volume and lamellar structure. Using standard statistical methods (Klein, Andersson et al. 2009), both the disc volume and lamellar structure had very good accuracy, strongly supporting the validity of the registration and the reported strain results. There are no directly comparable image registrations, but work has been published on whole brain registrations (Avants, Tustison et al. 2011). The disc volume validation can be compared to previous whole brain

registration, where the disc Target Overlap was 94% and brain was 96% (Avants, Tustison et al. 2011). Similarly, the lamellar structure validation, representing internal registration of fine detail, can be compared to brain cortical features, which are also internal. In this case lamellar structure Target overlap was 65% while brain cortical was 67% (Avants, Tustison et al. 2011). It is likely that the apparently reduced accuracy inside the disc reflects the challenges and errors in visualizing and marking these internal anatomic features to create the labels. The use of 3D Sobel edge detection to locate the lamellar boundaries was helpful in identifying lamellar features. Although the 300 $\mu\text{m}/\text{pixel}$ resolution achieved in this study is outstanding for disc MRI, identification of lamellar labels for validation was quite difficult given the 140 – 520 μm range of AF lamellar thickness (Marchand and Ahmed 1990). Nonetheless, qualitative evaluation of overlap of lamellar labels shows excellent correspondence (Figure 33) and quantitative validation matches the current standard in the field. Moreover, the implementation of overlap statistics on manual segmentations provides registration accuracy that is specific to the experimental conditions, a distinct advantage over to utilizing MR phantoms (Chan and Neu 2013) or computer generated deformations (Reiter, Fathallah et al. 2012).

Qualitative observations of the strain patterns were made. Axial strain horizontal banding was apparent (Figure 35A), similar to those observed in the 2D strain analysis by O'Connell *et al.* (O'Connell, Johannessen et al. 2007). Large tensile axial strains were observed at the boundary of the AF and vertebral endplate (Figure 35A), which was also consistent with previous work (O'Connell, Vresilovic et al. , O'Connell, Johannessen et al. 2007). The mechanism for axial tensile strain to occur when the disc is being compressed is not clear, however, we hypothesize that it may be related to tension in the

AF fibers at their insertion to the vertebrae, and/or the curvature of the endplate. Notably, compressive axial strains that were greater than the applied strain magnitude were observed in some regions, particularly in the mid-height region (Figure 35A), which makes some intuitive sense, when there is axial tension at the endplates. Integration of the axial strain across the disc in the z-direction at any fixed radial and circumferential coordinate would yield the total displacement in the z-direction, which ideally would be the same throughout the disc if the endplates were flat. The mechanical and biological effects these strain patterns have on local matrix and cells are a subject of future interest.

Strain maps not only enable qualitative visualization of strain patterns, but also enable quantitative regional AF strain analysis. In this study small regions of relatively homogenous tissue at the mid-disc height were evaluated (Figure 29C) and the strains under applied axial compression compared in regions around the disc (Figure 35). Axial strain was lowest in the anterior AF ($-8.8 \pm 4.4\%$) and highest in the lateral AF ($-15.8 \pm 7.5\%$), Figure 35A. This is likely related to the larger disc height in the anterior region. Since strain can be estimated as change in height divided by the reference height, if the anterior region has a higher reference height, it follows it would have a smaller strain for the same applied deformation. Circumferential strain was lowest in the anterior and anterior-lateral regions ($2.2 \pm 1.4\%$) and highest in the lateral region ($4.1 \pm 2.7\%$). Geometrically it is expected that circumferential ‘hoop’ strain would be highest at the largest radial distance from the disc center, which is the lateral AF. Radial strain was lowest and on average zero in the lateral AF and highest in the posterior AF. The low average strain in the lateral AF also had a very high standard deviation, suggesting a large degree of strain inhomogeneity that may be related to the steeper curve around the AF

contour at the lateral side. The higher radial strain in the posterior AF may be physiologically important for delamination and tears in the posterior regions of the disc, and may have important implications in this area where AF failure and disc herniation often occur.

The axial stress associated with the applied compression strains were calculated (Table 6) and can be related to in vivo lumbar disc stresses measured in the nucleus pulposus with a pressure transducer (Wilke, Neef et al. 1999). The stress associated with the applied 5% compression is comparable to lying down, the 10% compression is comparable to the stress to lying prone with an extended back supported on elbows and sitting slouched in a chair, and the 15% compression is comparable to a large number of activities, including sitting down and relaxed standing (Wilke, Neef et al. 1999). Thus the compressions applied in this study have physiological relevance. While this study was not designed to study the disc stress-relaxation, we did observe a viscoelastic response (Table 1) consistent with previous studies (Johannessen, Vresilovic et al. 2004, Beckstein, Sen et al. 2008, O'Connell, Jacobs et al. 2011) and that suggests nonlinear response that was expected based on known nonlinear disc mechanics (Keller, Spengler et al. 1987, Holmes and Hukins 1996, Johannessen, Vresilovic et al. 2004, Perie, Korda et al. 2005).

An advantage of this study is that 3D image registration was performed. Prior 2D image correlation experiments (O'Connell, Malhotra et al. , O'Connell, Vresilovic et al. , O'Connell, Johannessen et al. 2007, Reiter, Fathallah et al. 2012, Chan and Neu 2013) were designed to minimize out-of-plane deformations that could cause erroneous strains to be reported if the same tissue is not present in both the reference and deformed images.

To check this, the strains in this study were compared to previous 2D correlations (O'Connell, Johannessen et al. 2007). Although different samples and slightly different protocols were used (the present study applied 5% compression, the previous study (O'Connell, Johannessen et al. 2007) applied 1000 N compression), both studies achieved very similar applied axial disc strains, $E_{zz} = -4.27 \pm 1.48\%$ and $E_{zz} = -4.4 \pm 1.3\%$ strain, respectively. Therefore, the AF strains computed in 3D and mid-sagittal 2D can be compared with some confidence. This finding was not unexpected since axial compression was applied in both studies. The average AF axial strains were $E_{zz} = -3.6\%$ and -4.7% and the average AF radial strains were $E_{rr} = 2.2\%$ and 2.1% in the present 3D study and the previous 2D study (O'Connell, Johannessen et al. 2007), respectively. This is excellent correspondence given the differences in protocols, human sample variability, imaging and registration methods, and strain inhomogeneity. This observation provides confidence in both the present work and the remaining validity of the previous 2D studies. The ability to quantify out-of-plane motion will enable future 3D disc strain analysis in other loading configurations, such as rotation and bending, where less uniform deformations are expected.

The methods in this study are subject to some limitations. Long imaging times limit analysis to studies in which the disc is at steady state, and dynamic loading studies are not currently feasible with the described methods. Similar to other loading studies (Stokes 1987), the applied grip-grip compression overestimated the actual strain experienced by the disc: for applied 5, 10, and 15% grip-grip compression the manual segmentation averaged in the mid-sagittal and mid-coronal images were $-4.3 \pm 1.3\%$, $-9.3 \pm 0.9\%$, and $-12.0 \pm 0.9\%$, respectively. This is due deformation within the loading frame

fixtures and possibly deformation during locking of the loaded position prior to imaging. The loading frame's driving rod's thread pitch was comparable to the average applied 5% compression increment of 0.78 ± 0.07 mm. Additionally, it is likely that some deformation occurred within the vertebral bodies, as they are not rigid, particularly with osteoporosis (Hansson, Roos et al. 1980, McBroom, Hayes et al. 1985, Cheng, Nicholson et al. 1997, Ebbesen, Thomsen et al. 1999). The difference between grip-grip compression and actual strain is not itself problematic, however, it does increase variability when grouping samples for statistical analyses.

This study was performed in cadaveric discs and is not currently available for in vivo applications. To achieve high-resolution isotropic images used in this study, significant improvements to current spine surface coils and MRI sequence development will be needed. Nonetheless, MR-based biomechanical studies have been performed in vivo, where disc volume changes have been quantified following axial loading (Danielson and Willen 2001) and simulated diurnal loading (Malko, Hutton et al. 1999). Thus, future imaging advances could be translated to in vivo study.

In conclusion, key technical advances were made to develop and validate a new method to measure 3D internal strains in intact human discs. The 3D strain components were obtained for both qualitative and quantitative analysis and compared across AF regions. Three-dimensional spatial variation in the three strain components indicate complexities in the material mechanical properties and disc stresses not heretofore appreciated. Some of the variation in magnitude of axial and circumferential strain might be explained by disc geometry. Overall this study provided new methods that will be valuable in future work. The observed strain inhomogeneity may have implications for

both tissue mechanics and cell mechano-transduction, as nearby cells might experience wildly different mechanical environments. These techniques will be valuable in the design, the development, and the evaluation of surgical procedures and therapeutic interventions. Moreover this work should advance analysis of internal mechanics in other musculoskeletal joints to quantify strains in tendon, ligament, and meniscus within an intact joint.

CHAPTER 8 Regional Strain of the Annulus Fibrosus under Axial Compression

8.1. Introduction

The intervertebral disc substructures, annulus fibrosus (AF), nucleus pulposus (NP), and cartilaginous endplates (CEP) work together to distribute multidirectional loads in compression, torsion, and bending. Degeneration alters the discs structural integrity and mechanics, affecting the mechanical interaction of these substructures. Data within the literature quantifying the effects of degeneration on 3D internal strain distributions in compression is limited. Experimental whole-disc testing is limited to providing global disc load and deformation details, not internal mechanics information. The ability to quantify regional internal disc mechanics through non-invasive measures would yield vital information regarding disc function aiding the study of disc degeneration, implant development, and surgical procedure evaluation.

The AF is a structured composite of alternating concentric lamellae that consist of collagen bundles embedded in a matrix of proteoglycans and non-fibrillar collagens. This organized structure exhibits regional heterogeneity within the IVD circumferentially and radially (Marchand and Ahmed 1990, Tsuji, Hirano et al. 1993). Fiber orientation alternates between each layer 28° - 43° above and below the transverse plane (Hickey and Hukins 1980, Marchand and Ahmed 1990), with fiber angle increasing from outer to inner AF. The distinctive outer AF predominantly comprises of Type I collagen and some Type II. Lamellae become less distinct along the radial direction from outer to inner AF toward the NP as a result of increased Type II and decreased Type I collagen content

(Eyre and Muir 1976, Eyre and Muir 1977, Buckwalter 1995). As a result, 40-80% of the inner AF lamellae are incomplete and interconnecting creating a less distinct structure (Marchand and Ahmed 1990, Tsuji, Hirano et al. 1993). Lamellar thickness varies by location (anterior / posterior / lateral) within the disc and becomes thicker toward the NP ranging from 140 – 520 μm (Marchand and Ahmed 1990). The fibers of the AF's outer lamella are attached to the vertebra, while the inner lamellas merge with the CEP. These regional differences in composition, structure, and boundary conditions suggest regional internal heterogeneous mechanical behavior within the IVD.

The primary function of the AF is to aid the IVD in distributing multidirectional loads related to compression, torsion, flexion/extension, and lateral bending. An improved understanding of internal regional IVD mechanical behavior under native boundary conditions will provide critical information for understanding disc pathogenesis and design criteria for treatments that aim to restore mechanics. The AF exhibits anisotropic mechanical properties in tension (Skaggs, Weidenbaum et al. 1994, Acaroglu, Iatridis et al. 1995, Ebara, Iatridis et al. 1996, Elliott and Setton 2000, Elliott and Setton 2001, O'Connell, Guerin et al. 2009), shear (Iatridis, Kumar et al. 1999, Fujita, Wagner et al. 2000, Jacobs, Smith et al. 2011), and compression (Perie, Maclean et al. 2006, Cortes and Elliott 2012, Cortes, Han et al. 2013). In-vivo boundary condition replication is challenging, particularly when attempting to imitate torsion and bending with shear ex-vivo shear testing (Jacobs, Smith et al. 2011). Due to tissue dimension constraints in mechanical testing, IVD disc height is often not long enough to analyze differences in the axial direction. Ex-vivo mechanical testing has shown AF regional material property variability in the radial and circumferential direction. Along the radial direction

mechanical properties progressively increase from the inner to outer AF (Skaggs, Weidenbaum et al. 1994, Ebara, Iatridis et al. 1996, Fujita, Duncan et al. 1997, Fujita, Wagner et al. 2000), with the outer exhibiting shear and tensile modulus 3-5X greater than the inner AF (Ebara, Iatridis et al. 1996, Fujita, Wagner et al. 2000). Around the circumferential direction the anterior AF demonstrates stronger mechanical properties with tensile and shear moduli 2X greater than the posterior and posterior lateral AF (Galante 1967, Fujita, Duncan et al. 1997, Spera, Genovese et al. 2011). Circumferential variability is further highlighted though surface strain measurements of the outer AF under axial compression, exhibiting peak values in the posterior lateral region (Shah, Hampson et al. 1978, Stokes 1987, Heuer, Schmidt et al. 2008, Kawchuk, Kaigle Holm et al. 2009). Previous work has indicated that axial compression creates complex strain patterns to the AF (Shah, Hampson et al. 1978, Bruehlmann, Matyas et al. 2004, O'Connell, Johannessen et al. 2007, Heuer, Schmidt et al. 2008) within the IVD. Regional strain analyses have been limited to mid-axial ex-vivo tissue testing, surface strain measurements, and two-dimensional internal strain analysis (Galante 1967, Shah, Hampson et al. 1978, Stokes 1987, Skaggs, Weidenbaum et al. 1994, Acaroglu, Iatridis et al. 1995, Ebara, Iatridis et al. 1996, Fujita, Duncan et al. 1997, Iatridis, Kumar et al. 1999, Elliott and Setton 2000, Fujita, Wagner et al. 2000, Elliott and Setton 2001, Bruehlmann, Matyas et al. 2004, Perie, Maclean et al. 2006, O'Connell, Johannessen et al. 2007, Heuer, Schmidt et al. 2008, Kawchuk, Kaigle Holm et al. 2009, O'Connell, Guerin et al. 2009, Jacobs, Smith et al. 2011, Spera, Genovese et al. 2011, Cortes and Elliott 2012, Cortes, Han et al. 2013).

The heterogeneous composition and structure of the annulus fibrosus will result in regional strain differences along the discs principle directions (radial, circumferential, and axial). The objective of this chapter is to characterize the regional internal IVD strain under incremental amounts of axial compression. Utilizing techniques developed in Chapters 4-7, three-dimensional annular strain will be measured throughout the entire disc volume. Comparisons will be made along the radial (inner and outer annulus), circumferential (anterior: A, anterior-lateral: A-L, lateral: L, posterior-lateral: P-L, and posterior: P annulus), and axial (inferior, middle, and superior third annulus) direction.

8.2. Materials and Methods

8.2.1. Specimen Preparation

Degenerative grade 3 (Pfarrmann, Metzdorf et al. 2001) human lumbar L4L5 (n=9, T2=88.07±16.61 ms, age=57±12, gender=5F/4M) bone-disc-bone motion segments from Chapter 7 were analyzed for AF regional strain properties in this section. Samples were not retested; overlapping Chapter 7 methods will be discussed in brief. Bone-disc-bone motion segments with posterior elements removed were potted in polymethyl methacrylate (PMMA) bone cement for mechanical testing. Samples were hydrated in a refrigerated, phosphate-buffered saline (PBS) bath overnight and equilibrated to room temperature prior to testing.

8.2.2. Mechanical Testing and Image Acquisition

A custom-made, non-magnetic loading frame interfaced with an Instron 8874 to perform axial compression, as described in Chapter 5. The loading protocol from Chapter 7.2 is described in brief. Potted samples were placed in a PBS bath within the loading frame and an initial 50N pre-load was applied for 20 min. Pre-load “reference” position was locked into place, PBS replaced with 2% agarose gel, and the loading frame was removed from the Instron for reference position image acquisition. High-resolution 3D 300 μm isotropic MR images were acquired using imaging parameters from Chapter 7.2.3. After image acquisition the loading frame was returned to the Instron, agarose replaced with PBS, and pre-load position returned. Based on the average disc height taken from a mid-sagittal image in the reference condition, a 5% grip-to-grip strain was

applied at a slow 0.1 mm/s ramp rate (Holmes, Hukins et al. 1993) and allowed to relax for 2.5 hours. These steps were subsequently repeated twice more to achieve 10% and 15% applied strain.

8.2.3. Image Registration

All image sets were pre-processed to remove non-essential information. Reference position and strained image grayscale values were histogram-matched after normalization to their respective maximum intensity value [Figure 29B]. The pre-loaded image (reference) was then registered to the 5%, 10%, and 15% applied strain images respectively. An initial affine registration was performed to account for rigid body motion prior to a non-rigid registration with a symmetric diffeomorphic transformation model (Avants, Epstein et al. 2008), mean-squared difference similarity metric, and directly manipulated free-form deformation regularization technique (Tustison, Avants et al. 2009). The resultant registration defines a warp field, which prescribes how the reference image transforms into the deformed image.

8.2.4. Strain Analysis

A local coordinate system was established [Ch5-Figure 4] based on the disc's outer contour. Strain components were defined as follows; circumferential ($E_{\theta\theta}$) is tangent to disc's contour, radial (E_{rr}) normal to the contour, in-plane shear ($E_{\theta r}$), and the axial (E_{zz}) based on the primary axis of the spine. The local Cartesian strain tensor was transformed into these local coordinates [Chapter 7.2.6]. Utilizing techniques from Chapter 7.2.5-6, the disc was segmented by removing all pixels containing bone, then

eroding 2 pixels at the bone-disc interface with Matlab's image erosion function. The final disc segmentation was defined by the volumetric intersection where mean \pm two standard deviations of axial, circumferential, and radial strain values were located [Figure 29C].

Annulus fibrosus segmentation was performed dividing the disc radially into inner/outer AF, axially into inferior/middle/superior AF, and circumferentially into five AF regions (anterior = A, anterior-lateral = A-L, lateral = L, posterior-lateral = P-L, posterior = P). Regional average \pm standard deviation axial (E_{zz}), circumferential ($E_{\theta\theta}$), radial (E_{rr}), and in-plane shear ($E_{\theta\theta}$) strain for comparisons between the anatomic axial (middle vs. attachment region), circumferential (A, A-L, L, P-L, P) radial (inner vs. outer) direction. The segmented disc region [Figure 29C] was utilized to regionally segment the disc into inner and outer annulus. The outer contour was defined by tracing the discs projection into the x-y plane with its origin defined as the disc's centroid. The outer/inner annulus and inner annulus/nucleus pulposus boundaries were assumed to be approximate scaled-down versions of the discs outer contour. All three contours, outer AF, inner AF, and NP were assumed to not vary in the z-direction. Based on the known nucleus – annulus proportions (O'Connell, Vresilovic et al. 2007), the NP occupied 28% of the disc axial area and the outer/inner AF transition occurred halfway between the outer disc boundary and NP. Placement of the NP contour accounted for the natural offset within the disc by a 3% posterior translation from the discs centroid [Figure 37A]. The disc was then divided into thirds in the axial direction defining inferior, middle, and superior [Figure 37B] zones. Each AF zone was then divided into Anterior (A), Anterior-

Lateral (A-L), Lateral (L), Posterior-Lateral (P-L), and Posterior (P) (Costi, Stokes et al. 2007) regions excluding the lateral region furthest from the RF coil [Figure 37C].

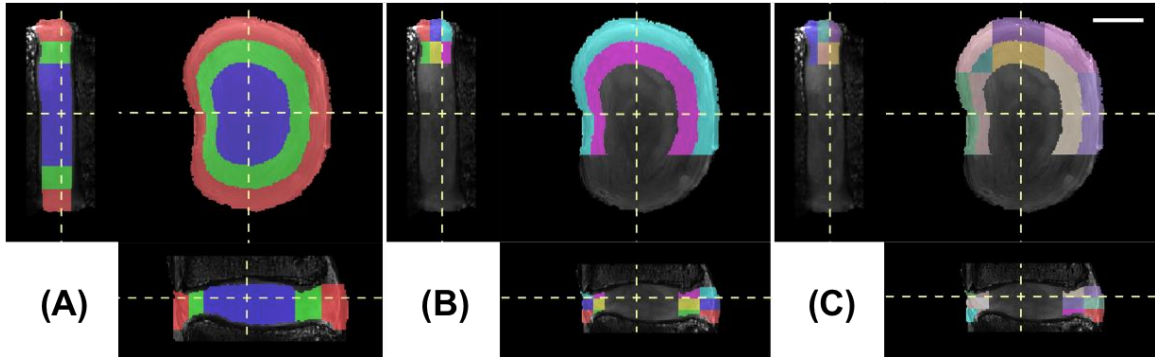


Figure 37: Representative segmentation process for defining disc regions: (A) Automatic NP (blue), inner AF (green), and outer AF (red), (B) Axial height division into superior, middle, and inferior disc regions, and (C) Subdivision into anterior: A, anterior-lateral: A-L, lateral: L, posterior-lateral: P-L, and posterior: P annulus within each axial height division. White scale bar = 1 cm.

Mean axial (E_{zz}), circumferential ($E_{\theta\theta}$), radial (E_{rr}), and shear ($E_{\theta r}$) disc strain

values were reported for each region and across the entire annulus [Figure 38].

Additionally, the location of peak mean strain values was identified.

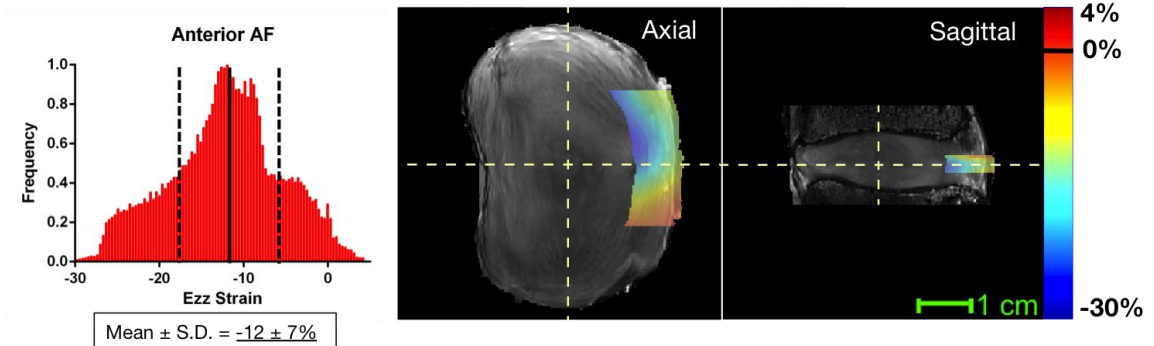


Figure 38: Representative middle third disc height anterior outer annulus axial strain histogram (left) and strain color map (right). Each region exhibited a normal strain distribution. Mean strain values (solid black line) were reported for each region. One standard deviation (dashed black line) is shown for reference.

Planned statistical comparisons were designed to test regional differences along the radial (inner vs. outer), circumferential (A vs. A-L vs. L vs. P-L vs. P), and axial (inferior vs. middle vs. superior) direction strain magnitudes for each disc's specific strain coordinate system E_{zz} , $E_{\theta\theta}$, E_{rr} , and $E_{\theta r}$ at the 5%, 10%, and 15% axial compressions. To simplify the number of potential comparisons, the entire inferior and superior AF was compared with a paired two-tailed t-test for E_{zz} , $E_{\theta\theta}$, E_{rr} , and $E_{\theta r}$ at each strain level for a total of 12 comparisons (adjusted p-value set significance at < 0.004). If the inferior and superior AF strain magnitudes are not found to be statistically different, these regions will be averaged in subsequent statistical analysis.

Regional variability in mean strain magnitude along the axial disc height (inferior, middle, and superior) was determined by a two-way ANOVA with repeated measures applied along the axial direction (middle and attachment region = average of inferior and superior) and circumferential direction (A, A-L, L, P-L, and P); a Bonferroni post-hoc correction was applied.

Radial and circumferential variability was determined by a two-way ANOVA with repeated measures along the radial (inner and outer AF) and circumferential direction (A, A-L, L, P-L, and P). Radial differences between the inner and outer AF within each circumferential region was analyzed with post-hoc comparisons with a Bonferroni correction factor. Circumferential variability between the A, A-L, L, P-L, and P within each radial region (inner/outer) was assessed with a post-hoc comparison using Tukey's test.

Each comparison (axial, radial, and circumferential) was made for each strain direction (E_{zz} , $E_{\theta\theta}$, E_{rr} , and $E_{\theta r}$) and level of compression (5%, 10%, and 15%) resulting

in 36 total comparisons. Significance for each comparison was adjusted according the prescribed post-hoc correction factor setting significance at $p \leq 0.05$ and trend at $0.05 \leq p \leq 0.10$.

8.3. Results

Qualitative visual strain patterns were consistent at all levels of axial compression. Axial compression resulted in predominantly negative E_{zz} and horizontal banding throughout the disc height. Peak negative axial strain occurred medially and small regions of tension located near the endplates [Figure 35A]. Circumferential strain exhibited values near zero at the bone-disc boundary, and positive peak values occurred in the posterior and lateral regions [Figure 35B]. Radial strain decreased from positive to near zero values out from the NP to the outer boundary of the AF [Figure 35C] with peak values in the posterior AF.

The superior and inferior annular strain regions were not found to be significantly different at each level of axial compression and strain direction ($p > 0.32$) [Figure 39]. These regions were subsequently averaged and labeled ‘attachment region’ for further analysis of regional variability.

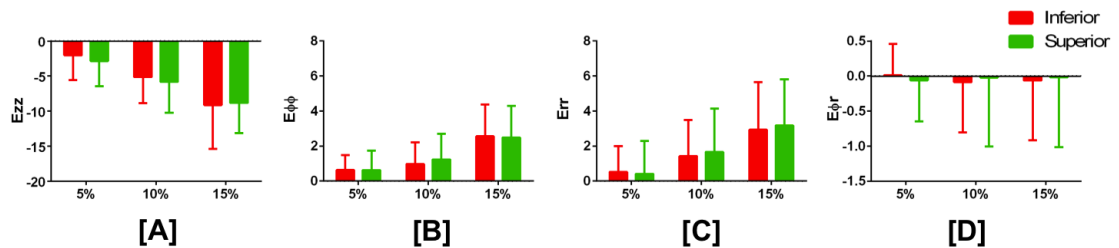


Figure 39: Reported regional (average \pm standard deviation) mean strain values for inferior (red) and superior (green) annulus fibrosus at 5%, 10%, and 15% axial compression for [A] – axial (E_{zz}), [B] – circumferential ($E_{\theta\theta}$), [C] – radial (E_{rr}), and [D] – in-plane shear ($E_{\theta r}$).

Annulus fibrosus strain in the principle strain (E_{zz} , $E_{\theta\theta}$, and E_{rr}) increased in magnitude with applied axial compression for all regions throughout the disc while in-

plane shear strain ($E_{\theta r}$) remained relatively constant. Global AF strain values are reported in Table 7, sub-region values and all statistical comparisons for E_{zz} , $E_{\theta\theta}$, E_{rr} , and $E_{\theta r}$ can be found in Table 8, Table 9, Table 10, and Table 11 respectively.

Axial Compression	Strain Direction			
	E_{zz}	$E_{\theta\theta}$	E_{rr}	$E_{\theta r}$
5%	$-2.49 \pm 4.93\%$	$0.72 \pm 1.08\%$	$0.39 \pm 1.80\%$	$-0.0087 \pm 0.48\%$
10%	$-6.39 \pm 5.63\%$	$1.29 \pm 1.49\%$	$1.48 \pm 2.32\%$	$-0.061 \pm 0.85\%$
15%	$-11.28 \pm 5.91\%$	$2.84 \pm 1.99\%$	$2.88 \pm 2.89\%$	$-0.017 \pm 0.93\%$

Table 7: Global annulus fibrosus strain values (average \pm standard deviation).

Peak reported mean AF strain values were located predominantly in posterior and lateral regions for each strain direction. Extreme axial strain values occurred largely within the inner annulus at the middle region disc height experiencing maximum negative (-28.42%) and peak positive (19.33%) values. Circumferential strain maximum strain values occurred within the inner annulus primarily at the attachment region exhibiting peak negative and positive values as follows -3.19% and 9.65% . Peak radial strain arose at the attachment region within the outer annulus undergoing peak negative values of -6.73% and positive values of 10.31% . In-plane shear strain peak values were more concentrated within the inner posterior-lateral annulus along the attachment region achieving peak negative and positive strain values of -3.91% and 3.16% .

For each statistical comparison analyzing variability in the axial, radial, and circumferential direction minimal regional variability occurred under 5% and 10% axial compression. Each subsequent results section will discuss regional differences under 15% axial compression, all statistical comparison results can be found in Table 8: E_{zz} , Table 9: $E_{\theta\theta}$, Table 10: E_{rr} , and Table 11: $E_{\theta r}$.

8.3.1. Axial Disc Height Variance

Axial strain (E_{zz}) varied between the middle and attachment region disc height in both the inner and outer AF within circumferential AF regions at 15% axial compression ($p < 0.016$) with inner AF regions exhibiting interaction effects ($p = 0.0694$). Larger E_{zz} strain magnitudes occurred along the middle disc height in the anterior-lateral and lateral AF ($p < 0.014$) for both the inner and outer AF [Figure 40A]. The outer AF displayed the same trends in all regions except the anterior AF ($p < 0.014$) [Figure 40B].

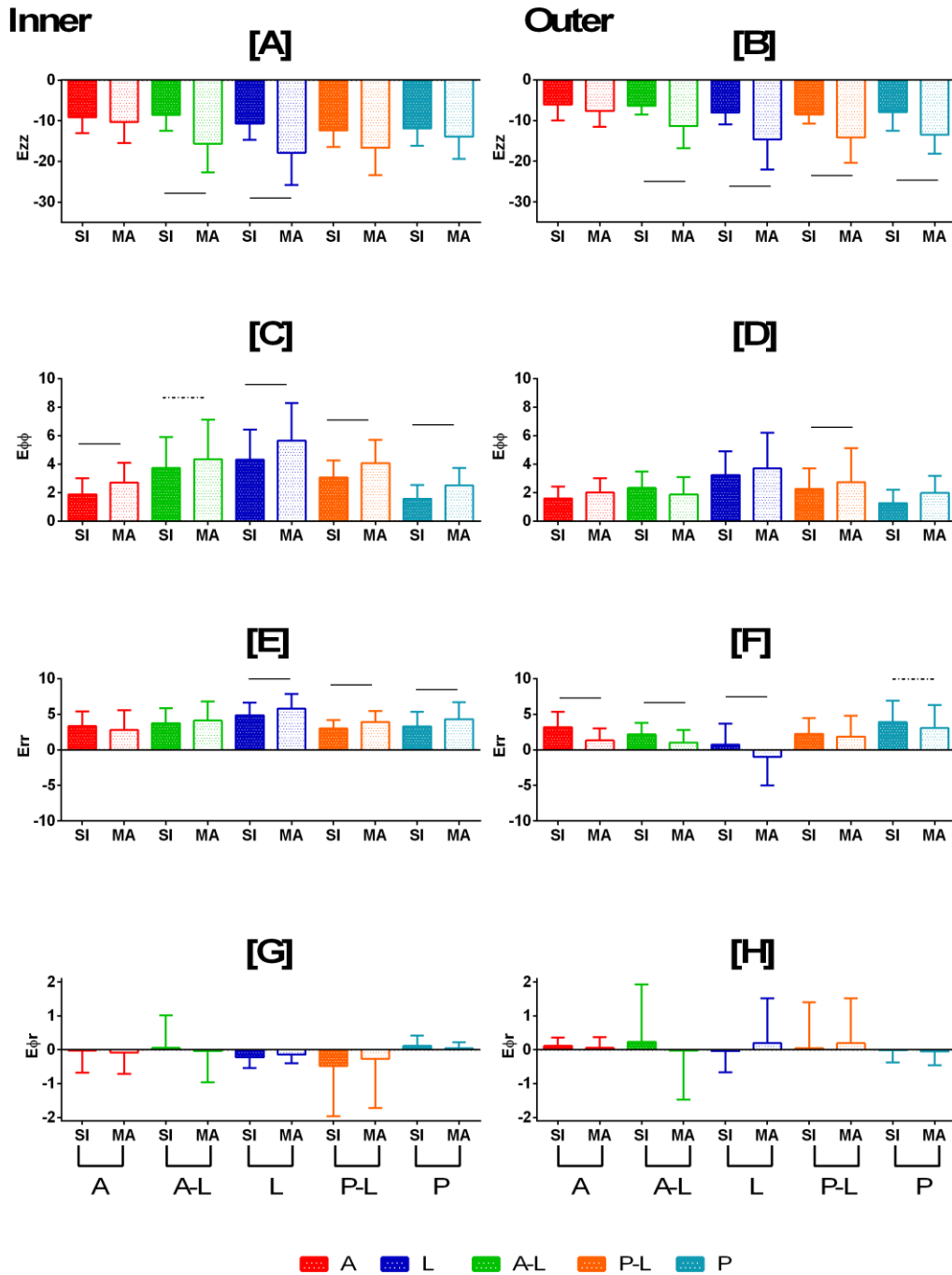


Figure 40: Regional strain bar charts (mean \pm standard deviation) comparing the inner (left-hand side) and outer (right-hand side) attachment region (solid) vs. middle (dotted) AF regions under 15% axial compression for axial [A / B], circumferential [C / D], radial [E / F], and in-plane shear [G / H] at 15% axial compression. Regions: anterior (A – red), anterior-lateral (A-L – green), lateral (L – blue), posterior-lateral (P-L – orange), and posterior (P – turquoise) annulus. Significance: solid line $p \leq 0.05$. Trend: dashed line $0.05 \leq p \leq 0.10$.

Overall the disc experienced relatively uniform circumferential strain ($E_{\theta\theta}$) along the middle region disc height for smaller degrees of axial compression [Table 9]. At 15% compression $E_{\theta\theta}$ showed significance in both the inner and outer AF regions ($p < 0.05$) and interaction effects were also observed within the outer AF ($p = 0.021$). All middle region disc inner annular regions [Figure 40C] were larger than the attachment region ($p < 0.08$) and larger within the posterior-lateral AF ($p = 0.036$) for the outer AF [Figure 40D].

Radial strain (E_{rr}) varied within the outer AF ($p < 0.037$) along the axial disc height at 10% and 15% compression (Table 10). Both the inner and outer AF ($p < 0.022$) radial strain varied along axial disc height at 15% axial compression and significant interaction between groups ($p < 0.042$). Middle disc height strain within the outer AF E_{rr} was significantly smaller than the attachment region disc height for all regions except the posterior-lateral [Figure 40F] at 15% axial compression. However, the middle region inner lateral, posterior-lateral, and posterior AF E_{rr} was greater than the attachment region disc height ($p < 0.008$) at 15% axial compression [Figure 40E]. No significance was found between regions for in-plane shear strain [Figure 40G/H]

8.3.2. Circumferential Regional Variance

Along the middle and attachment region disc height under 15% axial compression, axial strain (E_{zz}) varied between circumferential AF regions ($p < 0.01$) with interaction effect ($p < 0.02$). Within the outer and inner annulus middle disc height, the anterior AF E_{zz} exhibited smaller strains than all other regions ($p < 0.002$) and anterior-lateral AF smaller than lateral AF ($p < 0.034$) [Figure 41A]. The outer anterior-lateral AF

was smaller than the posterior-lateral AF ($p < 0.052$) [Figure 41A]. Within the attachment region disc height significance occurred at both 10% and 15% ($p < 0.07$) compression with no interaction effects. Under 10% axial compression the anterior AF E_{zz} strain was smaller than the lateral and posterior-lateral regions [Table 8]. Anterior AF E_{zz} strain was smaller than the posterior-lateral and posterior regions within the outer and inner AF for 15% axial compression ($p < 0.076$) [Figure 41B]. Within the inner annulus the anterior-lateral was significantly different than the lateral, posterior-lateral, and posterior ($p < 0.019$) at 15% compression [Figure 41B].

Circumferential strain ($E_{\theta\theta}$) varied between AF regions at 10% and 15% axial along both the middle ($p < 0.036$) and attachment region ($p < 0.0001$) disc heights with interaction effects ($p < 0.095$). Within the middle disc-height the lateral AF $E_{\theta\theta}$ experienced more circumferential strain in the inner and outer AF than the anterior and anterior-lateral AF ($p < 0.040$) [Table 9, Figure 41C] and the posterior AF within the inner AF. The inner anterior AF experienced less $E_{\theta\theta}$ than all regions other than posterior AF ($p < 0.040$) [Table 9, Figure 41C]. For the attachment region disc height annulus within the inner posterior-lateral region experienced higher $E_{\theta\theta}$ strain magnitudes than all other areas at 10% ($p < 0.0003$) [Table 9]. At 15% compression the attachment region inner and outer lateral AF exhibited higher $E_{\theta\theta}$ strain magnitudes than the anterior, posterior-lateral, and posterior regions ($p < 0.013$) [Figure 41D].

Middle

Attachment Region

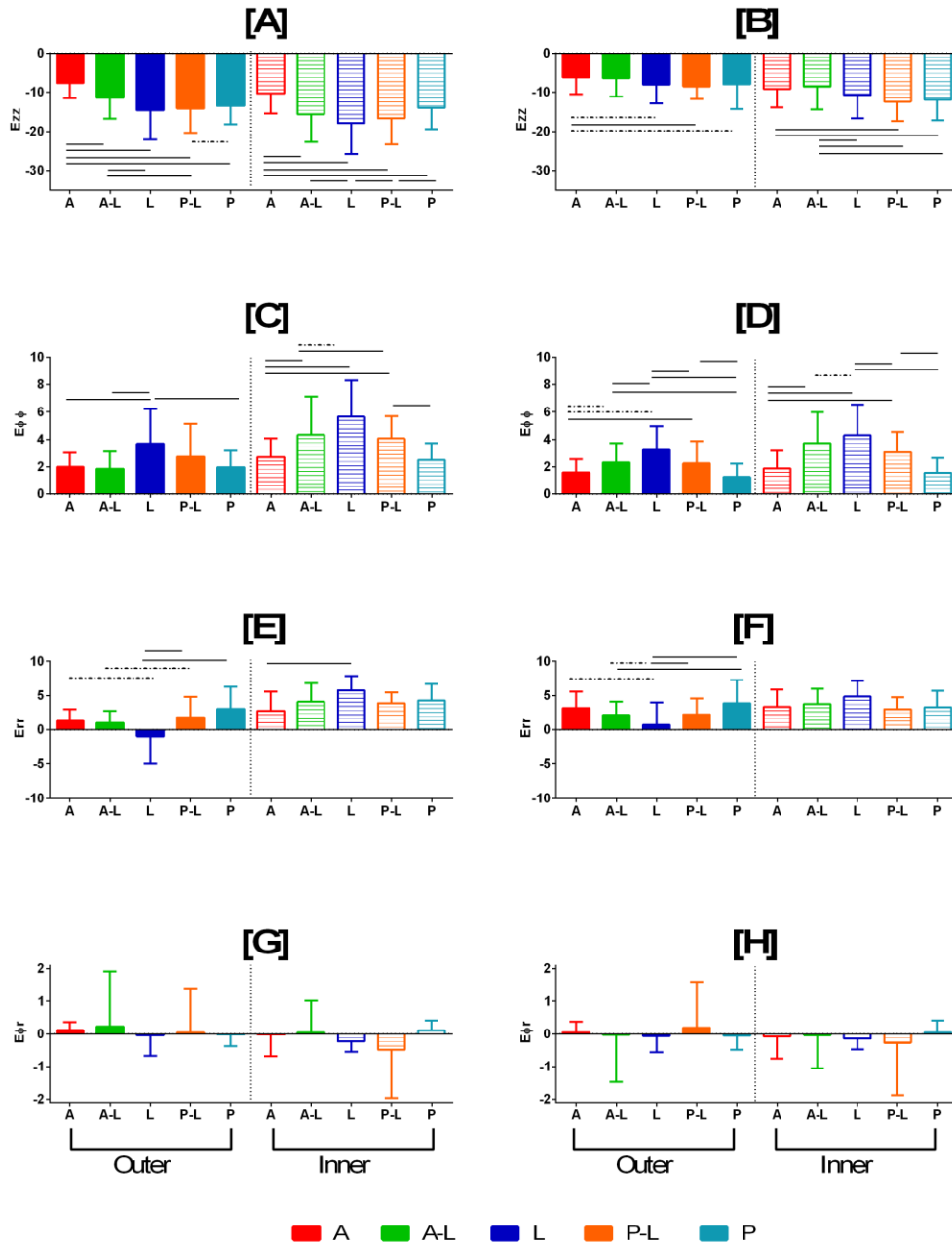


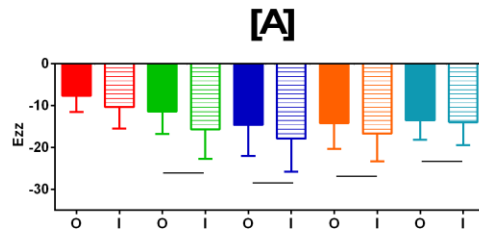
Figure 41: Regional strain bar charts (mean ± standard deviation) comparing the circumferential positions (A, A-L, L, P-L, and P) along the middle [left-hand side] and attachment region [right-hand side] disc height within the outer (solid) and inner (dashed) AF regions under 15% axial compression for axial [A / B], circumferential [C / D], radial [E / F], and in-plane shear [G / H] at 15% axial compression. Regions: anterior (A – red), anterior-lateral (A-L – green), lateral (L – blue), posterior-lateral (P-L – orange), and posterior (P – turquoise) annulus. Significance: solid line p ≤ 0.05. Trend: dashed line 0.05 ≤ p ≤ 0.10.

Regional analysis of variance illustrated significance only at 15% for both middle region ($p = 0.006$) and attachment region ($p = 0.026$) regions for radial strain (E_{rr}). Along the middle disc height of inner AF, the anterior E_{rr} was significantly smaller than the lateral AF ($p = 0.006$). The outer posterior AF E_{rr} was smaller than both the anterior-lateral and posterior-lateral AF ($p < 0.024$) at the attachment region axial disc height. The inner AF E_{rr} was more uniform along the attachment region. No significance was found between regions for in-plane shear strain [Figure 41G/H]

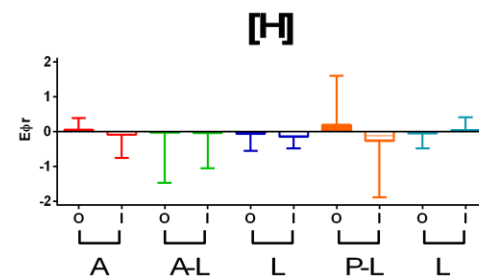
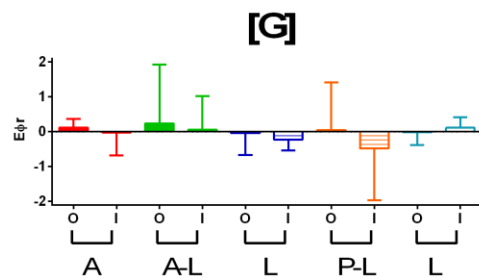
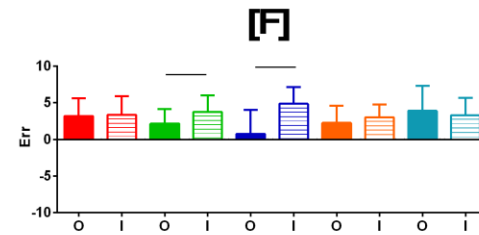
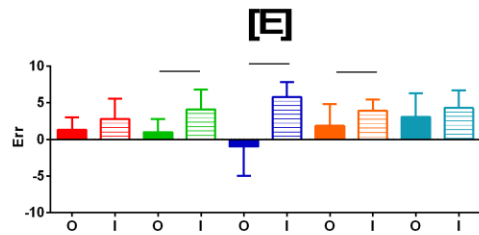
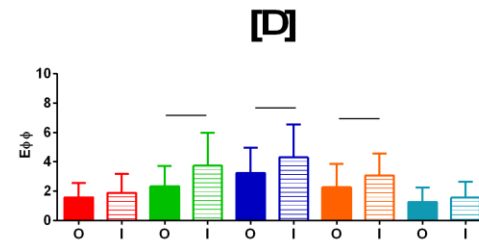
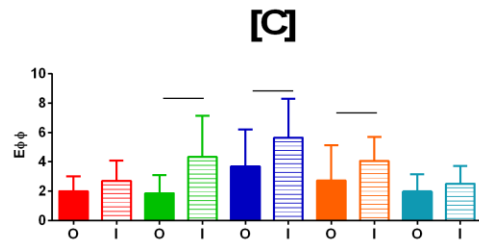
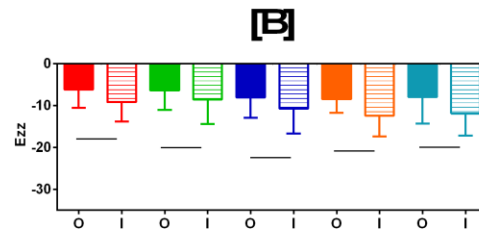
8.3.3. Inner vs. Outer Annulus

Overall the inner annulus (AF) exhibited higher strain magnitudes than the outer AF for the three principle strain components. Along the middle region disc height no significance was found in the radial direction between inner and outer AF axial strain (E_{zz}) at 5% and 10% axial compression. At 15% axial compression the middle region inner AF E_{zz} was higher compared to the outer AF strain (global inner/outer AF $E_{zz} = -14.91 \pm 6.74\% / -12.26 \pm 5.98\%$), for all regions except the anterior AF [Figure 42A] ($p < 0.008$). Within the attachment region the inner AF varied from the outer AF at both 10% and 15% ($p < 0.07$) axial compression with no interaction effects. The attachment region inner AF E_{zz} strain was greater in magnitude than outer AF (global inner/outer AF $E_{zz} = -10.55 \pm 5.45\% / -7.41 \pm 5.33\%$) for all regions at 15% [Figure 42B] ($p < 0.019$); except at 10%, the anterior lateral region exhibited a trend [Table 8] ($p < 0.063$).

Middle



Attachment Region



■ A ■ A-L ■ L ■ P-L ■ P

Figure 42: Regional strain bar charts (mean \pm standard deviation) comparing the middle [left-hand side] and attachment region [right-hand side] disc height outer (solid) and inner (dashed) AF regions under 15% axial compression for axial [A / B], circumferential [C / D], radial [E / F], and in-plane shear [G / H] at 15% axial compression. Regions: anterior (A – red), anterior-lateral (A-L – green), lateral (L – blue), posterior-lateral (P-L – orange), and posterior (P – turquoise) annulus. Significance: solid line $p \leq 0.05$. Trend: dashed line $0.05 \leq p \leq 0.10$.

Circumferential strain ($E_{\theta\theta}$) between the inner and outer AF along the middle disc height region was significant at 10% and 15% axial compression ($p < 0.018$). The inner anterior-lateral and posterior-lateral AF experienced more strain than the outer AF at 10% [Table 9] in addition to the lateral AF at 15% axial compression [Figure 42C] ($p < 0.032$). Circumferential strain in the attachment region axial disc height depicted significance between the inner and outer AF ($p < 0.053$). Interaction effects occurred ($p < 0.09$) at 10% and 15% axial compression. The inner AF had higher strain values than the outer AF in the posterior ($p = 0.003$) at 10% [Table 9] and in all lateral regions ($p < 0.021$) at 15% [Figure 42D] axial compression.

Radial strain (E_{rr}) was significant at 15% axial compression for both middle region ($p = 0.006$) and attachment region ($p = 0.026$) regions between the inner and outer annulus. The inner AF had higher strain magnitudes than the outer AF along the middle and attachment region disc height in the anterior lateral and lateral AF ($p < 0.019$) [Figure 42E/F]. The lateral region had the highest overall variability between inner and outer AF across the entire disc height. No significance was found between regions for in-plane shear strain [Figure 42G/H].

Discussion

Internal intervertebral disc (IVD) regional axial (E_{zz}), circumferential ($E_{\theta\theta}$), radial (E_{rr}), and in-plane shear ($E_{\theta r}$) strain properties for moderately degenerate (Pfirrmann, Metzdorf et al. 2001) discs (grade 3) was presented in this chapter. Comparisons were made along the primary axis of the spine, radially assessing inner vs. outer annulus (AF), circumferentially by five divisions (anterior, anterior-lateral, lateral, posterior-lateral, and lateral), and axially along the disc height (middle vs. attachment region). The AF anisotropic mechanical properties (Skaggs, Weidenbaum et al. 1994, Acaroglu, Iatridis et al. 1995, Ebara, Iatridis et al. 1996, Iatridis, Kumar et al. 1999, Elliott and Setton 2000, Fujita, Wagner et al. 2000, Elliott and Setton 2001, Perie, Maclean et al. 2006, O'Connell, Guerin et al. 2009, Jacobs, Smith et al. 2011, Cortes and Elliott 2012, Cortes, Han et al. 2013), regional structural and composition heterogeneity (Eyre and Muir 1976, Eyre and Muir 1977, Hickey and Hukins 1980, Marchand and Ahmed 1990, Tsuji, Hirano et al. 1993, Buckwalter 1995), and complex disc boundary conditions make no single ex-vivo test appropriate to quantify the AF mechanical properties. This work enables regional, non-invasive IVD strain measurement under incremental amounts of axial compression through high-resolution isotropic image acquisition ($300\mu\text{m}/\text{pixel}$) and image registration. As only moderately degenerate discs were tested, the proposed segmentation techniques are valid under the assumption that there is no presence of local bulging or herniation. Adjustments to this approach will be made for future studies testing degeneration where disc collapse has occurred. The division between the outer/inner AF and inner AF/ nucleus pulposus borders was kept constant along the axial disc height;

additional anatomical studies are required in-order to determine how these boundary proportions might vary with axial disc height. Under small strains (i.e. 5%) no regional statistical variances were found, and increased axial compression lead to differentiation between regions of the disc. The AF structure, composition, and regional heterogeneity within the IVD resulted in complex annular strain patterns under axial compression.

Variability in axial disc height due to vertebral body curvature caused regional strain variation throughout the disc under uniform axial compression. As a result of shorter disc height within inner AF and weaker material properties (Skaggs, Weidenbaum et al. 1994, Fujita, Duncan et al. 1997, Fujita, Wagner et al. 2000) resulted higher magnitudes of E_{zz} strain. Similarly, the large disc height within the anterior AF and stiffer material properties (Skaggs, Weidenbaum et al. 1994, Fujita, Duncan et al. 1997, Fujita, Wagner et al. 2000) created smaller strain magnitudes than the rest of the disc. As the disc undergoes compression, AF fibers attached to the vertebral body go into tension, producing decreased amounts of compression within the superior and inferior regions. This results in horizontal banding throughout the disc height with peak negative strain occurring medially. Middle region AF segmentations from Chapter 7 primarily align with the outer AF in this chapter, previous strain values are lower by ~1-2% as a result of partial inclusion of the inner AF. Outer AF strain values along the middle region disc height under 10% and 15% axial compression ($-6.90 \pm 6.18\%$ and $-12.26\% \pm 5.98\%$) correspond to previously published surface strains -10.4% under 500N axial load (Heuer, Schmidt et al. 2008, Heuer, Schmidt et al. 2008).

Circumferential strain was relatively constant throughout the disc, however regional differentiation was present under 15% axial compression. The lateral AF

exhibited 0.5X larger strains than the anterior and posterior regions. Similar to axial strain, geometry played a large role within the inner AF as it experienced more strain than outer AF. The smaller circumference of the inner AF proportionally displaced more than the larger outer AF under uniform axial compression. Compared to the inner AF, outer AF tensile modulus is greater, which could contribute to limiting deformation (Shah, Hampson et al. 1978, Stokes 1987). Additionally, AF fiber attachment to the vertebral bodies yielded smaller circumferential strain at these boundaries compared to the middle region disc height. The outer posterior AF at the middle region was 0.36X greater than the attachment region disc height. Along the attachment region the inner posterior-lateral AF underwent 0.51X more strain than all other regions under 10% axial compression. Large strains occurring in the lateral and posterior-lateral regions are indicative of regional sectors of weakness within the disc, where failure might occur. Experimental and clinical studies have shown these areas as weak points within the disc, often resulting in herniation of nuclear material through the AF (Resnick and Niwayama 1978, Brinckmann 1986, Yorimitsu, Chiba et al. 2001, Martin, Boxell et al. 2002, Weinstein, Lurie et al. 2006, Mariconda, Galasso et al. 2010). Outer AF circumferential strain was ~0.18% less than values found in Chapter 7 as a result of partial inclusion of the inner AF. Circumferential strains found at the middle region disc height within the outer AF ($3.16 \pm 2.18\%$) under 15% axial compression correspond to previously measured surface strain -3.4% (Heuer, Schmidt et al. 2008, Heuer, Schmidt et al. 2008).

Similar to axial and circumferential strain, regional radial strain differentiation within the AF began to be more apparent under 15% axial compression. Within each region of the AF, radial strain had a wide range of values with standard deviation being

greater than the reported average. Peak negative values occurred (-4.95% to -6.73%) in the lateral AF across the entire disc height for all levels of axial compression.

Additionally, the inner lateral AF exhibited the highest average radial strain values compared to rest of the AF. Within the lateral regions, the inner AF experience more radial strain than the outer AF. The more deformable inner AF enables even distribution of hoop stresses to dissipate energy uniformly throughout the disc (Best, Guilak et al. 1994). Peak positive radial strain occurred within the outer posterior AF along the bone-disc boundary (4.87% to 10.31%), however this region had the smallest overall average radial strain. The inclusion of inner AF in previous segmentations resulted in middle region outer AF values to be 0.55X smaller than values reported from Chapter 7. Large radial strain standard deviations and peak values occurring within the lateral and posterior regions of the AF are indicative of areas of potential failure leading to tears within the disc. It is well documented clinically (Resnick and Niwayama 1978, Brinckmann 1986, Yorimitsu, Chiba et al. 2001, Martin, Boxell et al. 2002) that the posterior-lateral region of the disc is a structural weak point based on increased interruptions in lamellar structure, lamellar thickness, and disc geometry (Marchand and Ahmed 1990, Tsuji, Hirano et al. 1993). High posterior E_r may be due to nucleus placement closer to the posterior annulus and thinner lamellae creating more posterior strain as the nucleus bulges outwards.

Disc geometry contributes largely to the observed regional differences in disc strain, particularly in axial and circumferential strain. The large differences regional radial strain magnitude may contribute to separation of the AF lamellae potentially leading to annular tears. Overall, the inner AF experienced more strain than the outer AF.

This is a result of the weaker inner AF being constrained between the stiff outer AF and pressurized NP. The outer annulus has been shown to be more anisotropic than the inner annulus, potentially as a result of differences in fiber angle 60° vs. 45° inducing similar inner AF tensile strain leading to equal directional moduli (Ebara, Iatridis et al. 1996, Fujita, Duncan et al. 1997, Fujita, Wagner et al. 2000). Additionally, in the radial direction there are more drastic changes in biochemistry exhibiting changes in the ratio between type I and type II collagen, collagen, water, and proteoglycan content.

Work within this chapter establishes techniques to non-invasively study 3D internal intervertebral disc strain. The regional internal strain variability was characterized under incremental amounts of axial compression. Overall disc geometry, subcomponent architecture, boundary conditions, and biochemical composition are potential contributing factors to internal strain variability. Future studies will explore the effects various loading modalities, degeneration, and clinical treatments on the internal strain distributions within the intervertebral disc.

Applied Compression	Axial/Radial Position		Circumferential Position					Regional Variance		
			A	A-L	L	P-L	P	Axial	Circumferential	Radial
5%	M	O	-0.21± 2.22	-2.02± 4.76	-4.38± 6.21	-4.31± 5.63	-3.26± 6.27	NS	NS	NS
		I	-0.01± 5.25	-0.49± 8.52	-2.66± 7.26	-4.87± 6.80	-3.19± 8.21	NS	NS	
	S/I	O	-1.16± 2.66	-1.74± 2.28	-2.37± 4.12	-2.43± 2.91	-2.40± 2.73		NS	NS
		I	-1.66± 4.94	-2.89± 3.32	-2.80± 4.00	-3.33± 4.20	-3.62± 4.36		NS	
10%	M	O	-4.78± 4.55	-5.61± 5.00	-7.85± 5.18	-8.52± 5.18	-7.75± 9.02	NS	NS	NS
		I	-5.94± 6.81	-7.30± 6.89	-8.22± 6.86	-9.39± 9.03	-7.57± 11.50	NS	NS	
	S/I	O	-2.77± 3.57	-4.30± 3.54	-5.36± 2.90	-4.82± 3.64	-5.22± 3.28		A vs. L*, P-L*, P*	A*, A-Lt, P-L*, P*
		I	-4.71± 4.95	-5.95± 4.78	-6.89± 3.78	-7.02± 4.60	-7.73± 3.84		A vs. L*, P-L*, P*	
15%	M	O	-7.65± 3.88	- 11.39± 5.37	- 14.62± 7.45	- 14.16± 6.21	- 13.51± 4.68	A-L*, L*, P-L*, P*	A vs. A-L*, L*, P-L*, P*, A-L vs. L*, P-L*, Pt	A-L*, L*, P-L*, P*
		I	- 10.34± 5.11	- 15.64± 7.03	- 17.89± 7.90	- 16.70± 6.61	- 13.96± 5.44	A-L*, L*	A vs. A-L*, L*, P-L*, P*, L vs. A-L*, P*, P-L vs. P*	
	S/I	O	-6.13± 4.41	-6.40± 4.66	-8.06± 4.81	-8.51± 3.25	-7.95± 6.34		A vs. Lt, P-L*, Pt, A-L vs. P-L*	A*, A-L*, L*, P-L*, P*
		I	-9.18± 4.65	-8.52± 5.88	- 10.71± 5.95	- 12.42± 4.96	- 11.92± 5.20		A vs. P-L*, P*, A-L vs. L*, P-L*, P*	

Table 8: Results for regional axial (E_{zz}) strain values (mean \pm standard deviation) under 5%, 10%, and 15% axial compression. Region definitions: axial disc height (M = middle region, S/I = attachment region), radial position (O = outer annulus, I = inner annulus), and circumferential position (A = anterior, A-L = anterior-lateral, L = lateral, P-L = posterior-lateral, P = posterior). Three comparisons were made along each axis to assess regional variance: 1. Axial column analyzed superior/inferior vs. middle region disc height within the outer and inner annulus for each circumferential position (A, A-L, L, P-L, and P). Circumferential column analyzed the differences between (A, A-L, L, P-L, P) within the outer and inner annulus for each axial disc-height position, and 3. Radial column analyzed inner vs. outer annulus within (A, A-L, L, P-L, P) for each axial disc-height position. Significance (* = $p < 0.05$) and trend ($t = 0.05 < p < 0.10$)

Applied Compression	Axial/Radial Position		Circumferential Position					Regional Variance		
			A	A-L	L	P-L	P	Axial	Circumferential	Radial
5%	M	O	0.46± 0.51	0.09± 1.07	0.92± 1.03	0.67± 1.52	0.74± 0.32	NS	NS	NS
		I	0.83± 0.66	0.46± 1.81	1.73± 1.19	1.26± 1.74	0.98± 0.36	NS	NS	
	S/I	O	0.33± 0.51	0.38± 1.02	0.74± 0.87	0.61± 1.26	0.53± 0.33		NS	NS
		I	0.59± 0.63	0.26± 1.45	1.10± 1.07	0.97± 1.42	0.78± 0.55		NS	
10%	M	O	1.12± 1.67	0.50± 0.95	1.08± 0.77	1.59± 1.65	1.27± 1.19	NS	A-L vs. P-Lt, Pt	A-L*, P-L*
		I	1.49± 2.00	1.40± 1.99	1.56± 1.66	2.98± 2.03	1.71± 1.23	NS	P-L vs. A*, A-L*, L*, P*	
	S/I	O	0.93± 1.40	0.97± 1.02	0.87± 0.74	1.25± 1.09	0.78± 0.84		NS	P*
		I	1.01± 1.69	1.19± 2.20	0.86± 1.38	2.08± 1.55	1.06± 0.90		P-L vs. A*, A-L*, L*, P*	
15%	M	O	2.01± 1.02	1.86± 1.24	3.70± 2.52	2.74± 2.39	1.98± 1.19	P-L*	L vs. A*, A-L*, P*	A-L*, L*, P-L*
		I	2.70± 1.39	4.34± 2.80	5.65± 2.65	4.07± 1.63	2.51± 1.21	A*, A-Lt, L*, P-L*, P*	A-L vs. A*, P*, P-L vs. A*, L*, P*, L vs. A*, A-Lt	
	S/I	O	1.58± 0.98	2.33± 1.39	3.23± 1.72	2.26± 1.60	1.26± 0.98		A vs. A-Lt, L*, P-Lt P vs. A-L*, L*, P-L* L vs. A-L*, P-L*	A-L*, L*, P-L*
		I	1.88± 1.29	3.73± 2.26	4.30± 2.24	3.07± 1.49	1.57± 1.07		A vs. A-L*, L*, P-L* L vs. P-L P vs. A-L*, L*, P-L*	

Table 9: Results for regional circumferential ($E_{\phi\phi}$) strain values (mean \pm standard deviation) under 5%, 10%, and 15% axial compression. Region definitions: axial disc height (M = middle region, S/I = attachment region), radial position (O = outer annulus, I = inner annulus), and circumferential position (A = anterior, A-L = anterior-lateral, L = lateral, P-L = posterior-lateral, P = posterior). Three comparisons were made along each axis to assess regional variance: 1. Axial column analyzed superior/interior vs. middle region disc height within the outer and inner annulus for each circumferential position (A, A-L, L, P-L, and P). Circumferential column analyzed the differences between (A, A-L, L, P-L, P) within the outer and inner annulus for each axial disc-height position, and 3. Radial column analyzed inner vs. outer annulus within (A, A-L, L, P-L, P) for each axial disc-height position. Significance (* = $p < 0.05$) and trend ($t = 0.05 < p < 0.10$)

Applied Compression	Axial/Radial Position		Circumferential Position					Regional Variance		
			A	A-L	L	P-L	P	Axial	Circumferential	Radial
5%	M	O	0.42± 1.51	-0.02± 1.12	-0.73± 2.79	0.05± 1.50	0.07± 2.65	NS	NS	NS
		I	0.37± 1.21	0.46± 1.81	0.95± 2.31	0.81± 1.55	0.83± 2.24	NS	NS	
	S/I	O	1.16± 1.40	0.49± 1.31	-0.03± 2.02	0.28± 1.28	0.23± 2.21		NS	NS
		I	0.42± 1.47	0.32± 1.50	0.58± 2.39	0.71± 1.33	0.42± 1.74		NS	
10%	M	O	1.26± 1.88	0.27± 1.19	-0.33± 3.52	1.15± 2.04	2.13± 2.96	A*,A-L*,L*	NS	NS
		I	1.12± 2.24	1.48± 1.84	1.97± 2.33	2.34± 1.90	2.77± 2.51	NS	NS	
	S/I	O	2.27± 1.91	1.09± 1.22	0.84± 3.09	1.32± 1.55	2.35± 3.17		NS	NS
		I	1.48± 2.25	1.25± 2.05	1.53± 2.79	1.57± 1.57	1.79± 2.31		NS	
15%	M	O	1.32± 1.69	0.99± 1.80	-0.97± 4.00	1.86± 2.95	3.06± 3.26	A*,A-L*,L*,Pt	L vs. At, P-Lt, P*	A-L*, L*, P-Lt
		I	2.78± 2.78	4.10± 2.68	5.77± 2.07	3.91± 1.58	4.29± 2.41	L*,P-L*,P*	A vs. L*	
	S/I	O	3.18± 2.43	2.16± 1.97	0.73± 3.28	2.25± 2.34	3.89± 3.40		L vs. A*, A-Lt, P-L*, P* P vs. A-L*, P-L*	A-L*, L*
		I	3.35± 2.52	3.75± 2.24	4.86± 2.28	3.03± 1.71	3.31± 2.38		NS	

Table 10: Results for regional radial (E_{rr}) strain values (mean \pm standard deviation) under 5%, 10%, and 15% axial compression. Region definitions: axial disc height (M = middle region, S/I = attachment region), radial position (O = outer annulus, I = inner annulus), and circumferential position (A = anterior, A-L = anterior-lateral, L = lateral, P-L = posterior-lateral, P = posterior). Three comparisons were made along each axis to assess regional variance: 1. Axial column analyzed superior/posterior vs. middle region disc height within the outer and inner annulus for each circumferential position (A, A-L, L, P-L, and P). Circumferential column analyzed the differences between (A, A-L, L, P-L, P) within the outer and inner annulus for each axial disc-height position, and 3. Radial column analyzed inner vs. outer annulus within (A, A-L, L, P-L, P) for each axial disc-height position. Significance (* = $p < 0.05$) and trend ($t = 0.05 < p < 0.10$).

Applied Compression	Axial/Radial Position		Circumferential Position					Regional Variance		
			A	A-L	L	P-L	P	Axial	Circumferential	Radial
5%	M	O	-0.007± 0.33	-0.004± 0.82	-0.01± 0.33	-0.03± 0.58	-0.11± 0.17	NS	NS	NS
		I	-0.17± 0.67	0.10± 0.71	0.13± 0.30	0.05± 0.72	-0.13± 0.31	NS	NS	
	S/I	O	-0.02± 0.25	0.07± 0.39	-0.07± 0.61	-0.15± 0.39	-0.007± 0.254		NS	NS
		I	-0.18± 0.51	0.03± 0.43	0.03± 0.32	-0.03± 0.31	0.07± 0.21		NS	
10%	M	O	-0.05± 0.18	0.05± 1.50	0.10± 0.30	-0.14± 1.67	-0.02± 0.43	NS	NS	NS
		I	-0.18± 0.46	-0.03± 0.89	0.06± 0.47	-0.25± 1.63	0.03± 0.20	NS	NS	
	S/I	O	-0.06± 0.10	-0.05± 0.47	-0.10± 0.95	-0.07± 0.72	0.07± 0.27		NS	NS
		I	-0.24± 0.42	-0.23± 0.62	-0.23± 0.48	-0.07± 0.39	0.05± 0.27		NS	
15%	M	O	0.11± 0.25	0.23± 1.69	-0.04± 0.63	0.04± 1.36	-0.02± 0.36	NS	NS	NS
		I	-0.02± 0.66	0.05± 0.97	-0.23± 0.32	-0.48± 1.48	0.11± 0.31	NS	NS	
	S/I	O	0.05± 0.32	0.001± 0.79	-0.03± 1.44	-0.09± 0.95	-0.06± 0.47		NS	NS
		I	-0.08± 0.64	-0.09± 0.83	-0.04± 0.92	-0.09± 0.46	-0.14± 0.26		NS	

Table 11: Results for regional radial ($E_{\phi r}$) strain values (mean \pm standard deviation) under 5%, 10%, and 15% axial compression. Region definitions: axial disc height (M = middle region, S/I = attachment region), radial position (O = outer annulus, I = inner annulus), and circumferential position (A = anterior, A-L = anterior-lateral, L = lateral, P-L = posterior-lateral, P = posterior). Three comparisons were made along each axis to assess regional variance: 1. Axial column analyzed superior/inferior vs. middle region disc height within the outer and inner annulus for each circumferential position (A, A-L, L, P-L, and P). Circumferential column analyzed the differences between (A, A-L, L, P-L, P) within the outer and inner annulus for each axial disc-height position, and 3. Radial column analyzed inner vs. outer annulus within (A, A-L, L, P-L, P) for each axial disc-height position. Significance (* = $p < 0.05$) and trend ($\dagger = 0.05 < p < 0.10$).

CHAPTER 9 **Conclusion and Future Directions**

The work presented within this thesis developed and validated methods to non-invasively in three dimensions visualize and quantify intervertebral disc (IVD) substructure geometry and track internal deformations for intact human discs under axial compression. The role of the IVD is to support load, permit motion, and dissipate energy in the spine. Resultant techniques and measurements established in this thesis will make significant contributions towards the study of disc function and degeneration, design criterion for functional tissue engineered discs, and to develop and evaluate surgical procedures and implants. Experimental internal strain measurements from this work will provide valuable data for disc finite element model validation, which to date has been limited to overall disc height deformation (Shirazi-Adl, Shrivastava et al. 1984, Goel, Monroe et al. 1995, Argoubi and Shirazi-Adl 1996, Fagan, Julian et al. 2002).

This thesis presents some of the first high-resolution disc substructure visualization and tissue specific MRI parameters of the IVD. As a result of the discs highly heterogeneous structural organization and biochemical composition (Lyons, Eisenstein et al. 1981, Bernick and Cailliet 1982, Pearce, Grimmer et al. 1987, Marchand and Ahmed 1990, Buckwalter, Mow et al. 2000) visualizing its substructures with a single MR imaging sequence proved challenging. Disc MRI tissue specific parameters (T1, T2, T2*, and T1 ρ) are well established for clinical grade scanners at 1.5T and 3.0T (Blumenkrantz, Zuo et al. , Welsch, Trattnig et al. , Pfirrmann, Metzdorf et al. 2001, Blumenkrantz, Li et al. 2006, Johannessen, Auerbach et al. 2006, Helms, Dathe et al. 2008, Hoppe, Quirbach et al. 2012, Lotz, Haughton et al. 2012, Antoniou, Epure et al. 2013) yet not well established at 7T. Increasing magnetic field strength allowed for an

increase in signal to noise ratio (SNR) improving overall image quality. To date 7T MRI spine research has been limited to pilot studies developing whole spine techniques (Wu, Wang et al. 2010, Cohen-Adad, Zhao et al. 2012, Dzyubachyk, Lelieveldt et al. 2013, Zhao, Cohen-Adad et al. 2013). Ideally, future development of a single imaging sequence would enable clear distinction between the discs substructure, however separate sequences were required to visualize the CEP and annulus fibrosus. Clear substructure visualization would permit tracking CEP and NP deformations under load.

The CEP morphology was visualized in three dimensions and thickness quantified using an MRI $200\ \mu\text{m}^3$ isotropic 3D FLASH (fast low-angle shot) sequence (Moon, Yoder et al. 2013) in Chapter 3. The circumferential size and shape of the CEP was highly irregular and varied amongst subjects and disc levels. No correlation was found between CEP thickness and disc level; however the periphery was significantly thicker compared to central locations over the nucleus pulposus. The relatively short scan time of 3 minutes per disc has shown potential in-vivo applications (Moon, Yoder et al. 2013). A semi-automated thickness measurement technique is currently in development providing less user input. This technique will permit an in-vivo population study looking at the effects of CEP size and shape with degeneration. Such studies will augment our understanding on substructure interactions, disc mechanics, and overall disc health as the CEP acts as a mechanical barrier between the pressurized NP and as a gateway for nutrient transport (Crock and Goldwasser 1984, Roberts, Menage et al. 1993, Moore 2000, Urban and Roberts 2003).

Annulus fibrosus lamellae were visualized in three dimensions with an optimized MRI 3D T2-weighted TSE (turbo spin-echo) sequence in Chapter 4. The high-resolution

300 μm^3 isotropic imaging sequence permitted distinction between adjacent lamellae. This clear distinction enabled annular tear detection, characterization, and detailed geometric quantification. Annular tears visualized in this work demonstrated their “non-classic” classification through interconnecting radial, circumferential, and perinuclear formations. Future work will further validate this technique with MRI slice matched histological and gross sectioning of the disc.

The custom-built loading device from Chapter 5 permitted long relaxation times outside of the MR scanner and maintained compression and hydration throughout imaging. Several improvements will be made in the future to mitigate current limitations and enhance mechanical testing capabilities. The incorporation of a watertight tank will remove the need for agarose during image acquisition in conjunction with reduced imaging times will enable in-MRI loading. The loss of signal to noise ratio with integration of the loading frame and RF coil (Wright, Lemdiasov et al. 2011) may have been a result of insufficient signal loading to the transmit coil. Improved coil loading might improve SNR, which in-turn could permit increased image resolution and/or decreased image acquisition time. Mechanical testing capabilities will be increased by the addition of design for torsion and new loading platens to apply combined loading schemes such as torsion + compression and bending + compression.

The long image acquisition time of 2.75 hours, loss of 2.33X signal to noise ratio on clinical scanners (3T), and the current strength of spine surface coils limits this approach to cadaveric work. The study of strain around such defects will require improved image resolution as the lamellar thickness ranges between 140 – 520 μm (Marchand and Ahmed 1990). Improved image resolution and lamellar contrast will

enable future work to study strain patterns around annular tears. In-combination with out of MRI cyclic loading there is potential to analyze how pre-existing tears propagate throughout the disc.

This method did provide adequate lamellar detection for tracking internal deformations of the disc with image registration in-order to measure internal strain. Internal intervertebral disc strain measurements with Advanced Normalization Tools image registration in Chapter 6 had excellent correspondence to previously published 2D work (O'Connell, Malhotra et al. , O'Connell, Johannessen et al. 2007). In combination with high-resolution 3D images from Chapter 4 and the MRI safe loading device from Chapter 5, out-of-plane AF lamellar tracking with image registration enhanced the validity and accuracy for non-invasive strain measurements in Chapter 7 and 8. The ability to identify lamellar boundaries with 3D Sobel edge detection facilitated image registration parameter optimization yielding excellent registration correspondence. The ability to perform tissue and experimental specific verification of image registration is a distinct advantage compared to utilizing MR phantoms (Chan and Neu 2013) or computer generated deformations (Reiter, Fathallah et al. 2012).

Qualitative observations of strain patterns in Chapter 7 were similar to those observed in 2D by O'Connell *et al.* (O'Connell, Johannessen et al. 2007). Three-dimensional strain map quantitative regional AF strain analysis in Chapter 7 and Chapter 8 further emphasized the discs inhomogeneous nature and effect of native boundary conditions. Based on the work of Costi *et al.* (Costi, Stokes et al. 2007) the inner lateral AF regional segmentations were proportionally smaller than corresponding outer regions (Figure 37C). Projecting the circumferential (anterior, anterior-lateral, lateral, posterior-

lateral, and posterior) boundaries diagonally out from the nucleus and/or normalizing data by volume would alleviate this issue.

Disc geometry and architectural composition appear to play a significant role in differences in strain magnitude between disc regions under axial compression. Annulus fibrosus fiber insertion to the vertebral body and endplate yielded large tensile axial strains while compressive strains were more than double the applied strain magnitude at the mid disc height where fibers were more free to move. Disc-height variability strongly dictated regional differences in axial strain, for instance the large anterior disc height led to smaller strain magnitudes in this disc region. The discs kidney bean shape created non-uniform circumferential strain patterns with high strain in the lateral region being a product of the larger radial distance from the discs center. The weaker posterior annulus consists of fewer lamellae lessening its ability to counterattack the outward forces of the nucleus pulposus and experience greater radial strain magnitudes. Overall, the inner AF experienced more strain than the outer AF, which might be a result of the weaker inner AF being constrained between the stiff outer AF and pressurized NP. The creation of a template disc from each specimen within this study would account for geometric differences such as height, volume, and cross-sectional shape. Spatial mapping between each specimen and the template would enable the mapping of strain patterns to study both how an average population and degenerative grade responds to axial compression and how an individual differs from the norm.

Future work will focus on the internal degenerative effects on regional strain properties within the disc. Discs will be block segmented by degenerative grade (Pfirrmann, Metzdorf et al. 2001) and T2 value (Blumenkrantz, Zuo et al. , Marinelli,

Haughton et al. , Antoniou, Epure et al. 2013) so that no overlap occurs. Degenerative blocks will be defined as follows (degenerative grade and T2 value): Mild = (grade < 2 and T2 > 120ms), Moderate = (2 < grade < 4 and 100 ms < T2 < 80 ms), and Severe = (grade > 4 and T2 < 60ms). Each specimen will undergo the same experimental protocol and strain analysis methods described in Chapter 8. Based on limited availability of lumbar spines, a total study size of n=18 have been collected with Grade 2 (n=6), Grade 3(n=9), Grade 4 (n=2) and Grade 5 (n=1) to date.

The developed internal strain measurement technique will enable future studies to analyze loading modalities beyond axial compression. The addition of an angled loading platen will enable compression + flexion/extension or compression + bending similar to previous work by O'Connell *et al.* (O'Connell, Vresilovic et al.). Torsional mechanics can be evaluated through the addition of strategically placed locking pins to the loading frame. To permit torsional strain, a locking pin is required at the loading frame – Instron interface bracket and applied in a counterclockwise direction so that the threaded driving and supporting rod (Figure 17) do not loosen. Two locking pins will traverse through the locking bolts and loading frame in order to secure applied torsional strain (Figure 17). Based on these preliminary design concepts both compression + extension/flexion/bending and torsion strains will be limited to a single degree of deformation.

High-resolution three-dimensional image acquisition and registration in combination with the ability to perform out of MRI loading will facilitate testing the mechanical effects of various treatments to the disc. Future work could assess the effects on internal disc strain with and without posterior elements. Additionally, the mechanical

affects for clinically relevant treatments such as nucleotomy (removal of nucleus pulposus) and nucleus pulposus replacements can be determined. Testing of restorative treatments will aid implant design by establishing their ability to restore disc mechanics to a healthy state.

Based on data from Chapter 7-8 healthy strain patterns will be defined for analysis on the effect of disc pressurization as an attempt to restore the IVD to a healthy state. A balloon catheter will be used to incrementally pressurize degenerate intervertebral discs and strain measured within each disc sub-region. Measured values will be compared to the individual disc's intact strain measurements, to median strain values at varying levels of degeneration, and changes in disc height. A reference image will be acquired under a nominal pre-load of 0.5 BW (0.24MPa), which is the stress seen on the disc when laying in the supine position (Wilke, Neef et al. 1999).



Figure 43: Proof of concept balloon loading placement: (A) Unpressurized placement in center of NP under fluoroscopic guidance, (B) Pressurized balloon, and (C) Securing of balloon.

Deformed images will include the disc after insertion of a balloon catheter laterally into the disc under fluoroscopic guidance placing the midline of the balloon in the center of the NP unfilled (Figure 43) and after pressurization to 25 – 50 – 75 psi, based on pressures seen during discography (Nachemson and Morris 1964). The disc will be

allowed to relax for 30 minutes between incremental pressurizations and subsequently imaged.

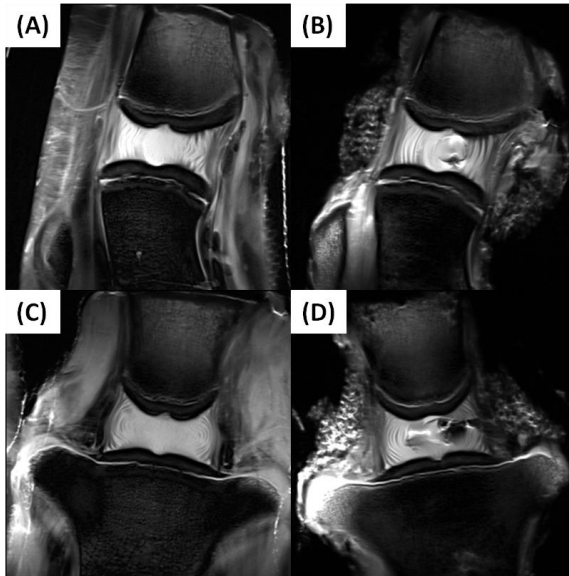


Figure 44: Proof of concept balloon visualization comparing an intact bovine motion segment to balloon pressurization: (A – B) Intact sagittal and coronal view and (C – D) Pressurized sagittal and coronal view.

Preliminary experiments showed a visible change in disc height; change in disc height will be measured at each pressurization level (Figure 44).

In conclusion, the work presented here provides key technical advances to measure 3D internal strains in intact human lumbar discs. Regional strain inhomogeneity was observed qualitatively and quantitatively. Variation in strain magnitudes might be explained by geometry in axial and circumferential strain while peak radial strain in the posterior AF may have important implications for disc herniation. Overall new methods were developed to further study the development and evaluation of surgical procedures, design of implants to restore mechanics, and effects of degeneration on the intervertebral disc.

Bibliography

- Abumi, K., M. M. Panjabi, K. M. Kramer, J. Duranceau, T. Oxland and J. J. Crisco (1990). "Biomechanical evaluation of lumbar spinal stability after graded facetectomies." Spine (Phila Pa 1976) **15**(11): 1142-1147.
- Acaroglu, E. R., J. C. Iatridis, L. A. Setton, R. J. Foster, V. C. Mow and M. Weidenbaum (1995). "Degeneration and aging affect the tensile behavior of human lumbar annulus fibrosus." Spine (Phila Pa 1976) **20**(24): 2690-2701.
- Accadbled, F., J. M. Laffosse, D. Ambard, A. Gomez-Bouchet, J. S. de Gauzy and P. Swider (2008). "Influence of location, fluid flow direction, and tissue maturity on the macroscopic permeability of vertebral end plates." Spine (Phila Pa 1976) **33**(6): 612-619.
- Adams, M. A. (2004). "Biomechanics of back pain." Acupunct Med **22**(4): 178-188.
- Adams, M. A. and P. Dolan (2005). "Spine biomechanics." J Biomech **38**(10): 1972-1983.
- Adams, M. A., P. Dolan and W. C. Hutton (1986). "The stages of disc degeneration as revealed by discograms." J Bone Joint Surg Br **68**(1): 36-41.
- Adams, M. A. and W. C. Hutton (1981). "The relevance of torsion to the mechanical derangement of the lumbar spine." Spine (Phila Pa 1976) **6**(3): 241-248.
- Adams, M. A. and W. C. Hutton (1983). "The effect of fatigue on the lumbar intervertebral disc." J Bone Joint Surg Br **65**(2): 199-203.
- Adams, M. A., D. W. McMillan, T. P. Green and P. Dolan (1996). "Sustained loading generates stress concentrations in lumbar intervertebral discs." Spine (Phila Pa 1976) **21**(4): 434-438.
- Adams, M. A., D. S. McNally and P. Dolan (1996). "Stress' distributions inside intervertebral discs. The effects of age and degeneration." J Bone Joint Surg Br **78**(6): 965-972.
- Adams, M. A. and P. J. Roughley (2006). "What is intervertebral disc degeneration, and what causes it?" Spine (Phila Pa 1976) **31**(18): 2151-2161.
- Alyas, F., D. Connell and A. Saifuddin (2008). "Upright positional MRI of the lumbar spine." Clin Radiol **63**(9): 1035-1048.
- Andersson, G. B. (1999). "Epidemiological features of chronic low-back pain." Lancet **354**(9178): 581-585.
- Antoniou, J., L. M. Epure, A. J. Michalek, M. P. Grant, J. C. Iatridis and F. Mwale (2013). "Analysis of quantitative magnetic resonance imaging and biomechanical parameters on human discs with different grades of degeneration." J Magn Reson Imaging **38**(6): 1402-1414.
- Antoniou, J., F. Mwale, C. N. Demers, G. Beaudoin, T. Goswami, M. Aebi and M. Alini (2006). "Quantitative magnetic resonance imaging of enzymatically induced degradation of the nucleus pulposus of intervertebral discs." Spine (Phila Pa 1976) **31**(14): 1547-1554.
- Argoubi, M. and A. Shirazi-Adl (1996). "Poroelectric creep response analysis of a lumbar motion segment in compression." J Biomech **29**(10): 1331-1339.
- Ariga, K., S. Miyamoto, T. Nakase, S. Okuda, W. Meng, K. Yonenobu and H. Yoshikawa (2001). "The relationship between apoptosis of endplate chondrocytes and aging and degeneration of the intervertebral disc." Spine (Phila Pa 1976) **26**(22): 2414-2420.
- Avants, B. and J. C. Gee (2004). "Geodesic estimation for large deformation anatomical shape averaging and interpolation." Neuroimage **23 Suppl 1**: S139-150.
- Avants, B. B., C. L. Epstein, M. Grossman and J. C. Gee (2008). "Symmetric diffeomorphic image registration with cross-correlation: evaluating automated labeling of elderly and neurodegenerative brain." Med Image Anal **12**(1): 26-41.
- Avants, B. B., N. J. Tustison, G. Song, P. A. Cook, A. Klein and J. C. Gee (2011). "A reproducible evaluation of ANTs similarity metric performance in brain image registration." Neuroimage **54**(3): 2033-2044.
- Avants, B. B., P. Yushkevich, J. Pluta, D. Minkoff, M. Korczykowski, J. Detre and J. C. Gee "The optimal template effect in hippocampus studies of diseased populations." Neuroimage **49**(3): 2457-2466.
- Bae, W. C., S. Statum, Z. Zhang, T. Yamaguchi, T. Wolfson, A. C. Gamst, J. Du, G. M. Bydder, K. Masuda and C. B. Chung (2013). "Morphology of the cartilaginous endplates in human intervertebral disks with ultrashort echo time MR imaging." Radiology **266**(2): 564-574.
- Bay, B. K. (2001). "Experimental measurement of three-dimensional continuum-level strain fields in trabecular bone." Adv Exp Med Biol **496**: 181-197.

Bay, B. K., T. S. Smith, D. P. Fyhrie and M. Saad (1999). "Digital volume correlation: Three-dimensional strain mapping using X-ray tomography." Experimental Mechanics **39**(3): 217-226.

Beckstein, J. C., A. A. Espinoza Orias, J. M. Cloyd and D. M. Elliott (2007). Axial and torsion mechanics for several animals compared to human disc. 53rd Annual Meeting of the Orthopaedic Research Society, San Diego, CA.

Beckstein, J. C., S. Sen, T. P. Schaer, E. J. Vresilovic and D. M. Elliott (2008). "Comparison of animal discs used in disc research to human lumbar disc: axial compression mechanics and glycosaminoglycan content." Spine (Phila Pa 1976) **33**(6): E166-173.

Benneker, L. M., P. F. Heini, M. Alini, S. E. Anderson and K. Ito (2005). "2004 Young Investigator Award Winner: vertebral endplate marrow contact channel occlusions and intervertebral disc degeneration." Spine (Phila Pa 1976) **30**(2): 167-173.

Bernard, T. N., Jr. (1990). "Lumbar discography followed by computed tomography. Refining the diagnosis of low-back pain." Spine (Phila Pa 1976) **15**(7): 690-707.

Bernick, S. and R. Cailliet (1982). "Vertebral end-plate changes with aging of human vertebrae." Spine (Phila Pa 1976) **7**(2): 97-102.

Best, B. A., F. Guilak, L. A. Setton, W. Zhu, F. Saed-Nejad, A. Ratcliffe, M. Weidenbaum and V. C. Mow (1994). "Compressive mechanical properties of the human annulus fibrosus and their relationship to biochemical composition." Spine (Phila Pa 1976) **19**(2): 212-221.

Bibby, S. R., D. A. Jones, R. B. Lee, J. Yu and J. P. G. Urban (2001). "The pathophysiology of the intervertebral disc." Joint Bone Spine **68**(6): 537-542.

Blumenkrantz, G., X. Li, E. T. Han, D. C. Newitt, J. C. Crane, T. M. Link and S. Majumdar (2006). "A feasibility study of in vivo T1rho imaging of the intervertebral disc." Magn Reson Imaging **24**(8): 1001-1007.

Blumenkrantz, G., J. Zuo, X. Li, J. Kornak, T. M. Link and S. Majumdar "In vivo 3.0-tesla magnetic resonance T1rho and T2 relaxation mapping in subjects with intervertebral disc degeneration and clinical symptoms." Magn Reson Med **63**(5): 1193-1200.

Bogduk, N. (1991). "The lumbar disc and low back pain." Neurosurg Clin N Am **2**(4): 791-806.

Borthakur, A., P. M. Maurer, M. Fenty, C. Wang, R. Berger, J. Yoder, R. A. Balderston and D. M. Elliott "T1rho MRI and Discography Pressure as Novel Biomarkers for Disc Degeneration and Low Back Pain." Spine (Phila Pa 1976).

Brinckmann, P. (1986). "Injury of the annulus fibrosus and disc protrusions. An in vitro investigation on human lumbar discs." Spine (Phila Pa 1976) **11**(2): 149-153.

Brinckmann, P. and H. Grootenboer (1991). "Change of disc height, radial disc bulge, and intradiscal pressure from discectomy. An in vitro investigation on human lumbar discs." Spine (Phila Pa 1976) **16**(6): 641-646.

Broc, G. G., N. R. Crawford, V. K. Sonntag and C. A. Dickman (1997). "Biomechanical effects of transthoracic microdiscectomy." Spine (Phila Pa 1976) **22**(6): 605-612.

Bruehlmann, S. B., J. R. Matyas and N. A. Duncan (2004). "ISSLS prize winner: Collagen fibril sliding governs cell mechanics in the annulus fibrosus: an in situ confocal microscopy study of bovine discs." Spine (Phila Pa 1976) **29**(23): 2612-2620.

Buckwalter, J., V. C. Mow, S. D. Boden, D. R. Eyre and M. Weidenbaum (2000). Intervertebral disc structure, composition and mechanical function. Orthopaedic Basic Science: Biology and Biomechanics of the Musculoskeletal System. J. Buckwalter, T. A. Einhorn and S. R. Simon. Rosemont, IL, American Academy of Orthopaedic Surgeons. **II**: 557-556.

Buckwalter, J. A. (1995). "Aging and degeneration of the human intervertebral disc." Spine (Phila Pa 1976) **20**(11): 1307-1314.

Buckwalter, J. A. and V. C. Mow (2000). Intervertebral disc structure, composition, and mechanical function. Orthopaedic Basic Science. T. A. Einhorn, J. A. Buckwalter and S. R. Simon. Rosemont, IL, American Academy of Orthopaedic Surgeons. **2nd Edition**: 547-556.

Cannella, M., A. Arthur, S. Allen, M. Keane, A. Joshi, E. Vresilovic and M. Marcolongo (2008). "The role of the nucleus pulposus in neutral zone human lumbar intervertebral disc mechanics." J Biomech **41**(10): 2104-2111.

Chan, D. D. and C. P. Neu (2013). "Intervertebral disc internal deformation measured by displacements under applied loading with MRI at 3T." Magn Reson Med.

Chandrashekara, R., R. Mohiaddin, R. Razavi and D. Rueckert (2007). "Nonrigid image registration with subdivision lattices: application to cardiac MR image analysis." Med Image Comput Comput Assist Interv **10**(Pt 1): 335-342.

Cheng, X. G., P. H. Nicholson, S. Boonen, G. Lowet, P. Brys, J. Aerssens, G. Van der Perre and J. Dequeker (1997). "Prediction of vertebral strength in vitro by spinal bone densitometry and calcaneal ultrasound." J Bone Miner Res **12**(10): 1721-1728.

Chiu, E. J., D. C. Newitt, M. R. Segal, S. S. Hu, J. C. Lotz and S. Majumdar (2001). "Magnetic resonance imaging measurement of relaxation and water diffusion in the human lumbar intervertebral disc under compression in vitro." Spine (Phila Pa 1976) **26**(19): E437-444.

Cohen-Adad, J., W. Zhao, L. L. Wald and A. L. Oaklander (2012). "7T MRI of spinal cord injury." Neurology **79**(22): 2217.

Cortes, D. H. and D. M. Elliott (2012). "Extra-fibrillar matrix mechanics of annulus fibrosus in tension and compression." Biomech Model Mechanobiol **11**(6): 781-790.

Cortes, D. H., W. M. Han, L. J. Smith and D. M. Elliott (2013). "Mechanical properties of the extra-fibrillar matrix of human annulus fibrosus are location and age dependent." J Orthop Res **31**(11): 1725-1732.

Costi, J. J., B. J. Freeman and D. M. Elliott "Intervertebral disc properties: challenges for biodevices." Expert Rev Med Devices **8**(3): 357-376.

Costi, J. J., I. A. Stokes, M. Gardner-Morse, J. P. Laible, H. M. Scoffone and J. C. Iatridis (2007). "Direct measurement of intervertebral disc maximum shear strain in six degrees of freedom: motions that place disc tissue at risk of injury." J Biomech **40**(11): 2457-2466.

Crock, H. V. and M. Goldwasser (1984). "Anatomic studies of the circulation in the region of the vertebral end-plate in adult Greyhound dogs." Spine (Phila Pa 1976) **9**(7): 702-706.

Danielson, B. and J. Willen (2001). "Axially loaded magnetic resonance image of the lumbar spine in asymptomatic individuals." Spine (Phila Pa 1976) **26**(23): 2601-2606.

Dathe, H. and G. Helms (2010). "Exact algebraization of the signal equation of spoiled gradient echo MRI." Phys Med Biol **55**(15): 4231-4245.

Deyo, R. A. and Y. J. Tsui-Wu (1987). "Descriptive epidemiology of low-back pain and its related medical care in the United States." Spine (Phila Pa 1976) **12**(3): 264-268.

Drake, J. D., C. D. Aultman, S. M. McGill and J. P. Callaghan (2005). "The influence of static axial torque in combined loading on intervertebral joint failure mechanics using a porcine model." Clin Biomech (Bristol, Avon) **20**(10): 1038-1045.

Dzyubachyk, O., B. P. Lelieveldt, J. Blaas, M. Reijnierse, A. Webb and R. J. van der Geest (2013). "Automated algorithm for reconstruction of the complete spine from multistation 7T MR data." Magn Reson Med **69**(6): 1777-1786.

Ebara, S., J. C. Iatridis, L. A. Setton, R. J. Foster, V. C. Mow and M. Weidenbaum (1996). "Tensile properties of nondegenerate human lumbar anulus fibrosus." Spine (Phila Pa 1976) **21**(4): 452-461.

Ebbesen, E. N., J. S. Thomsen, H. Beck-Nielsen, H. J. Nepper-Rasmussen and L. Mosekilde (1999). "Lumbar vertebral body compressive strength evaluated by dual-energy X-ray absorptiometry, quantitative computed tomography, and ashing." Bone **25**(6): 713-724.

Edwards, W. T., N. R. Ordway, Y. Zheng, G. McCullen, Z. Han and H. A. Yuan (2001). "Peak stresses observed in the posterior lateral anulus." Spine (Phila Pa 1976) **26**(16): 1753-1759.

Elliott, D. M. and J. J. Sarver (2004). "Young investigator award winner: validation of the mouse and rat disc as mechanical models of the human lumbar disc." Spine (Phila Pa 1976) **29**(7): 713-722.

Elliott, D. M. and L. A. Setton (2000). "A linear material model for fiber-induced anisotropy of the anulus fibrosus." J Biomech Eng **122**(2): 173-179.

Elliott, D. M. and L. A. Setton (2001). "Anisotropic and inhomogeneous tensile behavior of the human anulus fibrosus: experimental measurement and material model predictions." J Biomech Eng **123**(3): 256-263.

Eyre, D. R. and H. Muir (1976). "Types I and II collagens in intervertebral disc. Interchanging radial distributions in annulus fibrosus." Biochem J **157**(1): 267-270.

Eyre, D. R. and H. Muir (1977). "Quantitative analysis of types I and II collagens in human intervertebral discs at various ages." Biochim Biophys Acta **492**(1): 29-42.

Fagan, M. J., S. Julian, D. J. Siddall and A. M. Mohsen (2002). "Patient-specific spine models. Part 1: Finite element analysis of the lumbar intervertebral disc--a material sensitivity study." Proc Inst Mech Eng H **216**(5): 299-314.

Farfan, H. F. (1969). "Effects of torsion on the intervertebral joints." Can J Surg **12**(3): 336-341.

Farfan, H. F., J. W. Cossette, G. H. Robertson, R. V. Wells and H. Kraus (1970). "The effects of torsion on the lumbar intervertebral joints: the role of torsion in the production of disc degeneration." J Bone Joint Surg Am **52**(3): 468-497.

Francois, R. J., E. G. Bywaters and M. Aufdermaur (1985). "Illustrated glossary for spinal anatomy. With explanations and a French and German translation." Rheumatol Int **5**(6): 241-245.

Frei, H., T. R. Oxland, G. C. Rathonyi and L. P. Nolte (2001). "The effect of nucleotomy on lumbar spine mechanics in compression and shear loading." Spine (Phila Pa 1976) **26**(19): 2080-2089.

Frymoyer, J. W. (1988). "Back pain and sciatica." N Engl J Med **318**(5): 291-300.

Fujita, Y., N. A. Duncan and J. C. Lotz (1997). "Radial tensile properties of the lumbar annulus fibrosus are site and degeneration dependent." J Orthop Res **15**(6): 814-819.

Fujita, Y., D. R. Wagner, A. A. Biviji, N. A. Duncan and J. C. Lotz (2000). "Anisotropic shear behavior of the annulus fibrosus: effect of harvest site and tissue prestrain." Med Eng Phys **22**(5): 349-357.

Galante, J. O. (1967). "Tensile properties of the human lumbar annulus fibrosus." Acta Orthop Scand: Suppl 100:101-191.

Gallucci, M., M. Anselmi, A. Di Sibio and L. M. Gregori (2011). "Annular tears, fissures or HIZ?" Neuroradiology **53 Suppl 1**: S161-165.

Gilchrist, C. L., J. Q. Xia, L. A. Setton and E. W. Hsu (2004). "High-resolution determination of soft tissue deformations using MRI and first-order texture correlation." IEEE Trans Med Imaging **23**(5): 546-553.

Goel, V. K., B. T. Monroe, L. G. Gilbertson and P. Brinckmann (1995). "Interlaminar shear stresses and laminae separation in a disc. Finite element analysis of the L3-L4 motion segment subjected to axial compressive loads." Spine (Phila Pa 1976) **20**(6): 689-698.

Grignon, B., Y. Grignon, D. Mainard, M. Braun, P. Netter and J. Roland (2000). "The structure of the cartilaginous end-plates in elder people." Surg Radiol Anat **22**(1): 13-19.

Hamanishi, C., T. Kawabata, T. Yosii and S. Tanaka (1994). "Schmorl's nodes on magnetic resonance imaging. Their incidence and clinical relevance." Spine (Phila Pa 1976) **19**(4): 450-453.

Hangai, M., K. Kaneoka, S. Hinotsu, K. Shimizu, Y. Okubo, S. Miyakawa, N. Mukai, M. Sakane and N. Ochiai (2009). "Lumbar intervertebral disk degeneration in athletes." Am J Sports Med **37**(1): 149-155.

Hanley, E. N., Jr. and D. E. Shapiro (1989). "The development of low-back pain after excision of a lumbar disc." J Bone Joint Surg Am **71**(5): 719-721.

Hansson, T. and B. Roos (1983). "The amount of bone mineral and Schmorl's nodes in lumbar vertebrae." Spine (Phila Pa 1976) **8**(3): 266-271.

Hansson, T., B. Roos and A. Nachemson (1980). "The bone mineral content and ultimate compressive strength of lumbar vertebrae." Spine (Phila Pa 1976) **5**(1): 46-55.

Hansson, T. H., T. S. Keller and D. M. Spengler (1987). "Mechanical behavior of the human lumbar spine. II. Fatigue strength during dynamic compressive loading." J Orthop Res **5**(4): 479-487.

Hardisty, M. R., M. Akens, A. J. Yee and C. M. Whyne "Image registration demonstrates the growth plate has a variable affect on vertebral strain." Ann Biomed Eng **38**(9): 2948-2955.

Haughton, V. (2004). "Medical imaging of intervertebral disc degeneration: current status of imaging." Spine (Phila Pa 1976) **29**(23): 2751-2756.

Helms, G., H. Dathe and P. Dechent (2008). "Quantitative FLASH MRI at 3T using a rational approximation of the Ernst equation." Magn Reson Med **59**(3): 667-672.

Heuer, F., H. Schmidt and H. J. Wilke (2008). "The relation between intervertebral disc bulging and annular fiber associated strains for simple and complex loading." J Biomech **41**(5): 1086-1094.

Heuer, F., H. Schmidt and H. J. Wilke (2008). "Stepwise reduction of functional spinal structures increase disc bulge and surface strains." J Biomech **41**(9): 1953-1960.

Hickey, D. S. and D. W. Hukins (1980). "Relation between the structure of the annulus fibrosus and the function and failure of the intervertebral disc." Spine (Phila Pa 1976) **5**(2): 106-116.

Hilton, R. C., J. Ball and R. T. Benn (1976). "Vertebral end-plate lesions (Schmorl's nodes) in the dorsolumbar spine." Ann Rheum Dis **35**(2): 127-132.

Ho, M. M., T. A. Kelly, X. E. Guo, G. A. Ateshian and C. T. Hung (2006). "Spatially varying material properties of the rat caudal intervertebral disc." Spine (Phila Pa 1976) **31**(15): E486-493.

Holmes, A. D. and D. W. Hukins (1996). "Analysis of load-relaxation in compressed segments of lumbar spine." Med Eng Phys **18**(2): 99-104.

Holmes, A. D., D. W. Hukins and A. J. Freemont (1993). "End-plate displacement during compression of lumbar vertebra-disc-vertebra segments and the mechanism of failure." Spine (Phila Pa 1976) **18**(1): 128-135.

Hoppe, S., S. Quirbach, T. C. Mamisch, F. G. Krause, S. Werlen and L. M. Benneker (2012). "Axial T2 mapping in intervertebral discs: a new technique for assessment of intervertebral disc degeneration." Eur Radiol **22**(9): 2013-2019.

Iatridis, J. C., S. Kumar, R. J. Foster, M. Weidenbaum and V. C. Mow (1999). "Shear mechanical properties of human lumbar annulus fibrosus." J Orthop Res **17**(5): 732-737.

Iatridis, J. C., L. A. Setton, M. Weidenbaum and V. C. Mow (1997). "The viscoelastic behavior of the non-degenerate human lumbar nucleus pulposus in shear." J Biomech **30**(10): 1005-1013.

Iatridis, J. C., M. Weidenbaum, L. A. Setton and V. C. Mow (1996). "Is the nucleus pulposus a solid or a fluid? Mechanical behaviors of the nucleus pulposus of the human intervertebral disc." Spine (Phila Pa 1976) **21**(10): 1174-1184.

Jacobs, N. T., L. J. Smith, W. M. Han, J. Morelli, J. H. Yoder and D. M. Elliott (2011). "Effect of orientation and targeted extracellular matrix degradation on the shear mechanical properties of the annulus fibrosus." J Mech Behav Biomed Mater **4**(8): 1611-1619.

Johannessen, W., J. D. Auerbach, A. J. Wheaton, A. Kurji, A. Borthakur, R. Reddy and D. M. Elliott (2006). "Assessment of human disc degeneration and proteoglycan content using T1rho-weighted magnetic resonance imaging." Spine (Phila Pa 1976) **31**(11): 1253-1257.

Johannessen, W., J. M. Cloyd, G. D. O'Connell, E. J. Vresilovic and D. M. Elliott (2006). "Trans-endplate nucleotomy increases deformation and creep response in axial loading." Ann Biomed Eng **34**(4): 687-696.

Johannessen, W., E. J. Vresilovic, A. C. Wright and D. M. Elliott (2004). "Intervertebral disc mechanics are restored following cyclic loading and unloaded recovery." Ann Biomed Eng **32**(1): 70-76.

Kakitsubata, Y., D. J. Theodorou, S. J. Theodorou, D. Trudell, P. L. Clopton, A. S. Donich, N. Lektrakul and D. Resnick (2003). "Magnetic resonance discography in cadavers: tears of the annulus fibrosus." Clin Orthop Relat Res **407**: 228-240.

Kambin, P., L. F. Cohen, M. Brooks and J. L. Schaffer (1995). "Development of degenerative spondylosis of the lumbar spine after partial discectomy. Comparison of laminotomy, discectomy, and posterolateral discectomy." Spine (Phila Pa 1976) **20**(5): 599-607.

Katz, J. N. (2006). "Lumbar disc disorders and low-back pain: socioeconomic factors and consequences." J Bone Joint Surg Am **88 Suppl 2**: 21-24.

Kawchuk, G. N., A. M. Kaigle Holm, L. Ekstrom, T. Hansson and S. H. Holm (2009). "Bulging of the inner and outer annulus during in vivo axial loading of normal and degenerated discs." J Spinal Disord Tech **22**(3): 214-218.

Keller, T. S., D. M. Spengler and T. H. Hansson (1987). "Mechanical behavior of the human lumbar spine. I. Creep analysis during static compressive loading." J Orthop Res **5**(4): 467-478.

Klein, A., J. Andersson, B. A. Ardekani, J. Ashburner, B. Avants, M. C. Chiang, G. E. Christensen, D. L. Collins, J. Gee, P. Hellier, J. H. Song, M. Jenkinson, C. Lepage, D. Rueckert, P. Thompson, T. Vercauteren, R. P. Woods, J. J. Mann and R. V. Parsey (2009). "Evaluation of 14 nonlinear deformation algorithms applied to human brain MRI registration." Neuroimage **46**(3): 786-802.

Koeller, W., F. Funke and F. Hartmann (1984). "Biomechanical behavior of human intervertebral discs subjected to long lasting axial loading." Biorheology **21**(5): 675-686.

Korecki, C. L., J. J. MacLean and J. C. Iatridis (2008). "Dynamic compression effects on intervertebral disc mechanics and biology." Spine (Phila Pa 1976) **33**(13): 1403-1409.

Krismer, M., C. Haid and W. Rabl (1996). "The contribution of anulus fibers to torque resistance." Spine (Phila Pa 1976) **21**(22): 2551-2557.

Kumar, S. (2004). "Vibration in operating heavy haul trucks in overburden mining." Appl Ergon **35**(6): 509-520.

Kuroki, H., V. K. Goel, S. A. Holekamp, N. A. Ebraheim, S. Kubo and N. Tajima (2004). "Contributions of flexion-extension cyclic loads to the lumbar spinal segment stability following different discectomy procedures." Spine (Phila Pa 1976) **29**(3): E39-46.

Kusaka, Y., S. Nakajima, O. Uemura, H. Aoshiba, Y. Seo and Y. Hirasawa (2001). "Intradiscal solid phase displacement as a determinant of the centripetal fluid shift in the loaded intervertebral disc." Spine (Phila Pa 1976) **26**(9): E174-181.

Lawrence, J. P., H. S. Greene and J. N. Grauer (2006). "Back pain in athletes." J Am Acad Orthop Surg **14**(13): 726-735.

Lehmann, T. M., C. Gonner and K. Spitzer (1999). "Survey: interpolation methods in medical image processing." IEEE Trans Med Imaging **18**(11): 1049-1075.

Liang, Y., H. Zhu and M. H. Friedman "Measurement of the 3D arterial wall strain tensor using intravascular B-mode ultrasound images: a feasibility study." *Phys Med Biol* **55**(21): 6377-6394.

Liu, L. and E. F. Morgan (2007). "Accuracy and precision of digital volume correlation in quantifying displacements and strains in trabecular bone." *J Biomech* **40**(15): 3516-3520.

Liu, Y. K., G. Njus, J. Buckwalter and K. Wakano (1983). "Fatigue response of lumbar intervertebral joints under axial cyclic loading." *Spine (Phila Pa 1976)* **8**(8): 857-865.

Lotz, J. C., V. Haughton, S. D. Boden, H. S. An, J. D. Kang, K. Masuda, A. Freemont, S. Berven, D. K. Sengupta, L. Tanenbaum, P. Maurer, A. Ranganathan, A. Alavi and N. L. Marinelli (2012). "New treatments and imaging strategies in degenerative disease of the intervertebral disks." *Radiology* **264**(1): 6-19.

Luo, X., R. Pietrobon, S. X. Sun, G. G. Liu and L. Hey (2004). "Estimates and patterns of direct health care expenditures among individuals with back pain in the United States." *Spine (Phila Pa 1976)* **29**(1): 79-86.

Lyons, G., S. M. Eisenstein and M. B. Sweet (1981). "Biochemical changes in intervertebral disc degeneration." *Biochim Biophys Acta* **673**(4): 443-453.

Maintz, J. B. A. and M. A. Viergever (1998). "A survey of medical image registration." *Medical Image Analysis* **2**(1): 1-36.

Malko, J. A., W. C. Hutton and W. A. Fajman (1999). "An in vivo magnetic resonance imaging study of changes in the volume (and fluid content) of the lumbar intervertebral discs during a simulated diurnal load cycle." *Spine (Phila Pa 1976)* **24**(10): 1015-1022.

Marchand, F. and A. M. Ahmed (1990). "Investigation of the laminate structure of lumbar disc annulus fibrosus." *Spine (Phila Pa 1976)* **15**(5): 402-410.

Mariconda, M., O. Galasso, P. Attingenti, G. Federico and C. Milano (2010). "Frequency and clinical meaning of long-term degenerative changes after lumbar discectomy visualized on imaging tests." *Eur Spine J* **19**(1): 136-143.

Marinelli, N. L., V. M. Haughton and P. A. Anderson "T2 relaxation times correlated with stage of lumbar intervertebral disk degeneration and patient age." *AJNR Am J Neuroradiol* **31**(7): 1278-1282.

Marinelli, N. L., V. M. Haughton, A. Munoz and P. A. Anderson (2009). "T2 relaxation times of intervertebral disc tissue correlated with water content and proteoglycan content." *Spine (Phila Pa 1976)* **34**(5): 520-524.

Martin, M. D., C. M. Boxell and D. G. Malone (2002). "Pathophysiology of lumbar disc degeneration: a review of the literature." *Neurosurg Focus* **13**(2): E1.

McBroom, R. J., W. C. Hayes, W. T. Edwards, R. P. Goldberg and A. A. White, 3rd (1985). "Prediction of vertebral body compressive fracture using quantitative computed tomography." *J Bone Joint Surg Am* **67**(8): 1206-1214.

McGirt, M. J., S. Eustacchio, P. Varga, M. Vilendecic, M. Trummer, M. Gorensek, D. Ledic and E. J. Carragee (2009). "A prospective cohort study of close interval computed tomography and magnetic resonance imaging after primary lumbar discectomy: factors associated with recurrent disc herniation and disc height loss." *Spine (Phila Pa 1976)* **34**(19): 2044-2051.

McNally, D. S. and M. A. Adams (1992). "Internal intervertebral disc mechanics as revealed by stress profilometry." *Spine (Phila Pa 1976)* **17**(1): 66-73.

Meakin, J. R. and D. W. Hukins (2000). "Effect of removing the nucleus pulposus on the deformation of the annulus fibrosus during compression of the intervertebral disc." *J Biomech* **33**(5): 575-580.

Meakin, J. R., T. W. Redpath and D. W. Hukins (2001). "The effect of partial removal of the nucleus pulposus from the intervertebral disc on the response of the human annulus fibrosus to compression." *Clin Biomech (Bristol, Avon)* **16**(2): 121-128.

Moon, S. M., J. H. Yoder, A. C. Wright, L. J. Smith, E. J. Vresilovic and D. M. Elliott (2013). "Evaluation of intervertebral disc cartilaginous endplate structure using magnetic resonance imaging." *Eur Spine J* **22**(8): 1820-1828.

Moore, R. J. (2000). "The vertebral end-plate: what do we know?" *Eur Spine J* **9**(2): 92-96.

Murphy, K., B. van Ginneken, J. M. Reinhardt, S. Kabus, K. Ding, X. Deng, K. Cao, K. Du, G. E. Christensen, V. Garcia, T. Vercauteren, N. Ayache, O. Commowick, G. Malandain, B. Glocker, N. Paragios, N. Navab, V. Gorbunova, J. Sporring, M. de Bruijne, X. Han, M. P. Heinrich, J. A. Schnabel, M. Jenkinson, C. Lorenz, M. Modat, J. R. McClelland, S. Ourselin, S. E. Muenzing, M. A. Viergever, D. De Nigris, D. L. Collins, T. Arbel, M. Peroni, R. Li, G. C. Sharp, A. Schmidt-Richberg, J. Ehrhardt, R. Werner, D. Smeets, D. Loeckx, G. Song, N. Tustison, B. Avants, J. C. Gee, M. Staring, S. Klein, B. C. Stoel, M. Urschler, M. Werlberger, J. Vandemeulebroucke, S. Rit, D. Sarrut and J. P. Pluim (2011).

"Evaluation of registration methods on thoracic CT: the EMPIRE10 challenge." IEEE Trans Med Imaging **30**(11): 1901-1920.

Nachemson, A., T. Lewin, A. Maroudas and M. A. Freeman (1970). "In vitro diffusion of dye through the end-plates and the annulus fibrosus of human lumbar inter-vertebral discs." Acta Orthop Scand **41**(6): 589-607.

Nachemson, A. and J. Morris (1963). "Lumbar discometry. Lumbar intradiscal pressure measurements in vivo." Lancet **1**(7291): 1140-1142.

Nachemson, A. and J. M. Morris (1964). "In Vivo Measurements of Intradiscal Pressure. Discometry, a Method for the Determination of Pressure in the Lower Lumbar Discs." J Bone Joint Surg Am **46**: 1077-1092.

Nachemson, A. L., A. B. Schultz and M. H. Berkson (1979). "Mechanical properties of human lumbar spine motion segments. Influence of age, sex, disc level, and degeneration." Spine (Phila Pa 1976) **4**(1): 1-8.

Ng, L. and L. Ibanez (2004). Medical image registration: concepts and implementation. Insight into images: Principles and Practice for Segmentation, Registration, and Image Analysis. T. S. Yoo. Wellesey, MA, A K Peters
CRC Press: 239-306.

Nguyen, A. M., W. Johannessen, J. H. Yoder, A. J. Wheaton, E. J. Vresilovic, A. Borthakur and D. M. Elliott (2008). "Noninvasive quantification of human nucleus pulposus pressure with use of T1rho-weighted magnetic resonance imaging." J Bone Joint Surg Am **90**(4): 796-802.

O'Connell, G. D., H. L. Guerin and D. M. Elliott (2009). "Theoretical and uniaxial experimental evaluation of human annulus fibrosus degeneration." J Biomech Eng **131**(11): 111007.

O'Connell, G. D., N. T. Jacobs, S. Sen, E. J. Vresilovic and D. M. Elliott (2011). "Axial creep loading and unloaded recovery of the human intervertebral disc and the effect of degeneration." J Mech Behav Biomed Mater **4**(7): 933-942.

O'Connell, G. D., W. Johannessen, E. J. Vresilovic and D. M. Elliott (2007). "Human internal disc strains in axial compression measured noninvasively using magnetic resonance imaging." Spine (Phila Pa 1976) **32**(25): 2860-2868.

O'Connell, G. D., N. R. Malhotra, E. J. Vresilovic and D. M. Elliott "The Effect of Discectomy and the Dependence on Degeneration of Human Intervertebral Disc Strain in Axial Compression." Spine (Phila Pa 1976).

O'Connell, G. D., E. J. Vresilovic and D. M. Elliott "Human intervertebral disc internal strain in compression: The effect of disc region, loading position, and degeneration." J Orthop Res.

O'Connell, G. D., E. J. Vresilovic and D. M. Elliott (2007). "Comparison of animals used in disc research to human lumbar disc geometry." Spine (Phila Pa 1976) **32**(3): 328-333.

Osti, O. L., B. Vernon-Roberts, R. Moore and R. D. Fraser (1992). "Annular tears and disc degeneration in the lumbar spine. A post-mortem study of 135 discs." J Bone Joint Surg Br **74**(5): 678-682.

Pearce, R. H., B. J. Grimmer and M. E. Adams (1987). "Degeneration and the chemical composition of the human lumbar intervertebral disc." J Orthop Res **5**(2): 198-205.

Pech, P. and V. M. Haughton (1985). "Lumbar intervertebral disk: correlative MR and anatomic study." Radiology **156**(3): 699-701.

Peng, B., S. Hou, W. Wu, C. Zhang and Y. Yang (2006). "The pathogenesis and clinical significance of a high-intensity zone (HIZ) of lumbar intervertebral disc on MR imaging in the patient with discogenic low back pain." Eur Spine J **15**(5): 583-587.

Perie, D., D. Korda and J. C. Iatridis (2005). "Confined compression experiments on bovine nucleus pulposus and annulus fibrosus: sensitivity of the experiment in the determination of compressive modulus and hydraulic permeability." J Biomech **38**(11): 2164-2171.

Perie, D. S., J. J. Maclean, J. P. Owen and J. C. Iatridis (2006). "Correlating material properties with tissue composition in enzymatically digested bovine annulus fibrosus and nucleus pulposus tissue." Ann Biomed Eng **34**(5): 769-777.

Perry, J., V. Haughton, P. A. Anderson, Y. Wu, J. Fine and C. Mistretta (2006). "The value of T2 relaxation times to characterize lumbar intervertebral disks: preliminary results." AJNR Am J Neuroradiol **27**(2): 337-342.

Pfirrmann, C. W., A. Metzdorf, M. Zanetti, J. Hodler and N. Boos (2001). "Magnetic resonance classification of lumbar intervertebral disc degeneration." Spine (Phila Pa 1976) **26**(17): 1873-1878.

Phatak, N. S., S. A. Maas, A. I. Veress, N. A. Pack, E. V. Di Bella and J. A. Weiss (2009). "Strain measurement in the left ventricle during systole with deformable image registration." Med Image Anal **13**(2): 354-361.

Phatak, N. S., Q. Sun, S. E. Kim, D. L. Parker, R. K. Sanders, A. I. Veress, B. J. Ellis and J. A. Weiss (2007). "Noninvasive determination of ligament strain with deformable image registration." Ann Biomed Eng **35**(7): 1175-1187.

Pokharna, H. K. and F. M. Phillips (1998). "Collagen crosslinks in human lumbar intervertebral disc aging." Spine (Phila Pa 1976) **23**(15): 1645-1648.

Race, A., N. D. Broom and P. Robertson (2000). "Effect of loading rate and hydration on the mechanical properties of the disc." Spine (Phila Pa 1976) **25**(6): 662-669.

Raj, P. P. (2008). "Intervertebral disc: anatomy-physiology-pathophysiology-treatment." Pain Pract **8**(1): 18-44.

Reiter, D. A., F. A. Fathallah, R. T. Farouki and J. H. Walton (2012). "Noninvasive high resolution mechanical strain maps of the spine intervertebral disc using nonrigid registration of magnetic resonance images." J Biomech **45**(8): 1534-1539.

Resnick, D. and G. Niwayama (1978). "Intravertebral disk herniations: cartilaginous (Schmorl's) nodes." Radiology **126**(1): 57-65.

Reuber, M., A. Schultz, F. Denis and D. Spencer (1982). "Bulging of lumbar intervertebral disks." J Biomech Eng **104**(3): 187-192.

Riches, P. E., N. Dhillon, J. Lotz, A. W. Woods and D. S. McNally (2002). "The internal mechanics of the intervertebral disc under cyclic loading." J Biomech **35**(9): 1263-1271.

Roberts, S., J. Menage and S. M. Eisenstein (1993). "The cartilage end-plate and intervertebral disc in scoliosis: calcification and other sequelae." J Orthop Res **11**(5): 747-757.

Roberts, S., J. Menage and J. P. Urban (1989). "Biochemical and structural properties of the cartilage end-plate and its relation to the intervertebral disc." Spine (Phila Pa 1976) **14**(2): 166-174.

Roberts, S., J. P. Urban, H. Evans and S. M. Eisenstein (1996). "Transport properties of the human cartilage endplate in relation to its composition and calcification." Spine (Phila Pa 1976) **21**(4): 415-420.

Rodriguez, A. G., C. K. Slichter, F. L. Acosta, A. E. Rodriguez-Soto, A. J. Burghardt, S. Majumdar and J. C. Lotz (2011). "Human disc nucleus properties and vertebral endplate permeability." Spine (Phila Pa 1976) **36**(7): 512-520.

Saifuddin, A., S. Blease and E. MacSweeney (2003). "Axial loaded MRI of the lumbar spine." Clin Radiol **58**(9): 661-671.

Schenck, J. F. (1996). "The role of magnetic susceptibility in magnetic resonance imaging: MRI magnetic compatibility of the first and second kinds." Med Phys **23**(6): 815-850.

Schizas, C., G. Kulik and V. Kosmopoulos "Disc degeneration: current surgical options." Eur Cell Mater **20**: 306-315.

Seroussi, R. E., M. H. Krag, D. L. Muller and M. H. Pope (1989). "Internal deformations of intact and denucleated human lumbar discs subjected to compression, flexion, and extension loads." J Orthop Res **7**(1): 122-131.

Shah, J. S., W. G. Hampson and M. I. Jayson (1978). "The distribution of surface strain in the cadaveric lumbar spine." J Bone Joint Surg Br **60-B**(2): 246-251.

Shea, M., T. Y. Takeuchi, R. H. Wittenberg, A. A. White, 3rd and W. C. Hayes (1994). "A comparison of the effects of automated percutaneous discectomy and conventional discectomy on intradiscal pressure, disk geometry, and stiffness." J Spinal Disord **7**(4): 317-325.

Shirazi-Adl, A. (1994). "Nonlinear stress analysis of the whole lumbar spine in torsion--mechanics of facet articulation." J Biomech **27**(3): 289-299.

Shirazi-Adl, S. A., S. C. Shrivastava and A. M. Ahmed (1984). "Stress analysis of the lumbar disc-body unit in compression. A three-dimensional nonlinear finite element study." Spine (Phila Pa 1976) **9**(2): 120-134.

Skaggs, D. L., M. Weidenbaum, J. C. Iatridis, A. Ratcliffe and V. C. Mow (1994). "Regional variation in tensile properties and biochemical composition of the human lumbar anulus fibrosus." Spine (Phila Pa 1976) **19**(12): 1310-1319.

Smith, L. J., N. L. Nerurkar, K. S. Choi, B. D. Harfe and D. M. Elliott (2011). "Degeneration and regeneration of the intervertebral disc: lessons from development." Dis Model Mech **4**(1): 31-41.

Spera, D., K. Genovese and A. Voloshin (2011). "Application of Stereo-Digital Image Correlation to Full-Field 3-D Deformation Measurement of Intervertebral Disc." Strain **47**: E572-E587.

Stabler, A., M. Bellan, M. Weiss, C. Gartner, J. Brossmann and M. F. Reiser (1997). "MR imaging of enhancing intraosseous disk herniation (Schmorl's nodes)." AJR Am J Roentgenol **168**(4): 933-938.

Stokes, I. A. (1987). "Surface strain on human intervertebral discs." J Orthop Res **5**(3): 348-355.

Stokes, I. A., J. P. Laible, M. G. Gardner-Morse, J. J. Costi and J. C. Iatridis "Refinement of elastic, poroelastic, and osmotic tissue properties of intervertebral disks to analyze behavior in compression." Ann Biomed Eng **39**(1): 122-131.

Takashima, H., T. Takebayashi, M. Yoshimoto, Y. Terashima, H. Tsuda, K. Ida and T. Yamashita "Correlation between T2 relaxation time and intervertebral disk degeneration." Skeletal Radiol.

Thompson, J. P., R. H. Pearce, M. T. Schechter, M. E. Adams, I. K. Tsang and P. B. Bishop (1990). "Preliminary evaluation of a scheme for grading the gross morphology of the human intervertebral disc." Spine (Phila Pa 1976) **15**(5): 411-415.

Tsantrizos, A., K. Ito, M. Aebi and T. Steffen (2005). "Internal strains in healthy and degenerated lumbar intervertebral discs." Spine (Phila Pa 1976) **30**(19): 2129-2137.

Tsuji, H., N. Hirano, H. Ohshima, H. Ishihara, N. Terahata and T. Motoe (1993). "Structural variation of the anterior and posterior annulus fibrosus in the development of human lumbar intervertebral disc. A risk factor for intervertebral disc rupture." Spine (Phila Pa 1976) **18**(2): 204-210.

Tustison, N. J. and A. A. Amini (2006). "Biventricular myocardial strains via nonrigid registration of anatomical NURBS model [corrected]." IEEE Trans Med Imaging **25**(1): 94-112.

Tustison, N. J. and B. Avants (2013). "Explicit B-spline regularization in diffeomorphic image registration." Frontiers in Neuroinformatics **7**.

Tustison, N. J., B. B. Avants and J. C. Gee (2009). "Directly manipulated free-form deformation image registration." IEEE Trans Image Process **18**(3): 624-635.

Tustison, N. J., S. P. Awate, J. Cai, T. A. Altes, G. W. Miller, E. E. de Lange, J. P. Mugler, 3rd and J. C. Gee "Pulmonary kinematics from tagged hyperpolarized helium-3 MRI." J Magn Reson Imaging **31**(5): 1236-1241.

Tustison, N. J., T. S. Cook, G. Song and J. C. Gee "Pulmonary kinematics from image data a review." Acad Radiol **18**(4): 402-417.

Tustison, N. J., V. G. Davila-Roman and A. A. Amini (2003). "Myocardial kinematics from tagged MRI based on a 4-D B-spline model." IEEE Trans Biomed Eng **50**(8): 1038-1040.

Urban, J. P. and J. F. McMullin (1985). "Swelling pressure of the intervertebral disc: influence of proteoglycan and collagen contents." Biorheology **22**(2): 145-157.

Urban, J. P. and J. F. McMullin (1988). "Swelling pressure of the lumbar intervertebral discs: influence of age, spinal level, composition, and degeneration." Spine (Phila Pa 1976) **13**(2): 179-187.

Urban, J. P. and S. Roberts (2003). "Degeneration of the intervertebral disc." Arthritis Res Ther **5**(3): 120-130.

van der Veen, A. J., J. H. van Dieen, A. Nadort, B. Stam and T. H. Smit (2007). "Intervertebral disc recovery after dynamic or static loading in vitro: is there a role for the endplate?" J Biomech **40**(10): 2230-2235.

Veress, A. I., G. T. Gullberg and J. A. Weiss (2005). "Measurement of strain in the left ventricle during diastole with cine-MRI and deformable image registration." J Biomech Eng **127**(7): 1195-1207.

Veress, A. I., J. A. Weiss, G. T. Gullberg, D. G. Vince and R. D. Rabbitt (2002). "Strain measurement in coronary arteries using intravascular ultrasound and deformable images." J Biomech Eng **124**(6): 734-741.

Vernon-Roberts, B., N. L. Fazzalari and B. A. Manthey (1997). "Pathogenesis of tears of the annulus investigated by multiple-level transaxial analysis of the T12-L1 disc." Spine (Phila Pa 1976) **22**(22): 2641-2646.

Vernon-Roberts, B., R. J. Moore and R. D. Fraser (2007). "The natural history of age-related disc degeneration: the pathology and sequelae of tears." Spine (Phila Pa 1976) **32**(25): 2797-2804.

Videman, T. and M. Nurminen (2004). "The occurrence of annular tears and their relation to lifetime back pain history: a cadaveric study using barium sulfate discography." Spine (Phila Pa 1976) **29**(23): 2668-2676.

Villemure, I., L. Cloutier, J. R. Matyas and N. A. Duncan (2007). "Non-uniform strain distribution within rat cartilaginous growth plate under uniaxial compression." J Biomech **40**(1): 149-156.

Vresilovic, E. J., W. Johannessen and D. M. Elliott (2006). "Disc mechanics with trans-endplate partial nucleotomy are not fully restored following cyclic compressive loading and unloaded recovery." J Biomech Eng **128**(6): 823-829.

Wang, J. L., T. K. Wu, T. C. Lin, C. H. Cheng and S. C. Huang (2008). "Rest cannot always recover the dynamic properties of fatigue-loaded intervertebral disc." Spine (Phila Pa 1976) **33**(17): 1863-1869.

Wang, Z. X. and Y. G. Hu (2012). "High-intensity zone (HIZ) of lumbar intervertebral disc on T2-weighted magnetic resonance images: spatial distribution, and correlation of distribution with low back pain (LBP)." Eur Spine J **21**(7): 1311-1315.

Watanabe, A., L. M. Benneker, C. Boesch, T. Watanabe, T. Obata and S. E. Anderson (2007). "Classification of intervertebral disk degeneration with axial T2 mapping." AJR Am J Roentgenol **189**(4): 936-942.

Weidenbaum, M. and J. C. Iatridis (2006). Mechanical behavior of the intervertebral disk and the effects of degeneration. Low Back Pain: A Scientific and Clinical Overview. J. N. Weinstein and S. J. Gordon. Rosemont, IL, American Academy of Orthopaedic Surgeons: 557-582.

Weinstein, J. N., J. D. Lurie, T. D. Tosteson, J. S. Skinner, B. Hanscom, A. N. Tosteson, H. Herkowitz, J. Fischgrund, F. P. Cammisa, T. Albert and R. A. Deyo (2006). "Surgical vs nonoperative treatment for lumbar disk herniation: the Spine Patient Outcomes Research Trial (SPORT) observational cohort." JAMA **296**(20): 2451-2459.

Weiss, J. A., R. D. Rabbitt and A. E. Bowden (1998). Incorporation of medical image data in finite element models to track strain in soft tissues. SPIE, San Jose, CA, Society of Photo-Optical Instrumentation Engineers.

Welsch, G. H., S. Trattinig, T. Paternostro-Sluga, K. Bohndorf, S. Goed, D. Stelzeneder and T. C. Mamisch "Parametric T2 and T2* mapping techniques to visualize intervertebral disc degeneration in patients with low back pain: initial results on the clinical use of 3.0 Tesla MRI." Skeletal Radiol **40**(5): 543-551.

Wilke, H. J., P. Neef, M. Caimi, T. Hoogland and L. E. Claes (1999). "New in vivo measurements of pressures in the intervertebral disc in daily life." Spine (Phila Pa 1976) **24**(8): 755-762.

Wright, A. C., R. Lemdiasov, T. J. Connick, Y. A. Bhagat, J. F. Magland, H. K. Song, S. P. Toddes, R. Ludwig and F. W. Wehrli (2011). "Helmholtz-pair transmit coil with integrated receive array for high-resolution MRI of trabecular bone in the distal tibia at 7T." J Magn Reson **210**(1): 113-122.

Wu, B., C. Wang, R. Krug, D. A. Kelley, D. Xu, Y. Pang, S. Banerjee, D. B. Vigneron, S. J. Nelson, S. Majumdar and X. Zhang (2010). "7T human spine imaging arrays with adjustable inductive decoupling." IEEE Trans Biomed Eng **57**(2): 397-403.

Yang, K. H. and A. I. King (1984). "Mechanism of facet load transmission as a hypothesis for low-back pain." Spine (Phila Pa 1976) **9**(6): 557-565.

Yingling, V. R. and S. M. McGill (1999). "Mechanical properties and failure mechanics of the spine under posterior shear load: observations from a porcine model." J Spinal Disord **12**(6): 501-508.

Yorimitsu, E., K. Chiba, Y. Toyama and K. Hirabayashi (2001). "Long-term outcomes of standard discectomy for lumbar disc herniation: a follow-up study of more than 10 years." Spine (Phila Pa 1976) **26**(6): 652-657.

Yushkevich, P. A., J. Piven, H. C. Hazlett, R. G. Smith, S. Ho, J. C. Gee and G. Gerig (2006). "User-guided 3D active contour segmentation of anatomical structures: significantly improved efficiency and reliability." Neuroimage **31**(3): 1116-1128.

Zhao, W., J. Cohen-Adad, J. R. Polimeni, B. Keil, B. Guerin, K. Setsompop, P. Serano, A. Mareyam, P. Hoecht and L. L. Wald (2013). "Nineteen-channel receive array and four-channel transmit array coil for cervical spinal cord imaging at 7T." Magn Reson Med.

Zuo, J., G. B. Joseph, X. Li, T. M. Link, S. S. Hu, S. H. Berven, J. Kurhanewitz and S. Majumdar "In-vivo Intervertebral Disc Characterization using Magnetic Resonance Spectroscopy and T1rho Imaging: Association with Discography and Oswestry Disability Index and SF-36." Spine (Phila Pa 1976).